

FACTORS CONTRIBUTING TO THE FORMATION
OF SHEETING JOINTS: A STUDY OF SHEETING JOINTS ON A DOME IN
YOSEMITE NATIONAL PARK

A THESIS SUBMITTED TO THE GRADUATE DIVISION OF THE
UNIVERSITY OF HAWAI'I AT MĀNOA IN PARTIAL FULFILLMENT
OF THE REQUIREMENTS FOR THE DEGREE OF

MASTERS OF SCIENCE
IN
GEOLOGY AND GEOPHYSICS

AUGUST 2010

By

Kelly J. Mitchell

Thesis Committee:
Steve Martel, Chairperson
Fred Duennebier
Paul Wessel

Keywords: sheeting joints, exfoliation joints, topographic stresses,
curvature, mechanics, spectral filtering, Yosemite

Acknowledgements

I would like to extend my sincerest gratitude to those who helped make this thesis possible. Thanks to the National Science Foundation for funding this research. Thank you to my graduate advisor, Dr. Steve Martel, for your advice and support through the past few years. This has been a long and difficult project but you have been patient and supportive through it all. Special thanks to my committee, Dr. Fred Duennebier and Dr. Paul Wessel for their advice and contributions; without your help I do not think this project would have been possible. I appreciate the time all of you have spent discussing the project with me. Thank you to Chris Hurren, Shay Chapman, and Carolyn Parcheta for your hard work and moral support in the field; you kept a great attitude during the field season. Special thanks to the National Park Service staff in Yosemite, particularly Dr. Greg Stock and Brian Huggett for their assistance. I wish to thank NCALM, Ole Kaven, Nicholas VanDerElst, and Emily Brodsky for LIDAR data collection. Thank you to Carolina Anchietta Fermin, Lisa Swinnard, and Darwina Griffin for their moral support. Finally, I want to express my deep gratitude to my family for their love and encouragement. Mom, Dad, and Ryan, I love you. Thank you for your patience and emotional support.

Abstract

Sheeting joints (shallow, surface-parallel, opening-mode rock fractures) are widespread and have been studied for centuries. They are commonly attributed to removal of overburden by erosion, but erosion alone cannot open a sheeting joint. I test an alternative hypothesis that sheeting joints open in response to surface-parallel compression along a convex topographic surface using field observations, a large-scale fracture map, and analyses of stresses, slopes, and surface-curvatures (derived from aerial laser altimetry data) for a dome along Tenaya Creek in Yosemite National Park. Approximately 90% of the surface of detailed study is convex in at least one direction. Existing stresses and topography there can account for the nature and distribution of sheeting joints on the doubly-convex surfaces. Sheeting joints parallel and constitute the surface where the surface is doubly convex. Elsewhere, sheeting joints daylight, implying the surface has been eroded since the sheeting joints formed. My findings support the hypothesis.

Table of Contents

Acknowledgements	ii
Abstract.....	iii
List of Tables	vii
List of Figures.....	viii
Chapter 1. Introduction	1
1.1 Motivation	1
1.2 Characteristics of sheeting joints.....	2
1.3 Previous work.....	3
1.4 Hypothesis to be tested.....	7
1.5 Study area	7
1.6 Outline	8
Chapter 2. Mechanical Hypothesis.....	9
Chapter 3. Curvature Tutorial	16
3.1 Curvature of a plane curve	16
3.2 Curvature of surfaces	18
Chapter 4. Geology	22
4.1 Geologic overview of the Tenaya Lake region	22
4.2 Sheeting joints of the Tenaya Lake region.....	23
4.2.1 Characteristics	24
4.2.2 Age	25
4.3 Geologic structures of the TC Dome study area	26
4.3.1 Structural features older than the sheeting joints	27

4.3.2 Sheeting joints	28
4.3.3 Structural features younger than the sheeting joints.....	30
Chapter 5. Aerial LIDAR Data.....	32
5.1 Data collection.....	32
5.2 Calibration and point cloud data	33
5.3 Filtering and gridding by NCALM	34
Chapter 6. Stresses and Topographic Analyses	36
6.1 Stresses	36
6.2 Curvature of an ellipsoidal surface.....	38
6.3 Analyses of unsmoothed topographic data.....	39
6.4 Spectral filtering	39
6.5 Topographic geometry of filtered data	41
6.6 Stress gradient analyses.....	45
Chapter 7. Discussion and Conclusions	48
7.1 Scale of sheeting joints and topography.....	48
7.2 Modern conditions for sheeting joint nucleation at TC Dome study area	49
7.3 Stress gradient and the distribution and nature of sheeting joints at TC Dome	51
7.4 Other lessons	55
7.5 Suggestions for future work	55
7.6 Conclusions	57
Figures.....	60

Appendix A. Orientation of Structural Features at TC Dome	101
Appendix B. Curvature of Individual Sheeting Joints	104
References Cited.....	108

List of Tables

1. Topographic shapes based on principal curvature.....13

2. Topographic shapes based on mean and Gaussian curvature.....20

3. Orientation of Group F fractures.....28

List of Figures

1. Sheeting joints at Shuteye Peak, California60

2. Sheeting joints in cross-section60

3. Tioga Quarry61

4. Map of Yosemite and Tenaya Lake study region61

5. Shaded relief map of Tenaya Lake study region.....62

6. Shaded relief map of TC Dome study area.....63

7. Free body diagram.....64

8. Circular arc diagram.....64

9. Principal curvatures of a saddle-shaped surface65

10. Curvature of a bell-shaped hill65

11. Heavily eroded sheeting joints66

12. Groundwater seeping from sheeting joints.....67

13. Hackle marks.....68

14. Lack of slip across sheeting joint faces69

15. TC Dome as seen from Tenaya Creek.....69

16. TC Dome as seen from East Ridge70

17. East Ridge as seen from TC Dome71

18. Sheeting joints at the base of TC Dome72

19. Buckled sheet on TC Dome73

20. Orientation data for Group F Fractures74

21. Fracture Map of TC Dome study area near the pond.....75

22. Topographic profiles and sheet thickness TC Dome76

23. Point cloud data coverage at TC Dome study area.....	77
24. Gridded aerial LIDAR data at TC Dome study area	78
25. Force balance diagram	79
26. Surface-parallel stress results from conformal mapping solution	79
27. Curvature analysis of an ellipsoidal surface.....	80
28. Unfiltered slope map of TC Dome study area	81
29. Unfiltered k_I curvature map of TC Dome study area	82
30. Unfiltered topography of TC Dome greater area and TC dome study area	83
31. Unfiltered topography of TC Dome study area with best-fit plane removed	84
32. Radial periodogram and lowpass filter.....	85
33. Filtered topography of TC Dome study area	86
34. Filtered slope map of TC Dome study area	87
35. Filtered k_I curvature map of TC Dome greater area	88
36. Filtered k_I curvature map of TC Dome study area	89
37. Filtered k_2 curvature map of TC Dome study area	90
38. Filtered mean curvature map of TC Dome study area	91
39. Filtered Gaussian curvature map of TC Dome study area	92
40. Topographic classification of TC Dome study area.....	93
41. Lower bound for stress gradient at TC Dome study area.....	94
42. Upper bound stress gradient at TC Dome study area	95
43. Sinusoid fit to regional topography	96
44. Histograms of upper and lower bounds for stress gradient.....	97

45. Amount of glacial erosion at TC Dome.....	98
46. Stresses beneath a cusp shaped valley.....	99
47. Fracture F2 modeled as a thrust fault.....	100
A-1. Orientation data at TC Dome study area	102
A-2. Key map for notes at TC Dome study area	103
B-1. Shaded relief map of TC Dome from terrestrial LIDAR	105
B-2. Curvature of individual sheeting joint surfaces	106

Chapter 1. Introduction

Fractures in bedrock are an important factor in natural hazards (such as rock-fall and mass-wasting events), physical weathering, hydrology, and hydrocarbon migration. Understanding the cause of fracture formation increases our ability to prepare for these natural hazards, extract hydrocarbons, and site as well as design waste repositories and dams. This thesis addresses sheeting joints at a dome in Yosemite National Park, California. Sheeting joints are near-surface, curved fractures that develop sub-parallel to topography (Fig. 1). They are commonly referred to as exfoliation joints and occur in many places around the world. Although the study is conducted in Yosemite, the methods used are applicable to many other locations with sheeting joints.

1.1 Motivation

Sheeting joints have been studied for more than two centuries, yet the cause of their formation remains unclear. The most commonly accepted hypothesis for their formation is unloading from removal of overburden by erosion, a possibility proposed by Gilbert (1904). Erosion can certainly cause a decrease in confining pressure perpendicular to the topographic surface. By itself, however, it cannot account for the tension necessary to open these fractures (Martel, 2006). My thesis helps test the hypothesis of Martel (2006) that sheeting joints form in response to surface-parallel compressive stresses acting along a curved topographic surface by inducing a tensile stress normal to the surface at shallow depths. This thesis presents the first known analysis and description of sheeting joints in three dimensions, augments existing documentation on sheeting joint characteristics, and presents methods for analyses that can be applied to other study locations and geologic problems.

1.2 Characteristics of sheeting joints

Sheeting joints divide rock bodies into sheets, much like the layers of an onion. They are typically curved, and their curvature tends to decrease with depth (Fig. 2). In general, sheets tend to be thicker with depth (Dale, 1923; Jahns, 1943; Holzhausen, 1989) (Fig. 3), though in some places thick sheets overly a series of thinner ones (Cadman, 1969).

Sheeting joints have been found at depths more than 100 meters below the ground surface (Dale, 1923; Twidale, 1971). Multiple generations of sheeting joints have been observed in places such as Yosemite National Park in California (Cadman, 1969) and quarries in New England (Holzhausen, 1989). Hackled texture, or plumose structure, observed on sheeting joint faces (Cadman, 1969; Holzhausen, 1977), and the lack of slip across mineral grains and dikes (Jahns, 1943; Cadman, 1969) suggest that sheeting joints originate as opening-mode cracks (e.g., Segall and Pollard, 1983; Pollard and Aydin, 1988; Holzhausen, 1989). Sheeting joints in most locales are thought to be Pleistocene in age (Gilbert, 1904; Bradley, 1963), although some have formed in historic times (Cadman, 1969; Holzhausen, 1977).

Sheeting joints are geographically widespread. Although best known in granitic rocks, they also occur in metamorphic rocks, mafic intrusions, and strong massive sandstone (Bradley, 1963; Twidale, 1982). In many locales such as New England, the Colorado Plateau, and Yosemite National Park, sheeting joints have had a profound effect upon the landscape (Gilbert, 1904; Matthes, 1930; Jahns, 1943; Bradley, 1963; Huber, 1987).

Sheeting joints are most prevalent in massive rock. Their geometry is strongly influenced

by pre-existing structures (Bradley, 1963; Cadman, 1969; Holzhausen, 1989). Sheeting joints are most commonly observed on convex surfaces, such as domes, but they have been observed on some concave surfaces such as U-shaped valleys (Gilbert, 1904).

1.3 Previous work

Some of the most notable work on sheeting joints has been done by Gilbert (1904), Dale (1923), Matthes (1930), Jahns (1943), Bradley (1963), Cadman (1969), and Holzhausen (1977, 1989). These investigators provide careful descriptions of sheeting joints.

Gilbert (1904) studied the sheeting joints of Yosemite National Park. He observed that: 1) sheeting joints are curved; 2) sheeting joints are present on domes, walls of canyons, sides of ridges, and locally on valley walls; and 3) glacial polish is observed on sheets suggesting that sheeting joints pre-date the last glacial episode. Of the three hypotheses Gilbert considered for sheeting joint formation (surficial thermal effects, weathering, and unloading from erosion), his "unloading" hypothesis has persisted and has become the most commonly accepted mechanism (e.g., Chorley, et. al., 1984; Goudie, 2004), although Gilbert himself did not explicitly endorse this as his favored explanation.

Dale (1923) made several key observations of the commercial granites of New England. He noted that sheeting joints are sub-parallel to topography, that sheets have a lenticular shape, and that sheet thickness tends to increase with depth. The most important observation he made with respect to this thesis is that sheeting joints are present in areas currently under high surface-parallel compressive stress. The importance of this

observation will be explained in detail in chapter 2. Among hypotheses Dale tested and rejected are that sheeting joints form from insolation, contraction from cooling of the host intrusive body, tensile stress in the rift direction from cooling, and concentric weathering due to changes in texture or mineral composition. He could not reject surface-normal tension, surface-parallel compressive stress, and some combination of insolation near the surface and surface-parallel compressive stresses at depth as causes. He considered the last of these hypotheses to be the most plausible cause of sheeting joint formation.

Matthes (1930) studied sheeting joints in his seminal research on Yosemite National Park. He observed that sheeting joints become less curved and more widely spaced with depth. The sheets he observed vary in thickness from less than a meter to ~ 30 m.

Matthes recognized that older joints influenced the formation of sheeting joints. He attributed the sheeting joints to stresses in the rock as opposed to weathering. Matthes determined that thermal stresses influence sheeting at shallow depths but would not cause sheeting at depths as great as 30 m. He concluded that Yosemite's famous domes owe their rounded form to sheeting joints. Finally, Matthes estimated that at least half of the landscape in Yosemite owed its form to sheeting joints.

Jahns (1943) also studied the granites of New England. He noted that the curvature of sheeting joints decreases with increased depth; that sheeting joints form independent of mineral grains, dikes, xenoliths, and country rock; and that sheeting joints are best developed in sparsely jointed rock masses. An important observation he, like Dale, made is that New England granites are experiencing high lateral compressive stresses. He

postulated several causes for sheeting joint formation, including cooling; local or regional compressive stress; insolation (daily and secular); hydration and or chemical alteration (which he rejected); mechanical action of fire, frost, and vegetation; a decrease in confining pressure by removal of overburden; or some combination of all previously mentioned causes.

Bradley (1963) worked on sheeting joints of the Colorado Plateau. He observed that sheeting joints are present there in rocks that were once deeply buried, are of Pleistocene age, that pre-existing fractures control the prevalence of sheeting joints, and that sheeting joints are best displayed in thick massive rock units such as sandstones and limestones, being less prevalent in thinly bedded units. He also noted that sheets exposed during the construction of Glen Canyon Dam thickened with depth into the canyon wall. He postulated that sheeting joints form as a result of differential stress from unequal confining pressure release from erosion.

Cadman (1969) studied sheeting joints of Yosemite National Park in California. He observed that some sheeting joint surfaces have plumose structure, a feather-like texture present on opening mode cracks. Cadman made in-situ strain measurements to obtain stress values at Tuolumne Meadows; these are used in this thesis and will be discussed further in later chapters. He postulated that sheeting joints result from surface-parallel compressive stresses.

Holzhausen (1977, 1989) studied sheeting joints of New England. He observed that multiple generations of sheeting joints exist, that younger sheeting joint sheets are influenced by pre-existing structures, and that the hackle and rib marks like those found on sheeting joint faces are also found on rock-burst faces in quarries suggesting that sheeting joints grow rapidly. Holzhausen (1977) tested the hypothesis of Dale, that sheeting joints form in response to high compressive stresses parallel to the ground surface, and he could not reject it. He concluded that sheeting joints form from high differential stress, dominated by high compressive stresses parallel to an exposed rock surface. He also suggested that the cause of this high differential stress could be from vertical unloading by erosion.

A recurring theme is that sheeting joints are most prominent on domes experiencing surface-parallel compressive stresses (Martel, 2006). Holzhausen (1977) and Miller and Dunne (1996) have suggested on theoretical grounds that sheeting joints are related to strong compressive stresses parallel to topography, but they did not test the idea with real topographic data.

Martel (2006) derived a two-dimensional expression of equilibrium to explain the formation of sheeting joints. The key factors are surface-parallel stress, surface curvature, and body forces. He tested his hypothesis using topographic data and stress values from 9 locales across the U. S. and concluded that the sheeting joints present at 7 of the 9 locales can be accounted for by a combination of highly compressive surface-parallel stresses and topographic curvature.

1.4 Hypothesis to be tested

My research further tests Martel's (2006) hypothesis that sheeting joints form in response to surface-parallel stresses acting along a curved topographic surface. This thesis will address two items that were not previously adequately addressed together: 1) a three-dimensional shape of sheeting joints and topography (based on surface curvature), and 2) three-dimensional mechanical analyses for sheeting joint formation. The main focus is on whether sheeting joints at a particular dome in Yosemite National Park, referred to here as Tenaya Creek (TC) Dome, and the surrounding area be accounted for by modern topography and stresses.

1.5 Study area

Yosemite National Park, located in east-central California (Fig. 4), is well known for its vast expanses of granites and spectacular displays of sheeting joints (e.g., Matthes, 1930). It was selected for study because of its high quality sheeting joint exposures. The Tenaya Lake region extends over 77 km² near the center of the park (Figs. 4 and 5). Perhaps the single most striking display of sheeting joints in the Tenaya Lake region occurs at TC Dome along the northwest margin of Tenaya Canyon (Figs. 5 and 6). TC Dome is located at UTM 282491 northing, 4187365 easting, zone 11 (Fig. 6); its summit elevation is 2491 m. TC Dome has a gross doubly-convex shape (this will be discussed further subsequently). It is bordered by a ridge to the north-northeast, Tenaya Canyon to the east-southeast, and immediately to the east by Tenaya Creek (Fig. 6). This thesis

focuses on the TC Dome study area, but also utilizes observations from elsewhere in the Tenaya Lake region.

1.6 Outline

The remainder of this thesis presents field observations coupled with topographic and mechanical analyses to determine whether or not sheeting joints at TC Dome may be accounted for by the modern stress state and current topography. Two key factors in the analyses are surface-parallel stresses and surface curvature. The mechanical hypothesis being tested is explained in detail in chapter 2. Chapter 3 presents a tutorial of surface curvature, a concept from differential geometry that has only recently begun to be used in geology (e.g., Bergbauer, 2002; Pearce et. al, 2006). Chapter 4 presents geologic observations from the Tenaya Lake region and TC Dome, and describes the relative ages of structural features at TC Dome and East Ridge (Fig. 6). Chapter 5 discusses the collection, processing, and quality of aerial LIDAR data for the Tenaya Lake region. In chapter 6, stress and topographic analyses are presented for the TC Dome study area. Finally, chapter 7 discusses the findings and presents the key conclusions.

Chapter 2. Mechanical Hypothesis

Observations of sheeting joint faces overwhelmingly favor an opening-mode formation. Opening-mode, or mode I, fractures can open in one of two ways. Either a far-field stress normal to the fracture must be tensile, or the internal pressure (such as a fluid pressure) acting within the fracture must exceed the far-field compressive stress acting to close it (e.g., Pollard and Segall, 1987). One would anticipate either chemical alteration on sheeting joint faces or mineralization within the joints if they were opened by fluid pressure. Other than iron oxide stains along some sheeting joints, neither chemical alteration nor mineralization was observed along sheeting joints at TC Dome. Therefore, tension is required in order to open these joints.

The commonly accepted hypothesis that sheeting joints form in response to removal of overburden is not mechanically acceptable because removal of overburden, by itself, merely decreases the compressive stress normal to the topographic surface. While this reduction of vertical compressive stress will lead to a positive elastic strain (extension) normal to the surface, this does not equate to a tensile stress necessary to open a sheeting joint. In contrast, tension perpendicular to sheeting joint walls can be induced by high compressive stresses acting parallel to a convex topographic surface (Martel, 2006).

Figure 7 illustrates in two dimensions how a compressive stress (P) acting parallel to an infinitesimal convex surface element along the ground surface can induce a tension normal to the surface (N). Throughout the thesis, tension is considered as positive (hence compression is negative). Curvature is positive if concave (and negative if convex). The

convex upper surface of the element in Fig. 7 is traction free, and no shear tractions (τ) exist on the boundaries of the element. The compressive (negative) tractions on the element ends induce a force directed away from the center of curvature (F_r) that must be opposed by tensile tractions (N) perpendicular to the base of the element in order to maintain equilibrium (Martel, 2006).

Martel (2006) derived an expression using the equations of equilibrium that provide insight into near-surface stress conditions when a body force due to gravity is present. He showed that

$$\left. \frac{\partial N}{\partial z} \right|_{z=0} = kP - F_g, \quad [1]$$

where $\left. \frac{\partial N}{\partial z} \right|_{z=0}$ is the change in stress normal (N) to the surface with respect to depth (z), as evaluated at the surface; k is surface curvature ($1/r$, or the inverse of the radius of curvature); P is the normal stress acting parallel to the topographic surface. The term F_g is the body force due to gravity

$$F_g = \rho g \cos \beta \quad [2]$$

where ρ is density of the rock, g is gravitational acceleration, and β is the slope of the surface. Substituting Equation (2) into Equation (1) yields

$$\left. \frac{\partial N}{\partial z} \right|_{z=0} = kP - \rho g \cos \beta. \quad [3]$$

In order for sheeting joints to form, N must be tensile (positive) near the surface. Since $N=0$ at the surface ($z = 0$), a tension is guaranteed in the shallow subsurface where $\left. \frac{\partial N}{\partial z} \right|_{z=0} > 0$.

Equation (3) pertains strictly to a profile across cylindrical topography, but it may be expanded to a three-dimensional solution for use with topographic surfaces of arbitrary shape (Martel, 2005):

$$\left. \frac{\partial N}{\partial z} \right|_{z=0} = k_1 P_1 + k_2 P_2 - \rho g \cos \beta \quad [4]$$

where k_1 and k_2 are principal curvatures, P_1 and P_2 are normal stresses acting along the directions of the principal curvatures, and β is the slope. Surface curvature will be described in detail in the following chapter. For now, it suffices to say that the shape of a topographic surface at a point can be described by the maximum and minimum curvatures k_1 and k_2 . Equation (4) allows one to predict conditions under which sheeting joints could or should not nucleate based on topographic geometry and surface-parallel stresses.

Threshold conditions for sheeting joint formation are set by the $\rho g \cos \beta$ term of Equation (4). Assuming that sheeting joints open in tension, a necessary condition for sheeting joint nucleation would be that $k_1 P_1 + k_2 P_2 \geq \rho g \cos \beta$. In other words, the stress gradient acting to open the fracture ($k_1 P_1 + k_2 P_2$) exceeds that acting to close the fracture ($\rho g \cos \beta$).

Table 1 illustrates topographic shapes based upon combinations of principal curvatures. Those model landforms shown with an asterisk are most susceptible to developing sheeting joints if surface-parallel stresses P_1 and P_2 are compressive (negative) and of large magnitude, as is the case in the Tenaya Lake region (Cadman, 1969). For a dome, both principal curvatures are negative, so $k_1 P_1 + k_2 P_2$ would be positive, and sheeting joints could develop if that sum exceeds $\rho g \cos \beta$. Sheeting joints could develop in a

cylindrical ridge because even though k_1 equals 0, k_2 is negative, so $k_1P_1+k_2P_2$ could still be positive and exceed $\rho g \cos\beta$. For a bowl, however, both k_1 and k_2 are positive, hence $k_1P_1+k_2P_2$ would be negative. According to the conditions of Equation (4), sheeting joints should not nucleate beneath a bowl. Sheeting joints should not nucleate beneath a cylindrical valley either because k_1 is positive and k_2 is zero, hence $k_1P_1+k_2P_2$ would be negative. For a perfect plane (which is unlikely to exist in nature) both principal curvatures equal zero, so sheeting joints should not nucleate beneath a perfectly planar surface. For a saddle, perhaps the most common topographic shape, k_1 and k_2 have opposite signs. Whether or not sheeting joints develop beneath a saddle depends on the relative and absolute magnitudes of the products k_1P_1 and k_2P_2 . Where k_2P_2 (the “convex contribution”) sufficiently exceeds k_1P_1 (the “concave contribution”), sheeting joints could form. Thus, assuming surface-parallel stresses are compressive, sheeting joints are most likely to nucleate at domes, cylindrical ridges, and some saddles, but not at bowls, cylindrical valleys, and perfect planes.

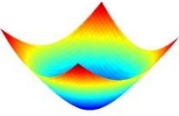
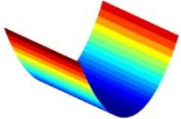
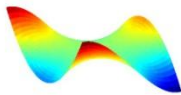
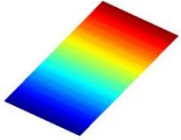
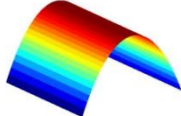
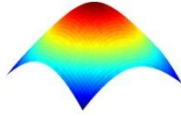
	$k_2 > 0$	$k_2 = 0$	$k_2 < 0$
$k_1 > 0$	Bowl 	Cylindrical Valley 	*Saddle* 
$k_1 = 0$	Doesn't exist: k_1 is always $\geq k_2$ by definition	Plane 	*Cylindrical Ridge* 
$k_1 < 0$	Doesn't exist: k_1 is always $\geq k_2$ by definition	Doesn't exist: k_1 is always $\geq k_2$ by definition	*Dome* 

Table 1. The 6 topographic shapes formed by combinations of principal curvature (modified from Bergbauer, 2002). Red elevations are high, and blue elevations are low. Assuming that surface-parallel stresses P_1 and P_2 are compressive (negative), topography with asterisks is most likely to develop sheeting joints.

The predictions change if surface-parallel stresses are tensile (positive). For a bowl $k_1P_1+k_2P_2$ would be positive, thus sheeting joints might form. Under a cylindrical valley, where k_1 is positive and k_2 is zero, k_1P_1 is positive and k_2P_2 is zero; sheeting joints again could form. At a dome, however, $k_1P_1+k_2P_2$ would be negative, so sheeting joints should not nucleate. Sheeting joints also should not be able to nucleate beneath cylindrical

ridges if surface-parallel stresses are tensile because k_1 is zero and k_2 is negative, so k_1P_1 would be zero and k_2P_2 would be negative. Because perfect planes have principal curvatures of zero, sheeting joints should not nucleate regardless of whether surface-parallel stresses are compressive or tensile. Sheeting joints could still form beneath a saddle if k_1P_1 (the “concave contribution”) sufficiently exceeds the absolute magnitude of k_2P_2 (the “convex contribution”). Thus, assuming surface-parallel stresses are tensile sheeting joints are most likely to nucleate at bowls, cylindrical valleys, and some saddles, but not at domes, cylindrical ridges, and perfect planes. Sheeting joints are less likely to form where surface-parallel stresses are tensile rather than compressive, however. This is because rocks are relatively weak in tension and hence are unlikely to be able to sustain surface-parallel tensile stresses large enough for the sum of the kP products to be large enough to promote the opening of sheeting joints.

In summary, according to Equation (4), sheeting joint nucleation depends upon surface curvature, surface-parallel stresses, the unit weight of the rock (ρg) and the slope. The shape of the topographic surface can act to either permit or preclude the formation of sheeting joints. Sheeting joints should not nucleate beneath a broad perfectly planar surface, regardless of the sign of surface-parallel stresses. Beneath saddles, sheeting joints could nucleate regardless of the sign of surface-parallel stresses. In regions where surface-parallel stresses are tensile everywhere, sheeting joints could nucleate under bowls, cylindrical valleys, and saddles; they are unlikely to nucleate beneath planes, cylindrical ridges, and domes. Where surface-parallel stresses are compressive (such as in the Tenaya Lake region), sheeting joint nucleation is most likely beneath domes,

cylindrical ridges, and saddles, and least likely beneath perfect planes, bowls, and cylindrical valleys. This thesis uses the 3d expression of equilibrium (Eqn. 4) derived by Martel (2006) to test whether or not the current topography and the stresses parallel to the topographic surface at TC Dome can account for the formation of geologically young sheeting joints.

Chapter 3. Curvature Tutorial

This chapter presents a brief tutorial of curvature for plane curves (two-dimensional) and surfaces (three dimensional), both of which were used for topographic analyses throughout this research. Curvature formulas are not derived here but can be found elsewhere (e.g., Struik, 1961; Bergbauer and Pollard, 2003; Mynatt et. al, 2007).

Common usage to the contrary, the curvature of a plane curve is not merely the second derivative, and the curvature of a surface is not merely the Laplacian. The second derivative and Laplacian provide good estimates of curvature only in special cases.

3.1 Curvature of a plane curve

The curvature at a point along a plane curve is defined as the rate of change of a unit tangent, or unit normal, with respect to distance along a curve (e.g., Bergbauer, 2002).

The curvature at a point along a plane curve $y = y(x)$ is (e.g., Leithold, 1976; Roberts, 2001)

$$k = \frac{y''}{[1 + (y')^2]^{3/2}}, \quad [5]$$

where y' and y'' are the first and second derivatives of y with respect to x . The second derivative equals the curvature only where the first derivative equals zero (i.e., at a local maximum or minimum along a plane curve).

Perhaps the simplest plane curve is a circular arc (Fig. 8). Using three points, the radius (r) of a circular arc can be obtained by fitting a circle to the three points, with the center being at the intersection of perpendicular bisectors between line segments connecting pairs of points. The curvature for a circular arc is the inverse of its radius. Another way

to determine the curvature is with the segment height (h) and chord length ($2c$), as shown in Fig. 8:

$$c^2 + (r - h)^2 = r^2 \quad [6]$$

$$c^2 + (r^2 - 2rh + h^2) = r^2 \quad [7]$$

$$c^2 - 2rh + h^2 = 0 \quad [8]$$

$$2rh = c^2 + h^2 \quad [9]$$

$$r = (c^2 + h^2)/2h \quad [10]$$

Assuming that the segment height (h) is very small relative to the half chord length (c):

$$r \approx c^2/2h \quad [11]$$

$$k = 2h/c^2 \quad [12]$$

Minor bumps or noise in real topography and uncertainty in topographic data can greatly affect curvature values. The curvature of such short wavelength features can easily dominate the curvature of longer wavelength topographic features. This can easily be demonstrated by examining the equation of a sinusoid

$$y = A \cos(2\pi x/L), \quad [13]$$

where A is amplitude and L is the wavelength. The first derivative of y with respect to x is

$$y' = -A(2\pi/L) \sin(2\pi x/L). \quad [14]$$

The second derivative of y with respect to x is

$$y'' = -A(2\pi/L)^2 \cos(2\pi x/L). \quad [15]$$

Since the curvature scales with the second derivative, Equation (15) indicates that the curvature increases approximately as the square of the reciprocal of the wavelength. Features with short wavelengths, therefore, can have high associated curvatures even if their amplitudes are small.

3.2 Curvature of surfaces

The concepts of curvature can be extended from plane curves to surfaces. The curvature at a point along a plane curve equals the second derivative if the reference frame is selected such that one of the reference frame axes is normal to the curve (the first derivative term in the denominator of Equation (5) equals zero). A family of cross-section planes that contain the normal to a surface intersect the surface to yield a series of plane curves (Fig. 9). Two of the cross section planes yield plane curves with the maximum and minimum principal curvatures, k_1 and k_2 , respectively. These planes are orthogonal to one another and a plane tangent to the surface (Struik, 1961).

Conceptually, the magnitudes of the principal curvatures could be found by taking the second partial derivatives of the surface $Z = Z(X,Y)$ as expressed in a local reference frame where the two axes X and Y lie in the tangent plane and the third axis (Z) is normal to the tangent plane. These second partial derivatives can be arranged in a 2x2 matrix

$$k = \begin{bmatrix} \frac{\partial^2 Z}{\partial X^2} & \frac{\partial^2 Z}{\partial X \partial Y} \\ \frac{\partial^2 Z}{\partial Y \partial X} & \frac{\partial^2 Z}{\partial Y^2} \end{bmatrix} \quad [16]$$

This real matrix is symmetric (the entry in the upper right matches the entry in the lower left), and hence can be re-expressed in the following form if the X-axis is aligned with the k_1 -direction (Strang, 1998):

$$k = \begin{bmatrix} k_1 & 0 \\ 0 & k_2 \end{bmatrix} \quad [17]$$

Calculation of the magnitudes and directions of the principal curvatures is not trivial in practice, however, and the interested reader should consult references for details (e.g., Struik, 1961; Bergbauer and Pollard, 2003; Pollard and Fletcher, 2005).

Two principal curvatures completely describe the shape of a surface at a point.

Analogous to curvature for plane curves, the principal curvatures for a point on a surface involve combinations of first and second partial derivatives of elevation (z) with respect to easting (x) and northing (y); see Struik (1961) and Bergbauer and Pollard (2003) for details. The principal curvatures are orthogonal, with one direction marking the most positive curvature and the other the most negative curvature (e.g., Struik, 1961).

Although principal curvature directions at a point are orthogonal in a tangent plane, their trends in map view are usually not. In the previous chapter, various combinations of k_1 and k_2 were used to illustrate topographic shapes (Table 1). Two other parameters based on principal curvatures are frequently used to describe topographic shapes as well: mean curvature (H) and Gaussian curvature (K). The mean curvature (H) is the mean value of k_1 and k_2 . Gaussian curvature is the product of k_1 and k_2 . Table 2 illustrates topographic shapes based upon combinations of mean and Gaussian curvature.

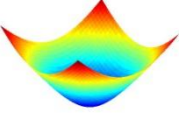
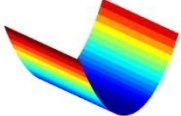
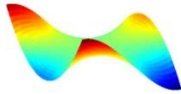
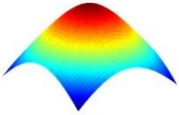
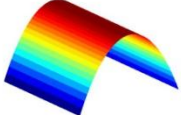
	$G > 0$	$G = 0$	$G < 0$
$H > 0$	Bowl 	Cylindrical Valley 	*Saddle* 
$H = 0$	n/a	Plane 	
$H < 0$	*Dome* 	*Cylindrical Ridge* 	

Table 2. The six topographic shapes formed by combinations of mean (H) and Gaussian (K) curvatures (modified from Roberts, 2001; Mynatt, 2007). Assuming that surface-parallel stresses P_1 and P_2 are compressive (negative), as is the case in the Tenaya Lake region, topography with asterisks are most likely to nucleate sheeting joints.

The shape of a topographic surface varies as a function of both position and wavelength. Two simple examples illustrate this point. First, consider an axisymmetric bell-shaped hill (Fig. 10). Although it has an overall domal shape, a closer look reveals that a true dome only exists near its summit, with a saddle near its base (Fig. 10b). Second, consider a golf ball. At a large wavelength, it appears to be spherical and doubly convex everywhere. However, if fine, short-wavelength features are considered (e.g., the

dimples on the ball), then much of the surface would be seen to be doubly concave (bowl-shaped). Sample spacing and wavelength thus play key roles in the determination of curvature.

Chapter 4. Geology

Yosemite National Park, located in east-central California (Fig. 4), is well known for its vast expanses of granitic rock and spectacular displays of sheeting joints (e.g., Matthes 1930). It was selected for study because of its quality of sheeting joint exposures. Aerial LIDAR (Light Detection and Ranging) data were collected by NCALM (National Center for Airborne Laser Mapping) over 77 km² of the Tenaya Lake region (Fig. 5) of Yosemite stretching approximately from Tuolumne Meadows to Olmsted Point, in the late summer of 2006. The LIDAR data were collected for topographic analyses, and in the hope that sheeting joints could be mapped from these data as well. Details of the LIDAR data collection and its collection are presented in chapter 5.

4.1 Geologic overview of the Tenaya Lake region

Two igneous bodies from the Tuolumne Meadows Intrusive Suite underlie the Tenaya Lake study area: the Cathedral Peak Granodiorite and the Half Dome Granodiorite (e.g., Huber, 1987). The Tuolumne Intrusive Suite was assembled over a period of roughly 10 m.y. between 95 Ma and 85 Ma, based on U-Pb dating (Glazner, et al., 2004). The Half Dome Granodiorite was assembled over a period of nearly 4 m.y. from ~88 Ma to ~91 Ma (Coleman et al., 2004). The Half Dome Granodiorite is medium-grained, light-gray in color, and composed of plagioclase, quartz, orthoclase, biotite, and hornblende (Matthes, 1930). The Cathedral Peak Granodiorite was emplaced ~88 Ma. The Cathedral Peak Granodiorite is easily recognized by its large (~10-20 cm) potassium feldspar phenocrysts; its groundmass is composed of small grains of quartz, feldspar, and

minor amounts of biotite and hornblende (Matthes, 1930). TC Dome is composed of Half Dome Granodiorite.

The uplift of the Sierra Nevada Range is a matter of renewed debate (e.g., Henry, 2009). Some workers suggest that the Sierra Nevada was uplifted during the late Cenozoic ~10 Ma (Unruh, 1991; Wakabayashi and Sawyer, 2001), mainly through a westward tilting of the range. In contrast, others argue that the range was uplifted in the late Mesozoic and remained high in the Cenozoic (Small and Anderson, 1995; Wernicke et al., 1996). They postulate that subsidence of the Basin and Range is responsible for faulting on the eastern flank of the Sierra Nevada, as opposed to uplift of the Sierra. Based on isotopic evidence, Cassel et al. (2009) concluded that the paleo-elevation of the northern Sierra Nevada 31-28 Ma was similar to what is observed today, providing support that most uplift occurred in the Late Cretaceous to early Cenozoic. Much of the current local topography in the High Sierra, which includes Yosemite National Park, is nonetheless likely to be of Quaternary age owing to extensive glaciation (e.g., Bateman and Wahrhaftig, 1966; Gillespie, 1982; Phillips et al., 1996).

4.2 Sheeting joints of the Tenaya Lake region

Sheeting joints are prominently exposed throughout much of the Tenaya Lake region. Some of the most notable locations include Clouds Rest, Cathedral Peak, Tenaya Peak, a dome located immediately southwest of Tenaya Lake (282290 northing, 4188130 easting, with a summit elevation of ~2586 m), Matthes Crest, Olmsted Point, a bowl (281355 northing, 4188295 easting) ~500m north of Olmsted Point, Tioga Road quarry and the

ridge containing it (278943 northing, 4187788 easting) ~3 km west of Olmsted Point, May Lake, and numerous other areas along Tioga Road (Fig. 5).

In many locales where sheeting joints are not immediately apparent they can be observed upon closer examination. Pothole Dome and the dome near BM 8452 (285854 northing, 4193386 easting), both in the northeastern part of the study area, appear to have few sheeting joints. Pothole Dome has extensive glacial polish, potholes, and glacial flutes. Sheeting joints crop out locally, but might have been more widespread and plucked away by Pleistocene glaciers. Near the top of Pothole Dome, sheeting joints decorate the west side of a natural amphitheater (Fig. 11a). Many of these joints do not parallel the modern topography, indicating substantial erosion since the joints formed. At the dome near benchmark 8452, across Tioga Road from Medlicott Dome, the southeastern face appears nearly devoid of sheeting joints, but the northwestern face has heavily weathered sheeting joint steps (Fig. 11b). Most of the southeastern face displays glacial polish and, upon close examination, sheeting joint traces are observed there as well.

4.2.1 Characteristics

Sheeting joints and sheets in the Tenaya Lake region have many common characteristics. Generally, sheets thicken with depth (e.g., Fig. 3), consistent with the findings of Jahns (1943) for New England. This is not the case everywhere, though. Some sheets near the base of TC Dome and at road-cuts along Tioga Road thin with depth. In some places multiple generations of sheeting joints exist. At Mount Hoffman, two sets of sheeting joints are present on an arête; the older set parallels an ancient topographic surface prior

to the last glacial erosion and the younger mimics modern topography (USGS, n.d.). Sheets tend to have a lenticular shape. In many locations, water stains develop down-slope of where sheeting joints daylight, and in several locales water was observed flowing out of sheeting joints (Fig. 12). Sheeting joints and other fractures are a particularly important factor in the shallow hydrology of the Yosemite region because the host crystalline rock has virtually no intrinsic interconnected pore structure.

Sheeting joints of the Tenaya Lake region, like those studied elsewhere by other researchers, exhibit evidence that they originate as opening mode (mode I) fractures (Holman, 1976; Holzhausen, 1989; Bahat et. al, 1999) rather than as shear (mode II or III) fractures. Hackled sheeting joint faces exist in several locales, for example on the southwest face of Pywiak Dome along Tioga Road, and on the northwest face of the ridge containing the Tioga Road quarry (Fig. 13). Where sheeting joints cut dikes, xenoliths, and phenocrysts, no offset is visible (Figs. 11 and 14). All of these observations indicate that sheeting joints in Tenaya Lake region formed as opening-mode fractures. If sheeting joints opened in response to elevated fluid pressures in the rock, then hydro-chemical alteration or mineralization might be expected along the joints. Fresh sheeting joint faces in this region, however, generally are not chemically altered. These observations support the idea that sheeting joints open in tension, not in response to elevated fluid pressure.

4.2.2 Age

Most sheeting joints mimic modern topography, and therefore are unlikely to be older than the Pleistocene. Glacial polish burnishes many sheeting joint faces, demonstrating

that at least some sheeting joints were formed and uncovered prior to the retreat of Tioga-age glaciers approximately 13,000 years ago (Clark, 1995). Other sheeting joints have formed within the last few decades. Cadman (1969) deduced that sheeting joints near Olmsted Point have formed since blasting occurred for the construction of Tioga road, which occurred between 1957 and 1961 (Trexler, 1961). Furthermore, some sheeting joints terminate against boreholes drilled in the quarry during the construction of Tioga road, suggesting that sheeting joints may still be forming.

4.3 Geologic structures of the TC Dome study area

TC Dome, located where the hanging valley of Tenaya Creek drops into Tenaya Canyon (Figs. 5 and 6), displays a spectacular array of sheeting joints (Figs. 14-19). The UTM coordinates of the summit of TC Dome are approximately 282491 northing and 4187365 easting, with a summit elevation of 2491 m. Tenaya Creek flows southeast between TC Dome and a ridge to the northeast (the "East Ridge"). Both TC Dome and the East Ridge display (1) an impressive array of sheeting joints (Fig. 15-18), and (2) large planar fractures that define domains of sheeting joints (Figs. 15, 17, and 18). In addition to these prominent features, dikes, glacial polish, and relatively small fractures (< 2 m long) occur.

The distribution, kinematics, and geometry of sheeting joints at TC Dome study area were documented with photographs (e.g., Figs. 14-19), attitude measurements on individual sheeting joint faces (appendix A), and a fracture map (Fig. 20). The fracture map was made from more than 2,200 points surveyed using a Topcon 206, 0°0'06" total

station instrument. The total station occupied one base station location (282543.6 easting, 4187403.8 northing, and 2451.0 m elev.) and a back-sight was set across Tenaya Canyon (282754.4 easting, 4187266.9 northing, and 2432.6 m elev.). The GPS coordinates were recorded at the base station and back-sight locations using a Geneq (SXBlue) GPS unit with < 2.5 m accuracy. Figures 15-19 show dikes in red and other fractures in blue. Circled numbers mark prominent features: domains of sheeting joints (numbers 1 and 2) and a scarp (number 3); see Fig. 16. The approximate extent of mapping in Fig. 20 is shown in bright green in Figs. 16 and 17.

4.3.1 Structural features older than the sheeting joints

Two aplite dikes (D1 and D2 shown in red on Figs. 16-18, and 20) extend across Tenaya Creek at TC Dome study area. They trend north-northeast, roughly parallel to Tenaya Canyon. D1 strikes N67°W, dipping 21°NE and D2 strikes N63°W, dipping 34°NE. Their lengths exceed 60 meters and they are approximately 0.3 meters thick. Because D1 and D2 extend across both TC Dome and East Ridge and do not cut any fractures, they are likely to be the oldest geologic structures of the study area.

Group F includes fractures F1-F10 (Fig. 20). They are present on either side of Tenaya Creek, but none cross either the streambed or the steeply dipping fracture (F1) along the streambed. Group F fractures are at least several meters long, with apertures of less than 5 cm. Fractures F2 and F4 exceed 40 meters in length. The fractures appear to lack mineral fillings. No lateral slip was observed across fracture faces where they cut dikes,

but the geometry of both the dikes and F fractures are such that slip would not be easily detectable. Orientation data for fractures F1-F10 are shown in Table 3 and Fig. 21.

Group F fractures are younger than dikes D1 and D2 because they cut the dikes. The relative ages of the F-fractures cannot be determined with certainty. Fracture F6 terminates against F4, suggesting that F4 is the older of the two fractures. Sheeting joints terminate against F fractures but do not cross them, suggesting that F-fractures are older than sheeting joints at TC Dome study area.

Fracture	Orientation (strike, dip)		Fracture	Orientation (strike, dip)
F1	~N40°W, ~90°		F6	N45°W, 44°NE
F2	S13°W, 17°NW		F7	S88°E, 14°S
F3	N81°E, 21°S		F8	S67°E, 69°SW
F4	N40°W, 13°NE		F9	S73°E, 60°SW
F5	N48°W, 50°NE		F10	S86°W, 22°N

Table 3. Orientation of Group F fractures (see Fig. 20)

4.3.2 Sheeting joints

Virtually the entire upper two-thirds of the topographic surface of TC Dome consist of sheeting joint faces (Figs. 14-15). Where sheeting joints parallel the topographic surface,

sheeting joint traces are sparse on Fig. 20. The situation differs sharply near the pond at the base of the dome and ridge (Figs. 15-18). Sheeting joints there are expressed as curvilinear traces as opposed to curved surfaces (Fig. 20). Sheeting joints at the base of the dome dip less than 5° , whereas the topography there slopes $\sim 35\text{-}40^\circ$ to the northeast.

Individual sheeting joint surfaces exhibit glacial polish and hackled texture. Some display red water stains, but many do not. Aside from the relatively few sheeting joints that are stained red, sheeting joint surfaces lack obvious chemical alteration. The sparsity of aqueous alteration combined with the presence of hackled texture suggests that the sheeting joints opened in tension rather than in response to high fluid pressures. Some sheeting joint surfaces are glacially polished, indicating that at least some sheeting joints here formed prior to the retreat of Tioga-age glaciers $\sim 13,000$ years ago (Clark, 1995).

Sheeting joints make up the topographic surface of the upper two-thirds of TC Dome and the surface of East Ridge east of fracture F7 (i.e., sheeting joint surfaces and the topographic surface are the same). In general, their shape is doubly-convex, though local concavities are present. Some sheets are longer than 10 meters, and their thickness varies between $\sim 0.3\text{-}0.5$ meters. (Fig. 22). No mineral fillings were observed in the sheeting joints. Lateral slip across in-place sheeting joints was not observed, although many sheets are not in-place, having slid down-slope. Sheeting joint apertures are generally less than 2 cm where sheets are in place. Sheeting joints cut dikes D1 and D2, and terminate against fractures of group F; therefore sheeting joints must be younger than dikes and fractures from group F.

Sheeting joints near the pond, on both TC Dome and East Ridge, are not parallel to the topographic surface. The topographic surface slopes $\sim 40\text{-}50^\circ$ to the northeast at the base of TC Dome, and $\sim 30^\circ$ to the southwest at East Ridge. Sheeting joint traces near the pond trend north-northwest, sub-parallel to Tenaya Creek. On TC Dome, sheeting joints near the pond are divided into two domains based upon their geometry and location relative to fracture F2. Sheeting joints beneath or east of F2, and north of F3 are in domain 1. Domain 1 sheeting joints dip less than 5° and are closely spaced (< 0.2 m) (Fig. 22). Domain 2 sheeting joints, west of F2, are spaced less than 0.5 meters apart, and curve sharply toward fracture F2. The dihedral angle between F2 and the sheeting joints is approximately $45\text{-}60^\circ$. Sheeting joints on East Ridge near the pond dip $10\text{-}20^\circ$ to the southwest and are spaced less than 0.5 meters apart. Their apertures are less than 2 cm. No lateral slip was observed across sheeting joints near the pond. Sheeting joints near the pond cut dikes D1 and D2 and terminate against fractures of group F, so sheeting joints near the pond must be the youngest of these features.

4.3.3 Structural features younger than the sheeting joints

Group O fractures strike north-northeast, dip steeply ($\sim 80\text{-}90^\circ$), and are relatively short, with lengths ranging from 0-3 meters. As with the other planar fracture groups, O-fractures show no mineral fill and are not water stained. Group O fractures terminate against F-fractures, indicating that O fractures are younger than F-fractures and hence younger than the dikes too. Some sheeting joints terminate against fractures from group

O, however, at least one O-fracture terminates against sheeting joints, so the relative ages of O-fractures and sheeting joints are unclear.

At least one sheet on TC Dome is fractured and buckled (B1 on Figs. 18 and 19).

Fracture B1 strikes N45°E along the hinge of the buckle and dips ~ 90. No lateral slip was observed across B1, and aperture is ~ 1 cm. The presence of a buckled sheet suggests that, at least recently, the area has been influenced by high surface-parallel compression (Ericson and Olvmo, 2004).

Chapter 5. Aerial LIDAR Data

Aerial LIDAR data, along with aerial photographs, were collected by NCALM over the Tenaya Lake region. The objective was to use these data for topographic analyses, and mapping of individual sheeting joints. An overview of NCALM's data collection and pre-processing is presented below; additional details can be found in NCALM's processing report.

5.1 Data collection

Aerial LIDAR data were collected by NCALM on September 18 and September 22, 2006. Spatial data were collected with an Optech 1233 ALTM (serial #99B112) mounted in a turbocharged twin engine Cessna 337 (tail number N86539). Color images were acquired using a Redlake MS 4100 digital camera; however, the photographs were overexposed and are not used in this thesis. Flight line spacing was held constant at 200 m. Because the flight line spacing was held constant and the height above terrain varied, overlap percentages between swaths vary. The scan angle was held constant at $\pm 19^\circ$, and scan frequency (mirror oscillation frequency) was fixed at 30 Hz.

For the Tenaya Lake region, flying heights averaged approximately 1,000 m above the ground surface. At this height, the cross-track point spacing is 1.2 m. The along-track point spacing depends on the ground speed of the aircraft which averaged approximately 125 knots. The along-track spacing is approximately 1.1 m at nadir and increases up to 2.2 m at the swath edge. Swath width is 670 m and laser spot size is 0.30 m. Project

flight lines were oriented east-northeast, with cross-lines being flown perpendicular to project flight lines.

GPS reference stations were set up at Olmsted Point and Pothole Dome. All observations were submitted to the NGS on-line processor OPUS with solution files included in Appendix A of NCALM's processing report. Final NAD83 UTM coordinates were obtained from the OPUS solutions. Estimated horizontal errors are less than 8 cm, with vertical errors less than 10 cm.

5.2 Calibration and point cloud data

The relative calibration procedure NCALM uses has cross-lines flown for every flight with a heading perpendicular to the project flight line heading. Small polygons containing both the cross lines and project flight lines are processed using approximate calibration values for heading, roll, pitch, and scanner mirror scale. All lines are processed separately and then filtered to remove vegetation. Individual flight line surfaces are then created. An iterative algorithm then computes the best fit between overlapping flight line surfaces, simultaneously accounting for heading, roll, pitch, and scanner mirror scale. The output is checked for all flights using each flight's cross lines. Each flight is calibrated by comparing the height of the nearest neighbor laser point to the height of a set of check points collected by vehicle-mounted GPS.

The data received from NCALM include a 9 column ASCII file (space delimited), with one file per flight strip. The columns are: GPS time (seconds of week), easting last

return, northing last return, height last return, intensity last return, easting first return, northing first return, height first return, and intensity first return. The 9-column ASCII files have ellipsoid heights that do not match the orthometric heights (elevations) found in 3-column ASCII files or 1-meter DEM gridded files. The 1-meter gridded files were used throughout this research. The point cloud (9-column ASCII data set) data set is shown in Figure 23. Holes in the point cloud data set could be due to "shadowing" where the laser is blocked from hitting the ground surface by trees, shrubs, boulders, and other obstacles.

5.3 Filtering and gridding by NCALM

NCALM's filtering and DEM production consisted of three steps: removal of low points, ground classification, and below surface removal. Low points are points that are clearly below the ground surface. The ground classification routine iteratively builds a triangulated surface model. The below-surface removal routine is run after the ground classification and identifies points which are below the true ground surface, effectively fine tuning the results from the low point removal.

After classification, the ground points were interpolated onto 2 km x 2 km overlapping tiles (60 m overlap) with one-meter grid spacing. These ASCII formatted (XYZ) files were created using Golden Software's SURFER ver. 8.01. The overlap allows consistent transitions from one tile to an adjacent tile. The resultant Surfer grid tile set was exported to ESRI ArcInfo floating point binary format. Then, using an NCALM C++ application, the overlap was trimmed from each tile. The trimmed tiles were exported to ESRI

ArcInfo GRID format and merged into one seamless raster dataset. A similar process was used to generate the unfiltered seamless grids. Filtered, gridded aerial LIDAR data are shown as a contoured, hillshade digital elevation model in Figure 24.

Chapter 6. Stresses and Topographic Analyses

Two key factors for testing the hypothesis are surface-parallel stresses and topographic geometry (surface-curvature and slope). This chapter presents stress data, followed by analyses of topography and stress gradient ($\partial N/\partial z$). Topographic analyses are performed in order to determine the shape of the TC Dome study area topographic surface. The stress gradient analysis illuminates whether the current topographic and stress conditions are sufficient to account for sheeting joints observed there.

6.1 Stresses

Existing measurements show surface-parallel compressive stresses of several MPa or greater in Yosemite National Park. Using the over-coring method, Cadman (1969) obtained principal stress values in Tuolumne Meadows (~11 km east-northeast of TC Dome) of $\sigma_1 = -7.6$ MPa oriented N60°W and $\sigma_2 = -13.9$ MPa oriented N30°E. The most compressive stress (σ_2) in Tuolumne Meadows is roughly aligned with major topographic features nearby (e.g., Tenaya Peak, Tenaya Lake, and Tenaya Canyon). Hickman (personal communication, 3/2008) obtained similar magnitudes, but different orientations, from hydrofracturing in two test holes near Wawona (~30 km south of TC Dome). For test hole 1 (50 m below the ground surface), $\sigma_1 = -6.5$ MPa at ~N49°E, and $\sigma_2 = -13$ MPa at N51°W. For test hole 2 (25 m below the ground surface), $\sigma_1 = -5.5$ MPa at ~N22°E, and $\sigma_2 = -9$ MPa at N68°W. Trends of principal stresses near Wawona also roughly coincide with large local topographic features. Although the methods used by Hickman and Cadman differ, the least compressive stress (σ_1) ranges from ~ -6 to ~ -8

MPa and most compressive (σ_2) stress ranges from -9 to \sim -14 MPa, with principal stress trends roughly corresponding to major nearby topographic features.

Figure 25 illustrates a horizontal force balance in cross section through a hill and valley. If horizontal compressive stresses are applied to the sides of the section, the horizontal compressive stresses at the valley bottom must on average exceed those beneath the hill to maintain a force balance. Tuolumne Meadows is a few hundred meters higher than the top of TC Dome; the normal stresses at TC Dome are likely to be at least as compressive as those at Tuolumne Meadows (-13.9 MPa).

The conformal mapping solution of Savage, et al. (1984) was utilized to evaluate possible stress variations along a profile that trends N60°E from the top of TC Dome to its base (profile D-D' on Fig. 24). This solution may be used to evaluate stresses at depth (Savage and Swolfs, 1986; Martel, 2000) as well as at the topographic surface, but the focus here is on stresses at the surface. The solution of Savage et al. (1984) conformally maps a half-space with a horizontal surface to one with a symmetric topographic surface. The topographic surface is defined by two parameters: a and b , where b is the maximum ridge height or valley depth and $a+b/2$ is the distance from the centerline of a ridge or valley to the inflection point on the topographic surface. Positive values of b yield a ridge, negative values a valley. For a valley, a must exceed the absolute value of b .

Figure 26 shows the model topography, the actual topography, and stress calculations for $a = 65$ m, and $b = -65$ m. The far-field horizontal stress was set to a constant -14 MPa,

and vertical stress varies as a function of depth ($\rho g = -2.7 \times 10^4$ Pa/m). In Fig. 26a, the topography used by the conformal mapping solution is shown as a solid line overlain on a topographic profile trending N60°E derived from aerial LIDAR data (Fig. 24). The values of P (surface-parallel stress) vary between -14 MPa at the shoulder of the valley and -25 MPa at the bottom (Fig. 26b). The compressive stresses at the base of TC dome thus could be about twice those at the top.

6.2 Curvature of an ellipsoidal surface

In order to approximate the curvature range for TC Dome as a whole, an ellipsoidal surface with similar dimensions to TC Dome is evaluated in Fig. 27. At 180 meters along the long axis (trending north-south), 100 meters wide along the short axis, and 40 meters high, the ellipsoid has the following range of principal curvature values:

$k_1 = -5.3 \times 10^{-3} \text{ m}^{-1}$ to $-4.2 \times 10^{-3} \text{ m}^{-1}$, and $k_2 = -1.6 \times 10^{-2} \text{ m}^{-1}$ to $-9.8 \times 10^{-3} \text{ m}^{-1}$. Vertical uncertainty in the aerial LIDAR data could be as much as 10 cm, so normally distributed noise of up to 10 cm is added to the nodes on a 1-m grid used to define the ellipsoidal surface in order to gain insight into how much the vertical uncertainty can affect curvature. Curvatures were calculated using an unpublished numerical code by Martel (personal communication, 6/2007). Curvature of the noisy surface varies between $-1.7 \times 10^{-1} \text{ m}^{-1}$ and $1.8 \times 10^{-1} \text{ m}^{-1}$ for k_1 , and $-2.0 \times 10^{-1} \text{ m}^{-1}$ and $-1.4 \times 10^{-1} \text{ m}^{-1}$ for k_2 . These values are much higher than those for the original surface and indicate that filtering is necessary in order to obtain the overall surface curvature at TC Dome from the aerial LIDAR data.

6.3 Analyses of unsmoothed topographic data

The slopes on TC Dome generally range from 0° - 63° , with locally steeper slopes at the "risers" between sheeting joints (Fig. 28). The 1 m gridded aerial LIDAR data are too coarse to identify each individual sheeting joint on TC Dome, but the trend of groups of sheeting joints can be seen as bands sub-parallel to the topographic contours.

The most positive curvature (k_1) on TC Dome as calculated from unsmoothed aerial LIDAR data using points on a 1 m grid shows a speckled or noisy pattern (Fig. 29).

Values of k_1 range from $-4.3 \times 10^{-1} \text{ m}^{-1}$ to $9.0 \times 10^{-1} \text{ m}^{-1}$. The magnitude, based on results from the ellipsoidal surface, is too large to represent the overall surface of TC Dome.

The least positive curvature (k_2) also shows a noisy pattern, as do the mean and Gaussian curvatures.

6.4 Spectral filtering

Spectral filtering allows one to evaluate a topographic surface at different wavelengths (e.g., Bergbauer, 2002; Perron et. al., 2008) and highlight or subdue various features. For example, to evaluate the overall surface and eliminate noise, short wavelength features can be filtered out. Conversely, to emphasize short wavelength features (e.g., streambeds), longer wavelength features can be filtered out. For spectral filtering, the topographic surface is decomposed into a series of sine and cosine waves using a Fourier transform (e.g., Smith, 1997; Smith, 2007), then evaluated and filtered in the wave number domain. The wave number is $1/\lambda$, where λ is the wavelength, and not $2\pi/\lambda$. The

wave number thus is similar to frequency except that we are dealing with amplitude as a function of space rather than time.

Several steps are required in order to perform spectral filtering. First, a least-squares best-fit plane must be removed from the topographic data to remove the mean. The mean elevation after de-trending should be zero. Fast Fourier transforms can introduce ringing, particularly at the edges of a topographic data set. This can be mitigated by windowing the data set and transforming an area larger than the area of interest.

Spectral analyses and lowpass filtering are performed on aerial LIDAR data for TC Dome study area using a Matlab code modified from Perron et al. (2008). The area analyzed (Fig. 30) is greatly extended to minimize edge effects. The extended area will be referred to as the greater TC Dome area. A best fit plane striking 316° and dipping 14° NE is subtracted from TC Dome and the greater area elevation data to remove the mean trend of the topographic surface. Figures 31a and 31b show the topographic surface of TC Dome and the greater area and TC Dome study area, respectively, after the best fit trend is removed, but before windowing the greater area. Elevations now vary about a mean elevation of zero. A Hanning (raised cosine) window is applied to the topographic data and the data are then transformed to the wave number domain using a fast Fourier transform. Figure 32 is a periodogram showing the mean amplitude as a function of radial wave number (or inverse wavelength). Vertical uncertainty in the aerial LIDAR data is ~ 10 cm; amplitudes less than this could represent noise rather than true variations in the topographic surface. The width of TC Dome from the summit to the

pond is ~50 m; wavelengths less than this are unlikely to represent dome-scale topography. The low-pass filter was selected such that wavelengths less than ~70 m are filtered out. This greatly smoothes the topographic surface such that small-amplitude and short-wavelength noise are removed while the overall topographic shape is maintained. To evaluate topographic shape (i.e., slope and surface-curvature) correctly, the data are transformed back into the spatial domain and the best-fit plane is added back in. If the best-fit plane were not included, slopes could be much too low and curvature values greatly affected.

6.5 Topographic geometry of filtered data

The re-trended filtered topographic data (Fig. 33) show the same major topographic features as the unfiltered data. Smaller wavelength features such as the gully northwest of TC Dome have been filtered out. Topographic contours here are much smoother than they were in Fig. 30. Tenaya Creek streambed has a shorter wavelength in cross-section than what was chosen for the filter and has thus been smoothed considerably.

The filtered slope (β) map (Fig. 34) has a noticeably smoother appearance than the map from the unfiltered data (Fig. 26). Many short wavelength features such as those exceeding 40° in Fig. 28 were removed in the filtering process, so patterns corresponding to features such as the gully and steps in topography caused by sheeting joints or other features in Fig. 28 are no longer visible in Fig. 34. The steepest portions of the unfiltered slope map (Fig. 34) correspond to the steepest portions in the filtered slope map (Fig. 28). The area near the summit of TC Dome has a relatively gentle slope between ~ 0 and 25° ,

while the flank of TC Dome is much steeper, varying between ~ 25 and 28° . The lower portions of TC Dome, pond, and East Ridge have gentler slopes, once again between ~ 0 and 25° .

Maximum principal curvature (k_I) is shown in Figs. 35 and 36. Figure 35 shows k_I of the greater TC Dome area and illustrates the extent of edge effects. These edge effects are visible in a border approximately 50 m wide in Fig. 35. The area of interest, TC Dome study area (outlined in a white box) is far from the influence of edge effects. The curvature of the overall topographic surface is much more apparent here (Fig. 36) than it was on the unfiltered surface (Fig. 29), varying between $-1.63 \times 10^{-2} \text{ m}^{-1}$ and $4.04 \times 10^{-2} \text{ m}^{-1}$. These are within one order of magnitude of those for the ellipsoidal surface grossly representing the dome (Fig. 27). The summit of TC Dome and a portion of East Ridge are identified as convex topographic shapes seen in the southwest and northeast corners of Fig. 36, respectively. Three locations in which k_I values are nearly zero are: TC Dome, East Ridge, and a small area in the southeastern corner (~ 4187340 northing, 282560 easting). The green "rings" around TC Dome and TC ridge represent points where k_I is approximately zero. The green area in the southeastern corner does not correspond to a real topographic feature. The point cloud aerial LIDAR data set has a hole in this location and values were interpolated for the 1 m gridded data set (Fig. 22); the process likely introduced some error. Because filtering removed small wavelength features, the pond and streambed were greatly smoothed and do not have a k_I value of zero as one might anticipate. Tick marks representing the direction of k_I in the tangent plane are reasonable, being aligned sub-parallel or roughly orthogonal to topographic

contours. Interestingly, sheeting joints from Fig. 20 are located in a positive or concave area.

Minimum principal curvature (k_2) is shown in Fig. 37, varying between $-4.0 \times 10^{-2} \text{ m}^{-1}$ and $1.2 \times 10^{-2} \text{ m}^{-1}$. As with the maximum principal curvature, minimum principal curvature values shown here depict large topographic shapes and range within an order of magnitude of the ellipsoidal model. An area of positive curvature in the north-northwestern portion of Fig. 37 is west of where the Tenaya Creek streambed changes orientation from north-south to northwest-southeast and where the gully of Fig. 15 drops down to the streambed. The topographic contours here are concave toward the east whereas contours further south are concave towards the west. Additionally, the long-wavelength topography across the streambed is concave. The green "ring" represents points where k_2 is approximately zero. The green area in the southwest corner is artificial, caused by interpolation of data (Fig. 22). In all other areas of this plot k_2 is negative (convex). This represents 90% of the study area.

Mean curvature of the filtered topography, shown in Fig. 38, varies between $-2.6 \times 10^{-2} \text{ m}^{-1}$ and $2.1 \times 10^{-2} \text{ m}^{-1}$. As expected, the mean curvature of the upper portion of TC Dome and a portion of East Ridge is negative, and it is positive where Tenaya Creek changes course near the north edge of the study area. The belt positive mean curvature extends along Tenaya Creek (Fig. 38). The mean curvature ranges from $-2 \times 10^{-2} \text{ m}^{-1}$ to nearly 0 m^{-1} where sheeting joints make up the topographic surface of TC Dome.

Interestingly, the sheeting joints in Fig. 20 lie in an area of positive (concave) mean curvature.

Gaussian curvature, the product of principal curvatures, can help identify topographic shapes. Positive Gaussian curvature occurs either when a surface is doubly-convex or dome-shaped (both k_1 and k_2 are negative) or doubly-concave or bowl-shaped (both k_1 and k_2 are positive). Negative Gaussian curvature occurs only at saddles (k_1 is positive and k_2 is negative). Gaussian curvature of zero occurs on cylindrical ridges (k_1 is zero and k_2 is negative), cylindrical valleys (k_1 is positive and k_2 is zero), or planes (both k_1 and k_2 are zero). One would expect that the Gaussian curvature plot for TC Dome study area should have at least two large areas of positive Gaussian curvature corresponding to TC Dome and East Ridge, with an area between the two having a value that is either zero or negative.

Gaussian curvature for the filtered data is plotted on Fig. 39 and varies between $-3.8 \times 10^{-4} \text{ m}^{-2}$ and $5.3 \times 10^{-4} \text{ m}^{-2}$. The color scale has changed magnitude from the previous plots of k_1 , k_2 , and mean curvature, but warm colors still represent positive values, cool colors represent negative values, and green represents values near zero. The two large, oval-shaped, positive regions on the western side of the plot correspond to the doubly-convex upper portion of TC Dome (southern oval) and the doubly-concave area in which Tenaya Creek changes trend (northern oval). The portion of East Ridge that has positive k_1 , k_2 , and mean curvature has positive Gaussian curvature values as well. Sheeting joints mapped on Fig. 20 lie in an area of negative Gaussian curvature. The

distribution of sheeting joints compared to topographic shape will be discussed in the next chapter.

The gross topographic forms are apparent using the filtered data (Fig. 40). As mentioned in chapter 2, areas of positive (concave) k_1 and k_2 curvature are classified as bowls, negative (convex) k_1 and k_2 as domes, and positive k_1 and negative k_2 as saddles. No location in the TC Dome study area is planar at the 1-m resolution of Fig. 40. The upper portion of TC Dome and a portion of TC ridge are doubly-convex or dome-shaped. The doubly-concave region on the west side of Tenaya Creek and north-northeast of TC Dome is classified as a bowl. The lower portion of TC Dome, East Ridge, and Tenaya Creek streambed are technically classified as saddle-shaped. The small blue area in the southwest corner of Fig. 40 is classified as a dome, but in Fig. 39 this area is colored green and apparently has negative Gaussian curvature. This discrepancy arises because the boundary between green and yellow colors in Fig. 39 actually occurs at $\sim 7 \times 10^{-7} \text{ m}^{-2}$ instead of zero and the Gaussian curvature for the cells in question is $4 \times 10^{-7} \text{ m}^{-2}$. The sheeting joints mapped in Fig. 20 lie in a saddle, but sheeting joints are present above the area mapped (Figs. 16-19). The relationship between sheeting joints shown here and the topographic geometry will be discussed in detail in the following chapter.

6.6 Stress gradient analyses

According to the hypothesis, sheeting joints can nucleate where the surface-normal stress gradient, $\partial N/\partial z$, is positive at the surface. This gradient, evaluated using Eq. (4), requires that surface parallel stresses be evaluated in the same directions as the respective

principal curvatures. Alternatively, this gradient can be bracketed in a way that does not rely on the principal directions (Martel, personal communication, 5/2010)

$$k_1\sigma_2 + k_2\sigma_1 - \rho g \cos\beta \leq \left. \frac{\partial N}{\partial z} \right|_{z=0} \leq k_1\sigma_1 + k_2\sigma_2 - \rho g \cos\beta \quad [18]$$

where σ_1 and σ_2 are principal stresses. Equation (18) is used to model the stress gradient ($\partial N/\partial z$) at the TC Dome study area using the principal stresses obtained for Tuolumne Meadows by Cadman (1969): $\sigma_1 = -6.5$ MPa and $\sigma_2 = -13.9$ MPa. These stress magnitudes will be considered as constant across the study area. The values for k_1 and k_2 in the stress gradient calculations are shown in Figs. 37 and 38, respectively.

Figure 41 shows the lower bound on the stress gradient, and Fig. 42 the upper bound. Positive values of stress gradient in each figure are shown in warm colors (yellow through red), values near zero in green, and negative values are shown in cool colors (cyan through purple). On both figures the minimum stress gradient is about -0.6 MPa/m, and the maximum stress gradient is about 1 MPa/m. The overall patterns of the stress gradients in Figs. 41 and 42 are similar. The upper two-thirds of TC Dome has a positive stress gradient, as does a portion of East Ridge. Sheeting joints form the topographic surface here. Tenaya Creek lies within a belt with a negative stress gradient, as do the lower portions of TC Dome and East Ridge. The biggest difference occurs near 282540 easting, between 4187330 and 4187360 northing, where stress gradient changes from negative in Fig. 41 to positive in Fig. 42. This location corresponds to a break in slope along Tenaya Canyon.

Most of the mapped sheeting joints in Fig. 20 lie in areas of negative stress gradient. Additional sheeting joints are observed throughout much of TC Dome study area (Figs. 14-18), but outside the area mapped in Fig. 20. According to the hypothesis $\partial N/\partial z$ should be positive in order for sheeting joints to nucleate. Reasons for this discrepancy will be discussed in detail in the following chapter.

The range of the stress gradients in Figs. 41 and 42 is revealing. The range of 1.6 MPa/m is roughly two orders of magnitude greater than the value of ρg . This means that the stress gradient contribution from the products of the curvatures and the surface-parallel stresses dwarf the contribution due to the gravitational body forces. This has two key implications. First, scaling the stresses up or down by a constant factor will result in a nearly commensurate scaling of the stress gradient. Doubling (or halving) the stress magnitudes would effectively double (or halve) the stress gradients while maintaining the shape of the stress gradient field. This means that the results here regarding the shape of the stress gradient field are robust, assuming the surface-parallel stresses are constant over the study area. Second, since the curvature magnitudes and slopes in the study area are not particularly remarkable, the signs of the principal curvatures are decisive factors in dictating the stress gradient, given the large magnitudes of the compressive stresses. This explains why doubly convex surfaces in the study area, and probably throughout the park as a whole, are decorated by sheeting joints.

Chapter 7. Discussion and Conclusions

This thesis tests the hypothesis that the presence or absence of recent sheeting joints can be predicted based on the current topography and the current stress state. To address this, I first discuss the scale of sheeting joints and topography in the Tenaya Lake region. This sets the stage for focusing on the central hypothesis, that the existing topography and stress state can account for sheeting joints formed in the recent past.

7.1 Scale of sheeting joints and topography

Sheeting joints in the Tenaya Lake region typically are visible on domes, ridges and saddles less than 1 km in length. No single sheeting joints were observed extending across an entire dome, ridge or saddle in the region. TC Dome, for example, is approximately 90 m wide and 180 m long, but its sheeting joints are several tens of meters long, approximately 10-20% of TC Dome's length. Longer sheeting joints observed in the region occur on the ridge immediately east of Olmsted Point, and the ridge containing Tioga Road quarry. Some sheeting joint trace lengths at these locales exceed 90 m, but they are still short relative to the scale of the topography. All of these observations are consistent with local topographic control on sheeting joint formation.

If sheeting joints were controlled primarily by regional topography (as opposed to local, dome-scaled topography), one would expect sheeting joints to extend through individual domes and across adjacent topography. Canyon wall exposures in the Tenaya Lake region, however, indicate that sheeting joints do not cross large canyons. For example, even though sheeting joint surfaces make up virtually the entire surface of TC Dome,

they do not extend from TC Dome through Tenaya Canyon, nor do they cross from TC Dome to East Ridge across Tenaya Creek. These observations further suggest that sheeting joints are controlled by local (i.e., individual domes, ridges, saddles, etc.) rather than regional topography.

Quantitative analysis also shows that sheeting joints are not controlled by curvature at a regional scale (i.e., topography with length scales greater than a few km). Consider a profile E-E' trending N45°E through TC Dome and Tuolumne Meadows (Figs. 5 and 43). The topographic relief over a distance of 8 km is ~ 0.3 km. A sinusoid with these attributes exhibits curvatures ranging from $-5 \times 10^{-5} \text{ m}^{-1}$ to $5 \times 10^{-5} \text{ m}^{-1}$. Assuming the most compressive stress at Tuolumne Meadows of -14 MPa (Cadman, 1969) can be applied uniformly to the most highly convex points of the profile, the curvature must be negative and have an absolute value of at least $1.9 \times 10^{-3} \text{ m}^{-1}$ for sheeting joints to nucleate (see Equation (3)). The peak curvatures along the sinusoidal fit are less than one-tenth that value. For sheeting joints to form where the curvature is $-5 \times 10^{-5} \text{ m}^{-1}$ the surface-parallel stress must be -540 MPa, more than twice the unconfined compressive strength of strong granite (e.g., Carmichael, 1989). Sheeting joints at TC Dome study area cannot be accounted for by regional-scale topography.

7.2 Modern conditions for sheeting joint nucleation at TC Dome study area

The aerial LIDAR data and Tuolumne Meadow stress measurements can be used to test whether sheeting joints are controlled by local topography (e.g., ridges) in two

dimensions using Equation (3). Maximum principal curvature values (k_I) at TC Dome for filtered topography vary between $-1.6 \times 10^{-2} \text{ m}^{-1}$ and $4.0 \times 10^{-2} \text{ m}^{-1}$ (Fig. 36). For sheeting joints to nucleate where the curvature is $-1.6 \times 10^{-2} \text{ m}^{-1}$, surface-parallel stress (P_I) values need not be more compressive than -1.7 MPa. The most compressive stresses reported by Cadman (1969) for Tuolumne Meadows are nearly an order of magnitude greater than this; the values reported for Wawona (Hickman, personal communication 3/2008) are several times greater as well. Results from the conformal mapping solution (see section 6.1) show that surface-parallel compressive stresses as great as -25 MPa may be present at the base of TC Dome. All surface-parallel stress estimates at TC Dome far exceed the levels necessary to nucleate sheeting joints there, based on two-dimensional analysis.

The concept that sheeting joint formation is controlled by local topography can be explored in three dimensions using the filtered aerial LIDAR data at the TC Dome study area and the distributions for the stress gradient in Figs. 41 and 42. Figure 44 shows histograms of $\partial N/\partial z$ values at points on a square grid with 1 m spacing. These nodes could be considered to represent $\partial N/\partial z$ for 1 m^2 cells. Columns to the left of the dashed line represent locations where the stress gradient ($\partial N/\partial z$) is negative and sheeting joints are predicted not to nucleate. Columns to the right of the dashed line represent locations where the stress gradient is positive and sheeting joints are predicted to nucleate. In Fig. 44a, which represents the stress gradient in Fig. 41, 36% of TC Dome study area exceeds the threshold for nucleating sheeting joints. In Fig. 44b, which represents the stress gradient in Fig. 42, 64% of TC Dome study area exceeds the threshold for nucleating

sheeting joints. The histograms together suggest that the current topographic and stress conditions in the study area as a whole cluster on the verge of being able to nucleate sheeting joints.

7.3 Stress gradient and the distribution and nature of sheeting joints at TC Dome

Sheeting joints make up virtually the entire surface of TC Dome, the exception being the steep face at its base (domain 1 of Figs. 16 and 18) where sheeting joints are not sub-parallel to the present topographic surface. The analyses account for sheeting joints ($\partial N/\partial z > 0$) above the elevation of the uppermost traces on Fig. 20, but predict sheeting joints should not be able to nucleate below this elevation ($\partial N/\partial z < 0$). These findings suggest that the distribution of sheeting joints is not entirely explained by nucleation sites controlled by the current stress and topographic conditions.

Where sheeting joint nucleation is predicted (e.g., Figs. 41 and 42), most sheeting joints are sub-parallel the surface (Figs. 15-18). In contrast, near the pond, where $\partial N/\partial z < 0$ and joint nucleation is not predicted, the sheeting joints are nearly horizontal (dipping $< 5^\circ$), very closely spaced (10-20 cm) (Fig. 22), and do not lie sub-parallel to the topographic surface of TC Dome ($\sim 35^\circ$ - 40° slope). Their character is very different from the rest of TC Dome, and their geometry cannot be accounted for by the modern topography.

At least three non-exclusive factors may account for these apparent discrepancies without violating the proposed mechanical explanation for the nucleation of sheeting joints. First,

sheeting joints could have nucleated where $\partial N/\partial z$ is positive and propagated into and terminated within regions where $\partial N/\partial z$ is negative. Second, the topography could have been altered since sheeting joints formed. Third, the mechanical effects of fracture interaction could account for the change in the nature of the joints. A treatment of the first possibility is beyond the scope of this thesis, but I do explore the latter two options below.

A small amount of material added to TC Dome in cross-section would be sufficient to create a positive stress gradient. The thickness of material required can be estimated using Equation (8). Figure 45 shows a topographic profile D-D' trending N60E (Fig. 24), the same profile used in surface-parallel stress analyses in chapter 5. The solid line represents the current topography, the dotted line shows a surface where the curvature would be zero, and the dashed line shows a surface with curvature sufficient to achieve a positive stress gradient. Assuming the minimum surface-parallel stress at the top of TC Dome is -14 MPa (σ_1 from Tuolumne Meadows), the curvature (k) required for sheeting joint nucleation is $-1.9 \times 10^{-3} \text{ m}^{-1}$. The chord length, $2c$, of the dotted line is 60 m. The minimum thickness of (presumably eroded) material between the dotted line to the current topography is 3.4 meters. Using Equation (12), an additional 0.9 meters of material would be needed to achieve a curvature of $-1.9 \times 10^{-3} \text{ m}^{-1}$. Thus, removal of 4.3 meters of rock by glacial erosion is sufficient to account for the discrepancy between stress gradient values and sheeting joint surface traces observed on TC Dome near the pond. This amount of erosion could easily be accommodated by Tioga glaciation.

Glacial erosion could explain the discrepancies between stress gradient ($\partial N/\partial z$) values and the distribution of sheeting joint traces near the base of TC Dome. They do not, however, completely account for the nearly horizontal and closely spaced sheeting joints oblique to the topographic surface there (Figs. 16 and 18). One way the closely spaced sheeting joints there could be accounted for is by a stress concentration along the base of a paleo-streambed. Consider a cusp-shaped valley, grossly representing a "paleo" cross-section through TC Dome, Tenaya Creek, and the East Ridge (Fig. 46). The stresses are modeled using the conformal mapping method of Savage et al. (1984), assuming a uniform far-field horizontal stress of -14 MPa, ambient vertical stress that varies as a function of depth at a rate of ρg , where ρ is density (2750 kg/m³ was used), with parameters a and b of 65 m and -65 m respectively. Figure 46 shows the most tensile stress for this hypothetical cusp-shaped valley representing Tenaya Creek prior to glaciation. The most tensile stress is contoured, and the least tensile (most compressive) stress trajectories are shown as a proxy for sheeting joint orientations. Near the valley bottom cusp, the stress trajectories change orientation as stresses become more compressive. They are no longer sub-parallel to topography; instead they flatten and become nearly horizontal. like the sheeting joints do now. The joints thus might have formed in a stream-cut valley that was convex on both sides prior to glaciation. Erosion along Tenaya Creek, both glacial and fluvial, could have exposed sub-horizontal joints formed earlier. Fluvial erosion could have exploited fracture F1. This scenario relies on the joints nucleating in a region where $\partial N/\partial z$ is positive and propagating into a region where $\partial N/\partial z$ is negative. Gilbert (1904) noted that sheeting joints occur in some valleys

in the Sierra, and the analysis here shows how sheeting joints could develop nearly to the valley bottoms.

An entirely different process could also account for the close spacing of sheeting joints in domain 1 and the differences in sheeting joint geometry between domains 1 and 2 across fracture F2 (Fig. 18). Fracture F2 dips obliquely to the surface and under high surface-parallel stresses might have slipped as a thrust fault prior to sheeting joint formation.

Using a linearly elastic boundary element model (Crouch and Starfield, 1983; Martel and Muller, 2000), fracture F2 is modeled as a 100 meter long frictionless thrust fault that breaks the surface and has a maximum of ~0.25 meters slip, with the walls remaining in contact. The far-field horizontal stress is assumed to be -10 MPa (mean normal stress from Tuolumne Meadows), and the vertical stress varies as a function of depth at a rate of ρg (with $\rho = 2750 \text{ kg/m}^3$). Figure 47 shows results of the model: (a) the displacement field; (b) trajectories of most compressive stress; and (c) the most tensile stress. Sheeting joints tend to grow perpendicular to the most tensile stress; therefore trajectories of most compressive stress may be used as a proxy for sheeting joint orientation. Trajectories shown in (b) are very similar to what is observed today at the base of TC Dome, with sheeting joints of domain 1 (left of fracture F2) being nearly horizontal whereas those of domain 2 (right of F2) roll steeply toward the fracture. The close spacing of sheeting joints in domain 1 could be accounted for by the tensile stress concentration near the fault in this scenario. Tensile stresses on the left side of the fault are greater and extend deeper than those on the right. Slip of 0.25 m would be very difficult to detect given the nature

of the outcrops and markers near F2. Similar effects could be achieved with an even shorter fault with less slip.

Geologic evidence suggests that sufficient time for topographic modification has elapsed since sheeting joints near the pond formed. Glacial polish on the surface of some sheeting joints at TC Dome indicates that at least some of them formed, and were uncovered, prior to the retreat of Tioga glaciation, ~ 13,000 years ago (Clark, 1995). Fracture F1 and the closely spaced sheeting joints make the region near the pond particularly susceptible to glacial and fluvial erosion.

7.4 Other lessons

My research illuminated two other important points. First, filtering of the LIDAR data was essential to calculate curvatures relevant to this project. Otherwise the curvatures were dominated by short wavelength effects that would be regarded as “noise”. Second, although sheeting joints have been noted for more than a century (Gilbert, 1904) as being characteristically curved, their curvature was never measured. The sheeting joints at TC Dome have curvatures with absolute values as great as $\sim 4 \times 10^{-3} \text{ m}^{-1}$ over lengths of a few tens of meters.

7.5 Suggestions for future work

The stress analyses for this project are based on the nearest stress measurement (Cadman, 1969), at Tuolumne Meadows ~ 11 km away from TC Dome. This measurement is the only one within Tenaya Lake region. Additional stress measurements could greatly

enhance the project. If additional stress measurements were made available, one might use a mechanical numerical model to help interpolate the stresses in the region.

The approach applied at TC Dome could be extended to other areas. Research-grade aerial LIDAR data have been collected across the whole 77 km² Tenaya Lake region by NCALM. NCALM also has collected aerial LIDAR data across other regions of Yosemite for the National Park Service. Analyses similar to those presented in this thesis could be performed for these regions. Hundreds of photographs have been taken, by the author and others, of the topography and individual sheeting joints in the Tenaya Lake region. A map marking the location where many of these photographs were taken has been made by the author in ArcGIS along with a database that could be useful for future analyses. High-resolution topographic contour and hillshade digital elevation maps at a scale of 1:10,000 have also been made by the author, based on aerial LIDAR data gridded to 1 m resolution, for the entire Tenaya Lake region.

At least six specific locations are suggested for further study in the Tenaya Lake region:

- 1) The ridge containing the quarry near the road to May Lake, 2) Tenaya Canyon, 3) Olmsted Point, 4) the bowl immediately north of Olmsted Point, 5) the ridge immediately east of Olmsted Point, and 6) a dome above the southwest shore of Tenaya Lake (Fig. 5).

Data available for the quarry include: terrestrial LIDAR data collected by NCALM, photographs, slab thickness measurements, and strike and dip measurements collected by the author. Tenaya Canyon is an ideal place to study the effects of curvature on sheeting joint formation because so few sheeting joints exist there. The bowl across Tioga Road

from Olmsted Point features displays numerous sheeting joints. High resolution (~ 5-7 cm) tripod-mounted LIDAR data were collected at the bowl by Ole Kaven (Stanford) and Nicholas VanDerElst (UC Santa Cruz) using equipment loaned by Emily Brodsky (UC Santa Cruz). The ridge east of Olmsted Point displays large sheeting joints with a unique geometry on its NW slope. Further study of this ridge may yield insight into the propagation and bifurcation of individual sheeting joints. Finally, the dome (elev. 2491 m) just east of Tenaya Lake has many sheeting joints. Sheeting joints there could be mapped and characterized easily. The suggested study locations include each of the major topographic features: domes (Olmsted Point), ridges (quarry and ridge east of Olmsted Point), saddles (one at the top of a bowl 0.7 km north of Olmsted Point and one along Tenaya Canyon), bowls (0.7 km north of Olmsted Point), and valleys (Tenaya Canyon).

Although the aerial LIDAR data set was collected specifically to test the hypothesis presented in this thesis, it could be used in many other ways. For example, geomorphologists could use these data to explore glacial extent, ice volume, and fluvial geomorphology. Structural geologists could examine the long bedrock fractures easily seen in the data set as well.

7.6 Conclusions

The hypothesis that sheeting joints open in tension as a result of high, surface-parallel compressive stresses acting parallel to a convex topographic surface is supported by field evidence in Tenaya Lake region. The presence of sheeting joints on domes, ridges, and

saddles less than 1 km long indicate local topographic control of the joints rather than regional topographic control because the local topographic curvature is sufficient for sheeting joints to form, whereas the regional curvature is not. The presence of hackles on sheeting joint faces and the lack of slip across features cut by sheeting joints (e.g., dikes, veins, xenoliths, phenocrysts, and fractures) indicates that sheeting joints are tensile fractures. The general lack of chemical alteration on sheeting joint faces suggests that sheeting joints do not open from fluid pressure, but rather from a tension induced by high compressive stresses acting parallel to a curved topographic surface. Further evidence of high, surface-parallel compressive stresses is present in the form of buckled sheeting joint slabs. Measurements by Cadman (1969) and Hickman (personal communication, 3/2008) indicate that surface-parallel stresses are highly compressive (on the order of -10 MPa) in the Yosemite region. The study area is on the verge of nucleating additional sheeting joints given stresses of this magnitude and the curvature and slope of the topography.

The presence of many sheeting joints at TC Dome study area is consistent with modern topographic and stress conditions. Compressive stresses parallel to the surface are likely to have absolute magnitudes of at least 14 MPa and could be as high as 25 MPa. The upper portion of TC Dome is doubly-convex; however much of the lower surface is saddle-shaped, likely the result of glacial erosion. Sheeting joints at the lower portion of TC Dome requires no more than 4.3 meters of erosion of the topographic surface since the joints formed. Glacial erosion could have accomplished this.

The sheeting joint distribution everywhere at TC Dome cannot be accounted for entirely by current topographic and regional stress conditions. The sheeting joints on the doubly convex upper portions of the dome can be accounted for, both in terms of their distribution and the orientation parallel to topography. Current topography and stress conditions do not account for sheeting joints at the base of the dome in domains 1 and 2. Sheeting joints of domain 1 are closely spaced, nearly horizontal, and are oblique to the topographic surface. In domain 2, sheeting joints have an unusual geometry, dipping steeply towards fracture F2. Both differences can be accounted for by plausible local stress variations and erosion. The nearly horizontal sheeting joints in domain 1 can be accounted for, at least in part, if the topography across Tenaya Creek were doubly convex when the joints formed. The stress trajectories beneath a cusp-shaped valley are consistent with sub-horizontal sheeting joints develop near the cusp. With a few meters of glacial and stream erosion, the flat sheeting joints would be exposed. The close spacing of sheeting joints in domain 1 and unusual geometry in domain 2 can be accounted for if fracture F2 were activated as a thrust fault prior to sheeting joint formation. A tensile stress concentration caused by the fault could account for the closely spaced sheeting joints in domain 1. Trajectories of most compressive stress (a proxy for sheeting joint orientation) roll toward the fault, thus accounting for the sheeting joints in domain 2 steeply dipping toward fracture F2. Subtle geologic factors and topographic modification need to be considered to account for the sheeting joints low on TC Dome; presumably they would need to be considered in other places as well.

Figures



Figure 1. Sheeting joints sub-parallel to topography on Shuteye Peak, California (USGS n.d.).
Photograph taken by N.K. Huber.

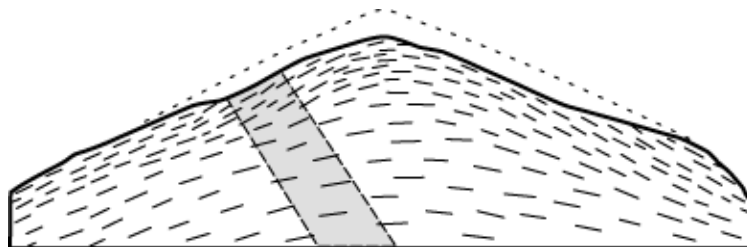


Figure 2. Sketch depicting sheeting joints in cross-section (from Martel, 2006). The gray band represents a dike.



Figure 3. Photograph looking south at Tioga Road (Highway 120) quarry wall near Olmsted Point, Yosemite National Park. As seen in this photograph, sheets generally tend to be thicker with increasing depth below the surface. A geologist can be seen above the quarry for scale.

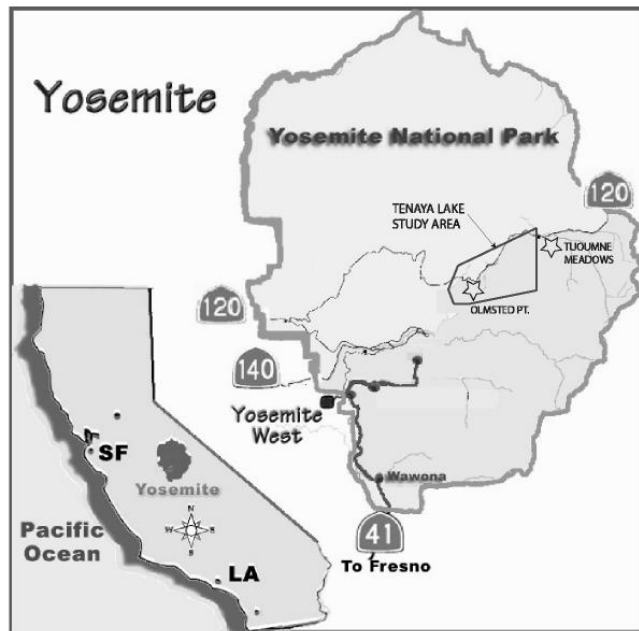


Figure 4. Location of Yosemite National Park and the Tenaya Lake study area (modified from Wikipedia, 2007).

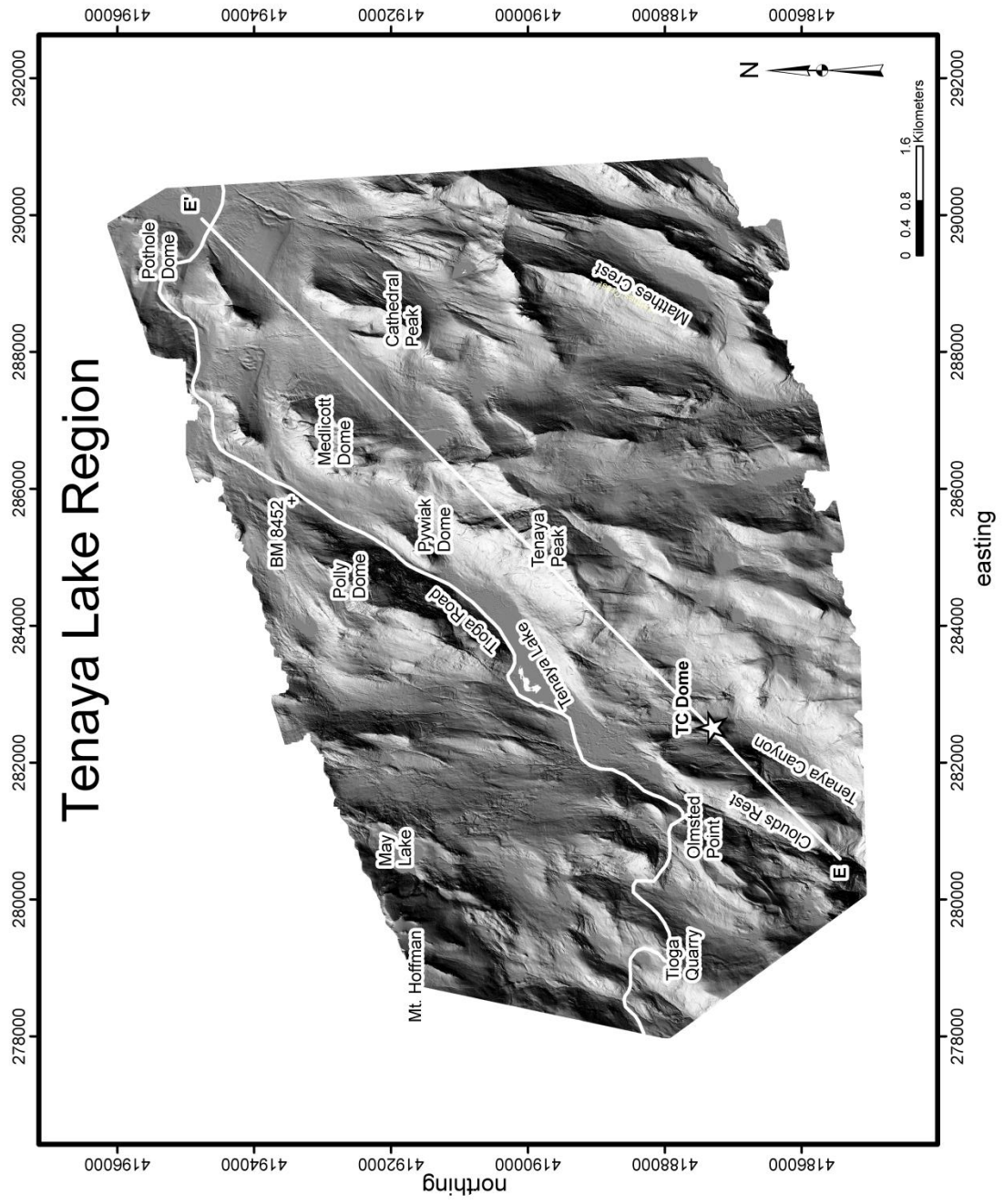


Figure 5. Shaded relief map of Tenaya Lake study area. E-E' is the line of cross-section in Fig. 43. The star at TC Dome marks the site of detailed field investigation.

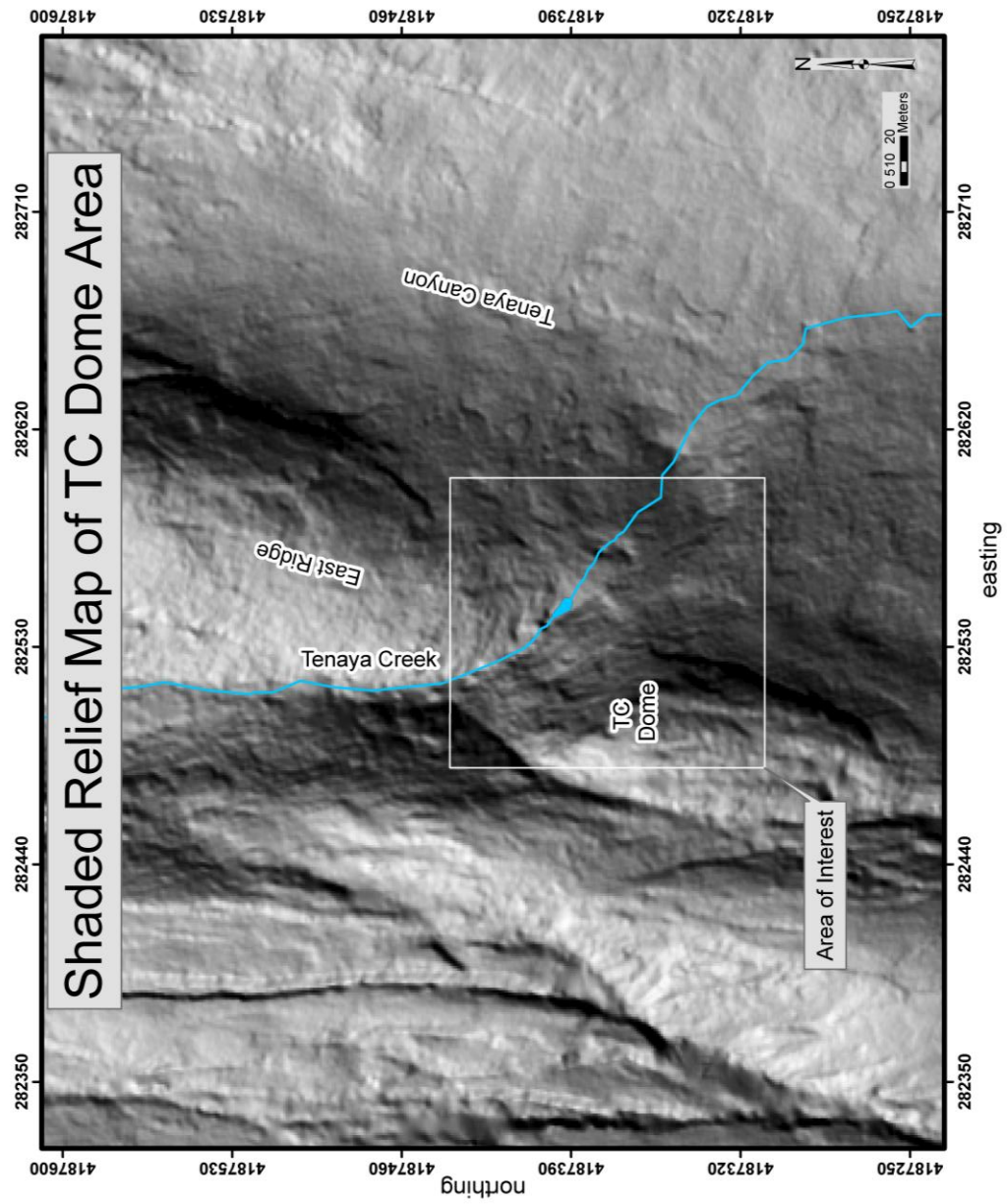


Figure 6. Shaded relief map of region surrounding TC Dome study area (outlined in white).

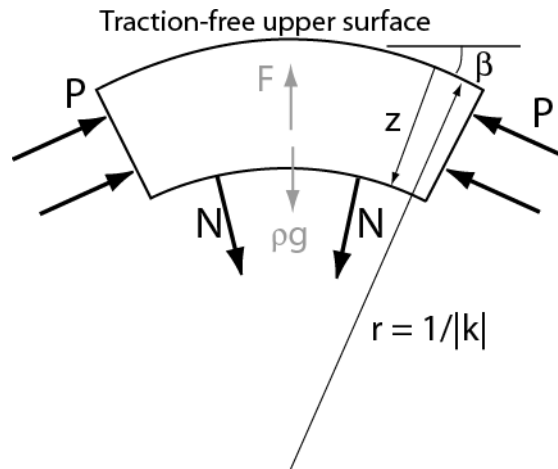


Figure 7. Free body diagram showing a rock element with a convex, traction-free upper surface, compressive end loads (P), and a lower surface subject to normal tractions (N). If body forces ρg are absent, and P is compressive, then N must be tensile for the forces to be in equilibrium (adapted from Martel, 2006).

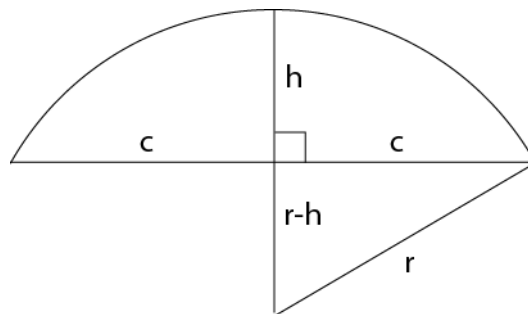


Figure 8. Diagram of a segment bounded by a circular arc of radius of (r) and a chord of half-length (c). The segment height is h . The curvature may be calculated using the half chord length and the segment height (equation 8).

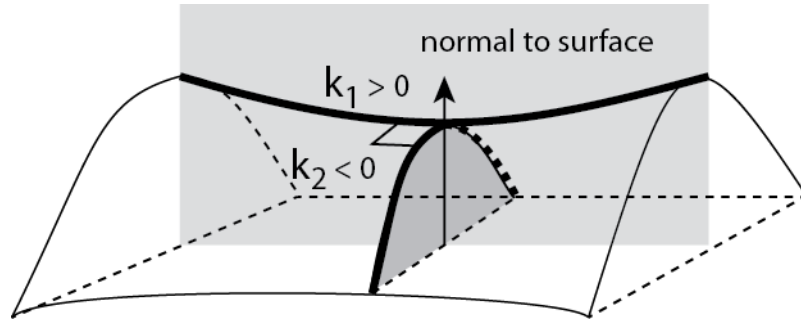


Figure 9. Diagram of a saddle-shaped surface. Gray planes shown contain the surface normal and intersect the saddle in plane curves that yield the principal curvatures for the surface.

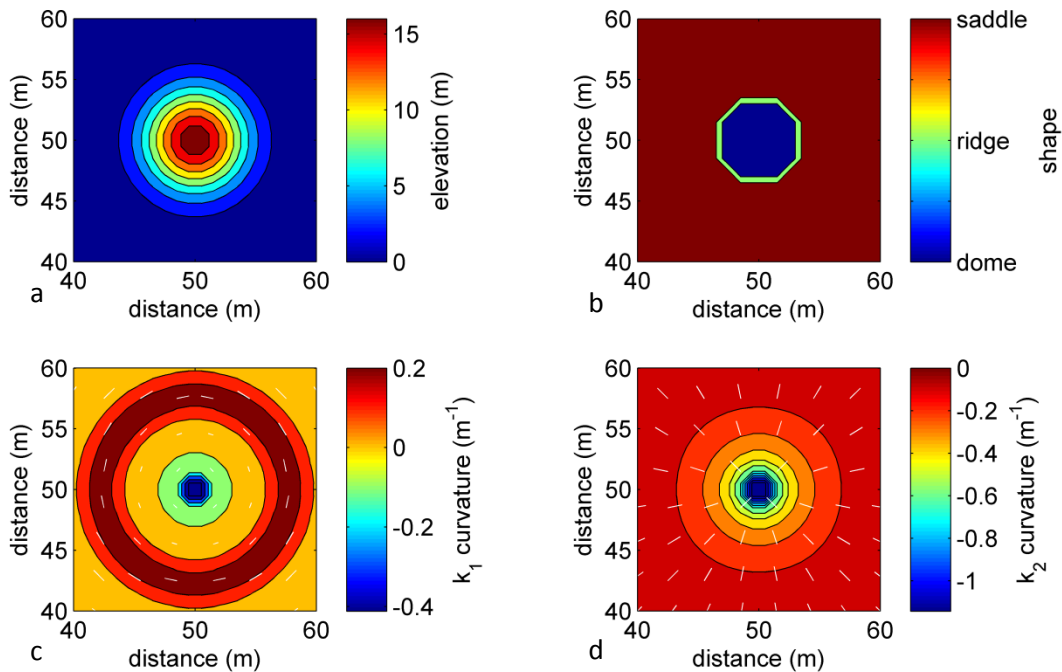


Figure 10. Geometry of a bell-shaped hill. (a) Topographic contour map. (b) Topographic shapes on the hill. The hill is doubly-convex, or dome-shaped. At points within the green band k_1 is zero and k_2 is negative, thus the local geometry is akin to that of a cylindrical ridge. The base of the hill is a saddle because k_1 is positive and k_2 is negative. (c) Maximum principal curvature (k_1), with ticks showing the direction of maximum curvature. (d) Minimum principal curvature (k_2), with ticks showing the direction of minimum curvature. This bell-shaped hill resembles several domes in Yosemite National Park (e.g., Lembert Dome).

a



b



Figure 11. Photographs of heavily weathered sheeting joints in the porphyritic Cathedral Peak Granodiorite. Much of the topographic surface in both locations is glacially polished. (a) Sheeting joints on Pothole Dome that are not sub-parallel to the topographic surface. (b) A sheeting joint cutting phenocrysts and a small dike on a dome near BM 8452, with no visible offset. Note pencil for scale. The lack of offset suggests that sheeting joints are mode I (tensile) fractures rather than mode II or III (shear) fractures.

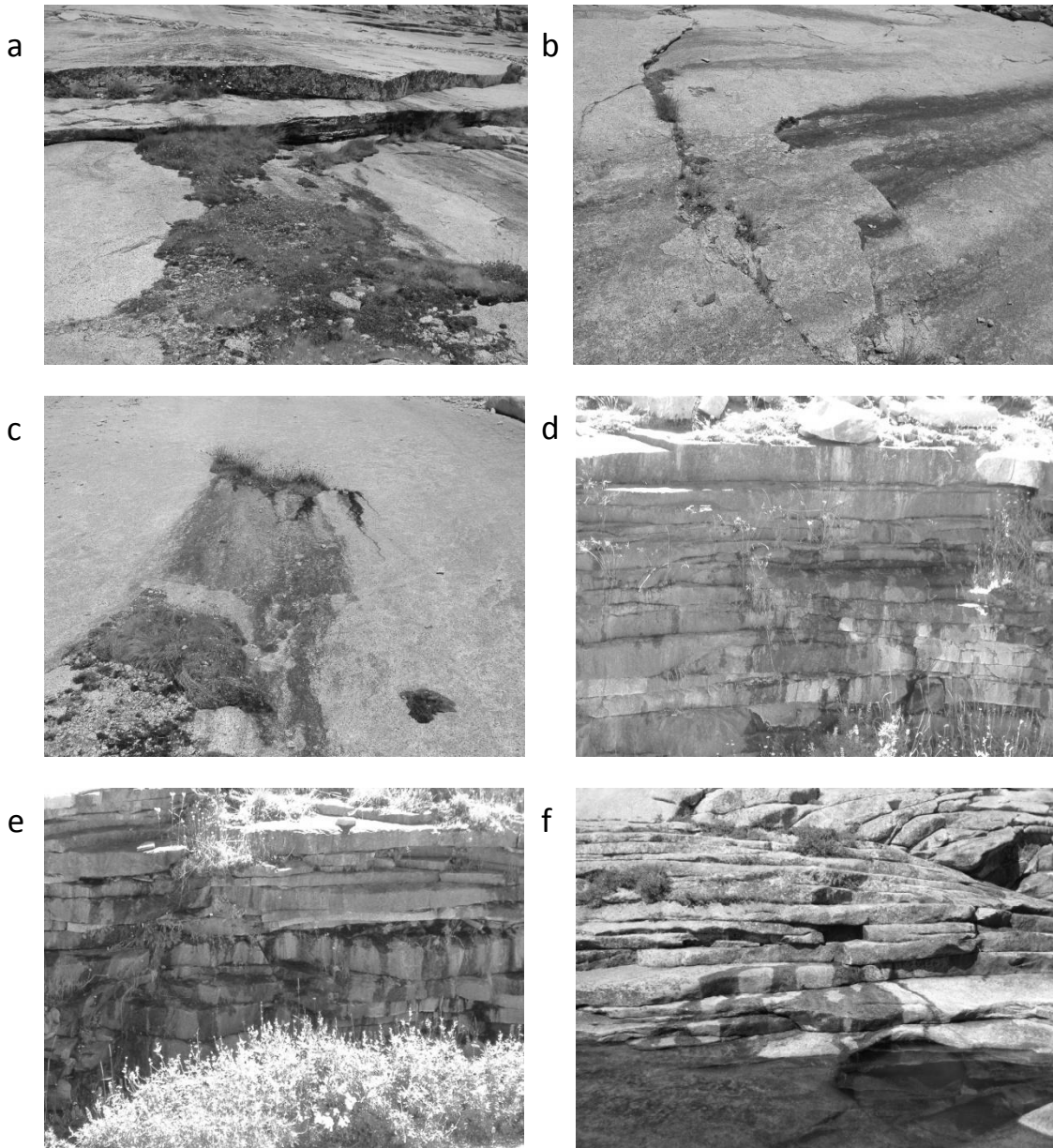
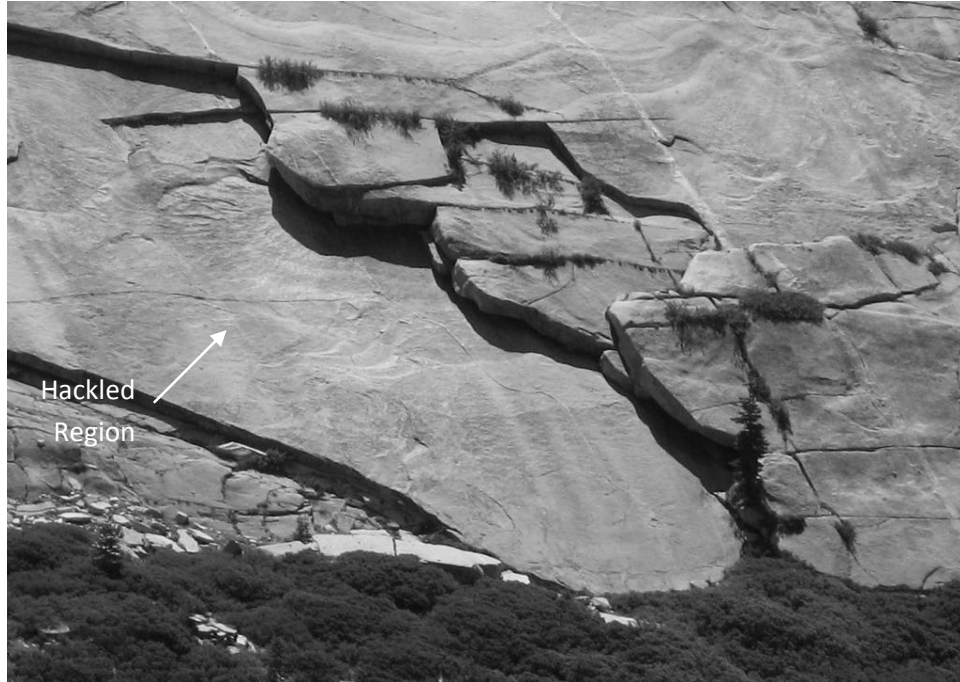


Figure 12. Photographs of sheeting joints seeping water. Photographs (a- c) are taken northeast of Olmsted Point, below Tioga Road; (d and e) show road-cuts along Tioga road; and (f) shows TC Dome the day after a heavy rainstorm.

a



b



Figure 13. Photographs of hackles on sheeting joint faces. (a) View southeast toward the northwestern face of "Quarry Ridge". (b) View northeast to Pywiak Dome.

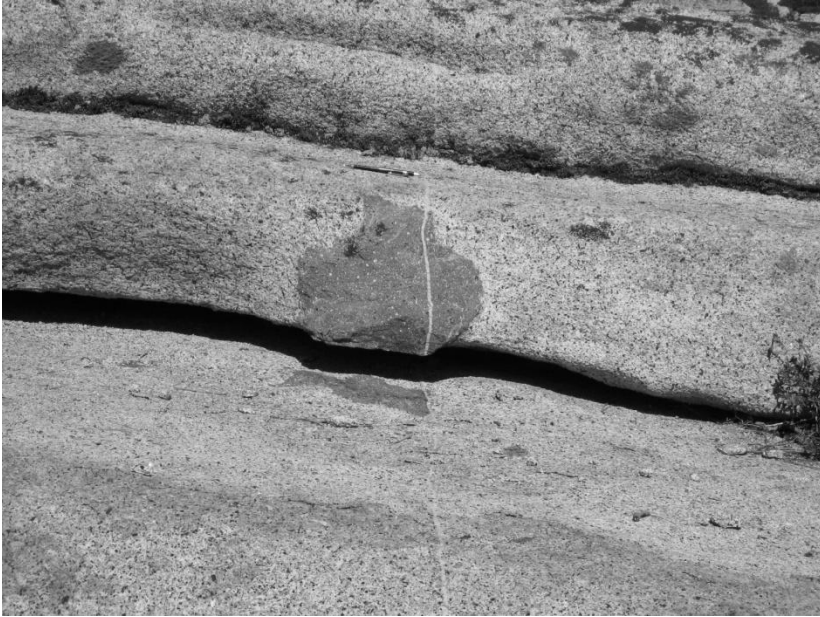


Figure 14. Sheeting joint cutting (but not offsetting) a xenolith and a vein near the top of TC Dome. A pencil above the xenolith is shown for scale.



Figure 15. View south from Tenaya Creek to TC Dome. Virtually the entire north face of the dome consists of sheeting joint faces or sheeting joint traces.



Figure 16. View southeast of TC Dome from East Ridge. Fractures F2 and F3 divide the lower portion of the dome into domains (1) and (2), in which sheeting joint geometry is not sub-parallel to topography. Sheeting joints on the upper two-thirds of the dome are sub-parallel to topography, hence fewer sheeting joint traces are observed there than near the base of the dome. The spacing of sheeting joints is smaller at (1) than at (2).



Figure 17. View northeast to East Ridge. The green line marks the approximate extent of fracture map on Figure 20. Dike D1 extends further than shown. The east side of the ridge faces Tenaya Canyon and displays extensive glacial polish. Sheets on the ridge tend to be more heavily fractured than those on TC Dome.



Figure 18. View south-southeast of the base of TC Dome. Sheeting joints in domain 1 tend to be nearly horizontal. Their geometry changes little as they approach fracture F2. The sheeting joints in domain 2, however, curve as they approach F2.

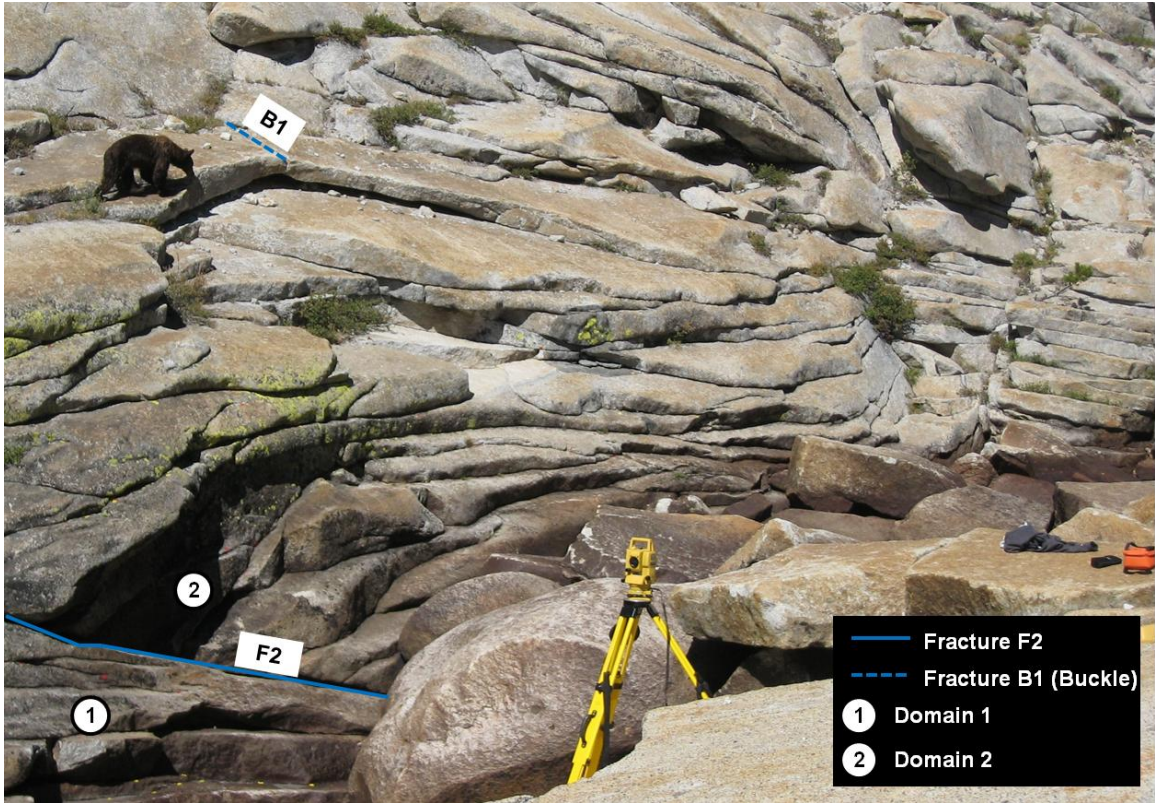


Figure 19. View looking south-southwest to the base of TC Dome. Fracture F2 divides sheeting joints into domains 1 and 2 is shown in blue. A buckled sheet (fracture B1) is shown as a dashed blue line, near the bear. The presence of buckled sheets indicates that the area has experienced high surface-parallel compressive stresses since glaciation.

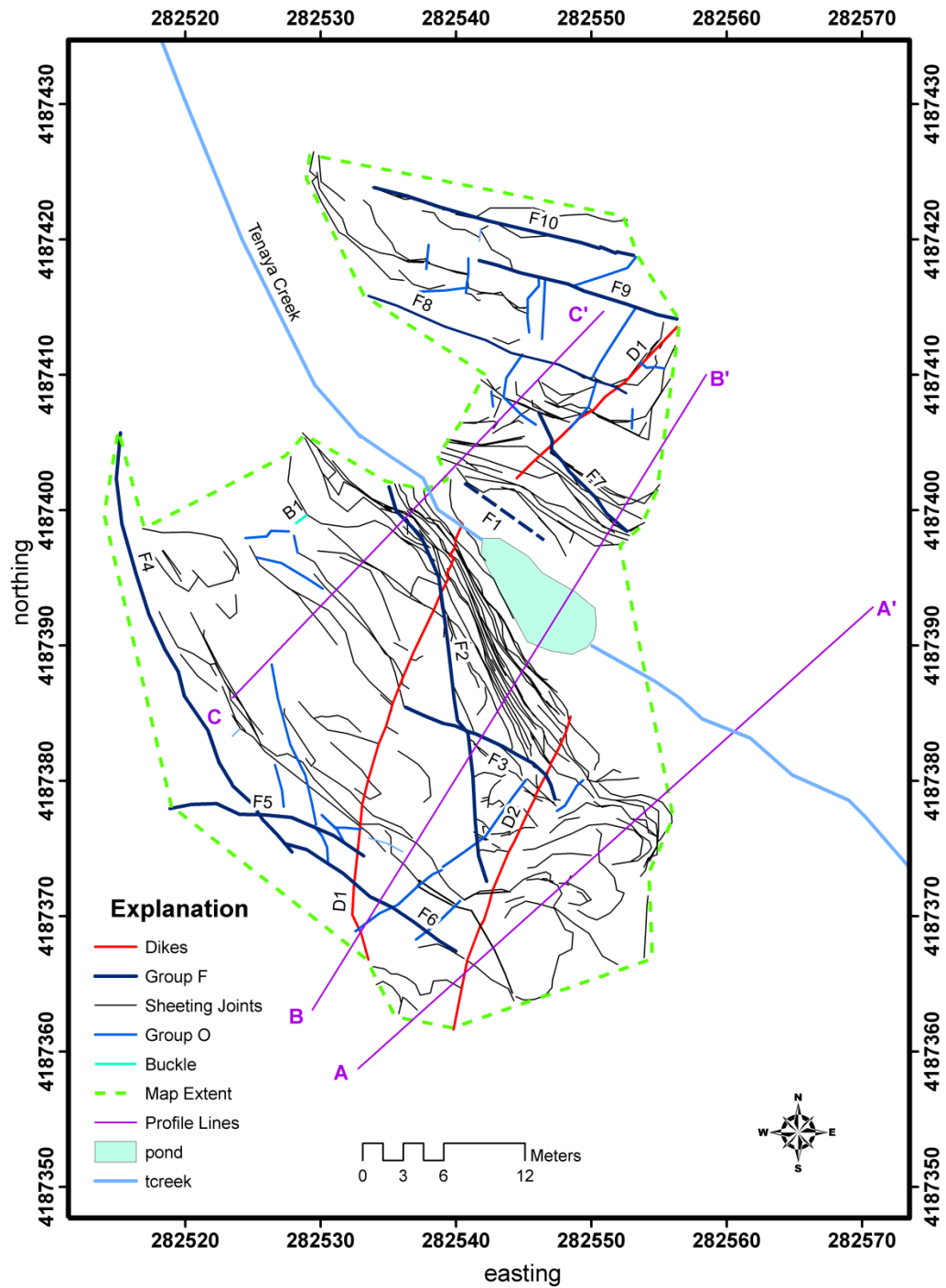


Figure 20. Fracture map of TC Dome study area. The bottom edges of sheets were mapped. Sheeting joints are shown in black, dikes in red and other fractures in blue. Structures in the explanation are listed from oldest (dikes) to youngest (buckle). Fractures from this map are shown in many subsequent figures for reference.

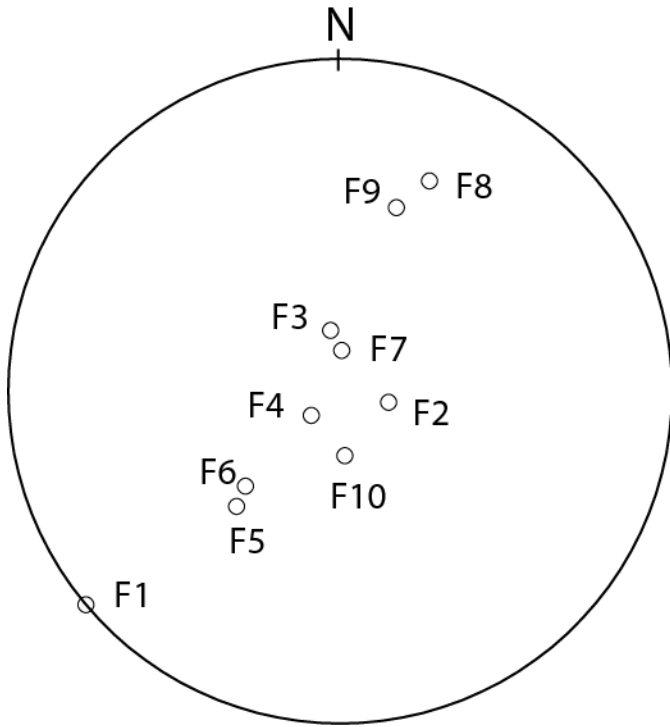


Figure 21. Stereographic projection of poles to fractures F1-F10.

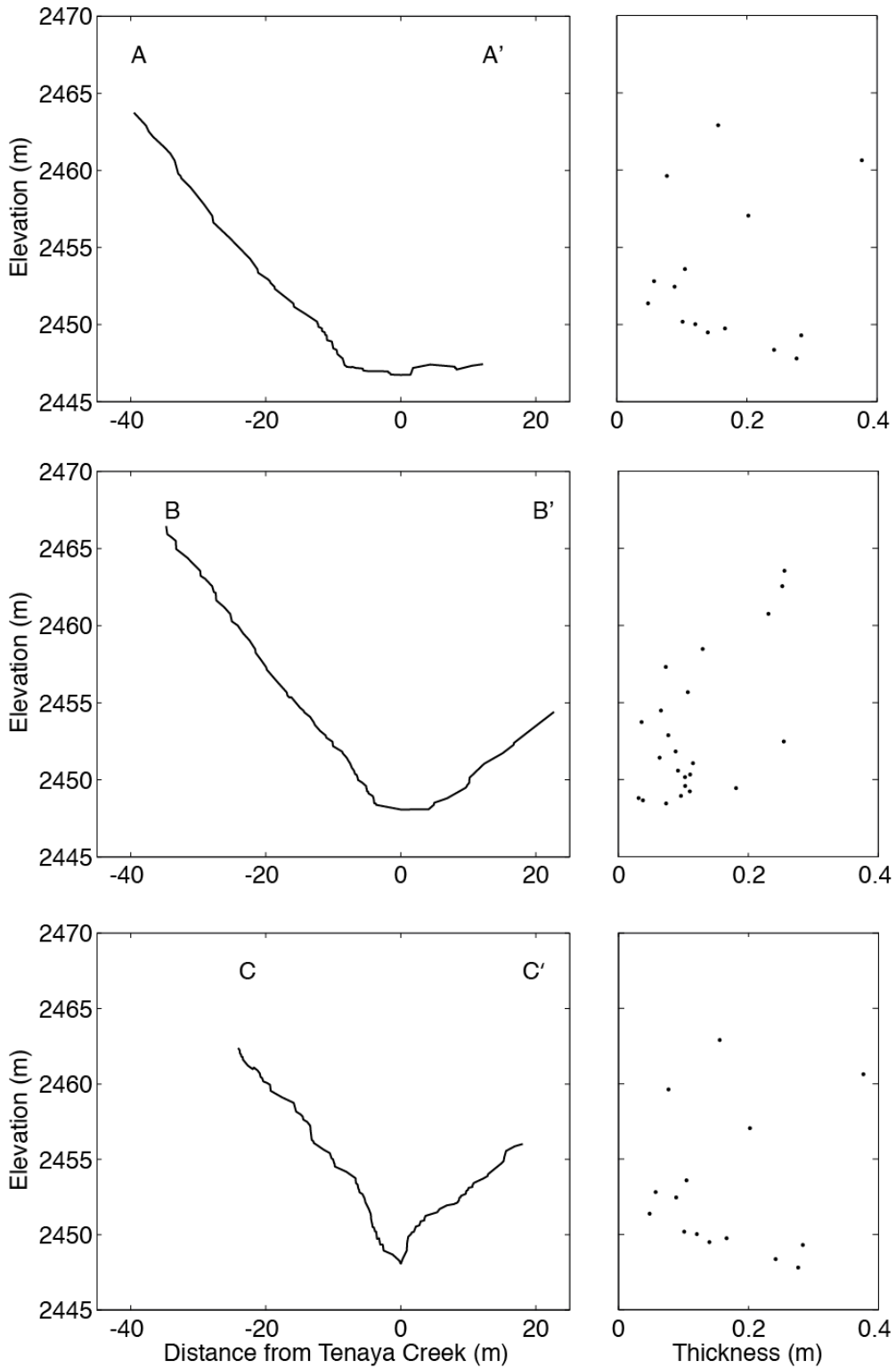


Figure 22. Topographic profiles (from Fig. 20) and sheet thickness at TC Dome. Steps marking the closely spaced, horizontal sheeting joints of domain 1 are seen in B-B' below 2452 m elevation. Steps marking domain 2 sheeting joints are shown in C-C' below 2454 m elevation.

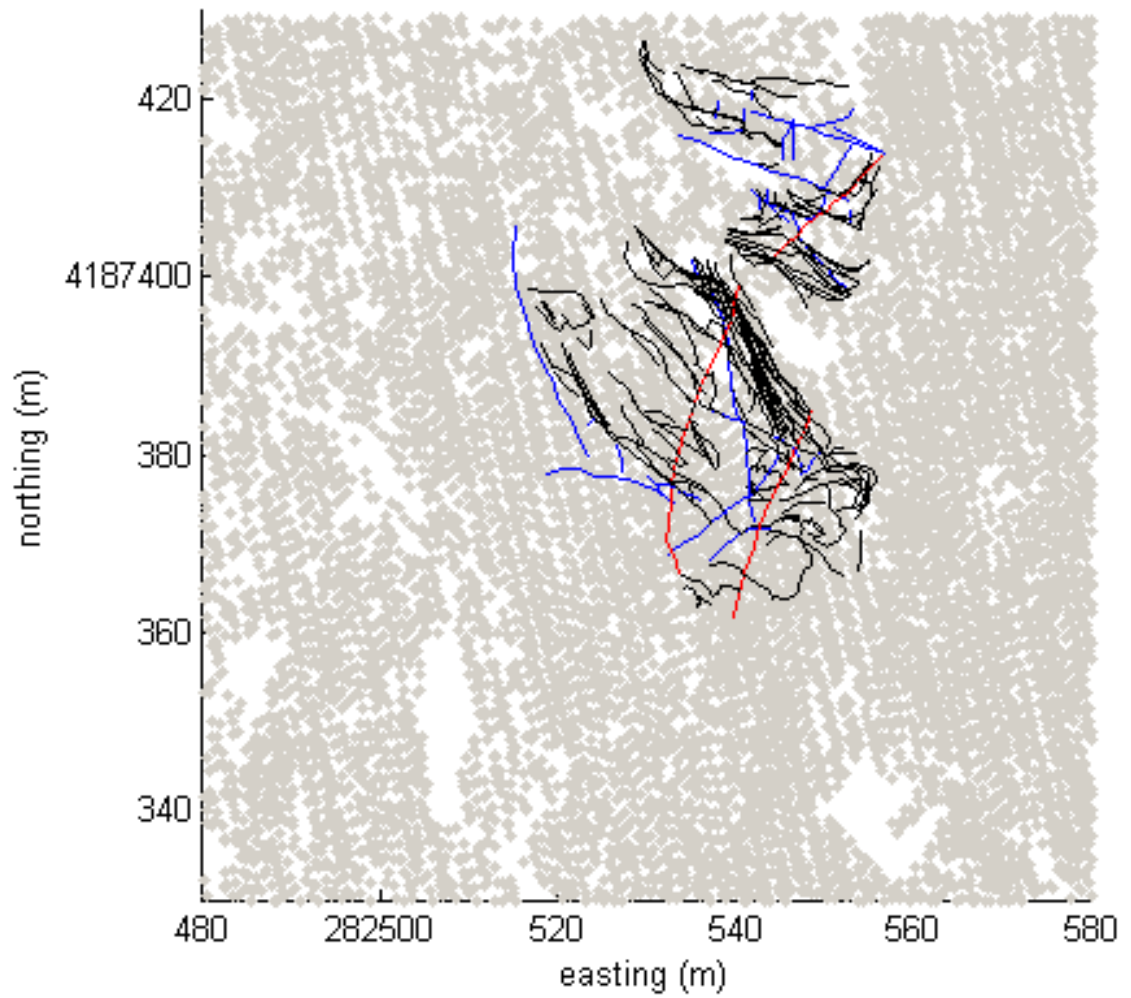


Figure 23. LIDAR point cloud data coverage (grey dots) for TC Dome study area. Large white patches indicate areas with no data. Fractures from Fig. 20 are overlain for reference.

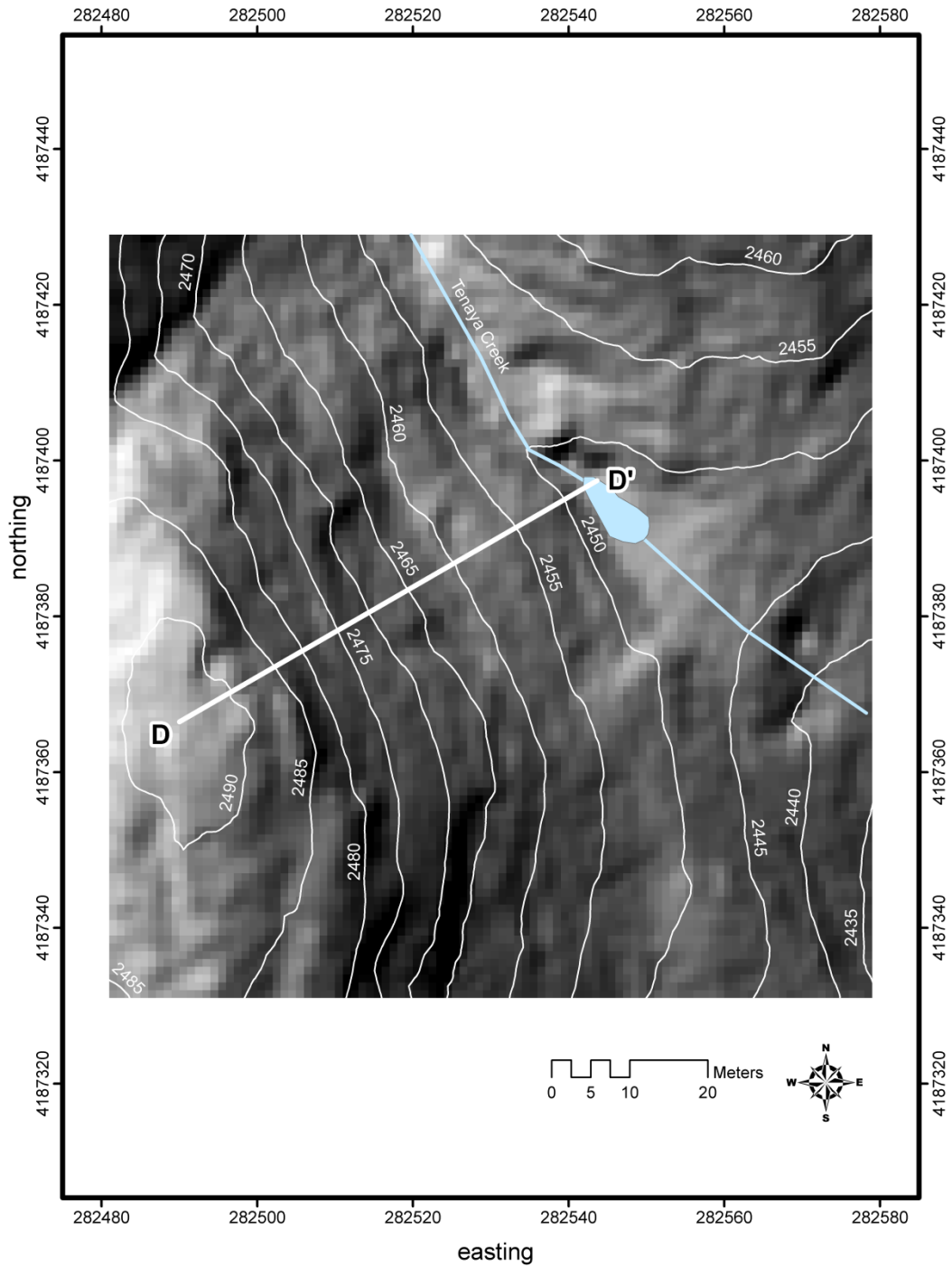


Figure 24. Topographic contour map overlain on shaded relief digital elevation model from filtered aerial LIDAR data on a 1-m grid. Profile D-D' is shown in Fig. 45.

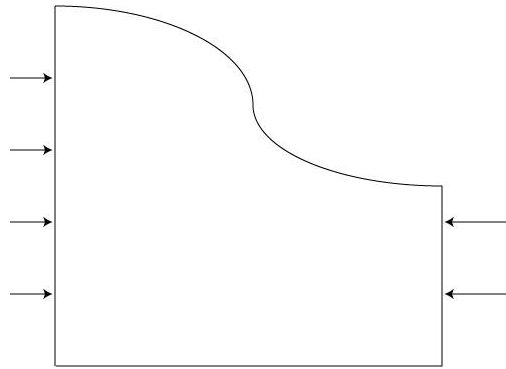


Figure 25. Lateral force balance diagram. The horizontal stresses below the valley must be more compressive on average than those below the hill in order to maintain a force balance.

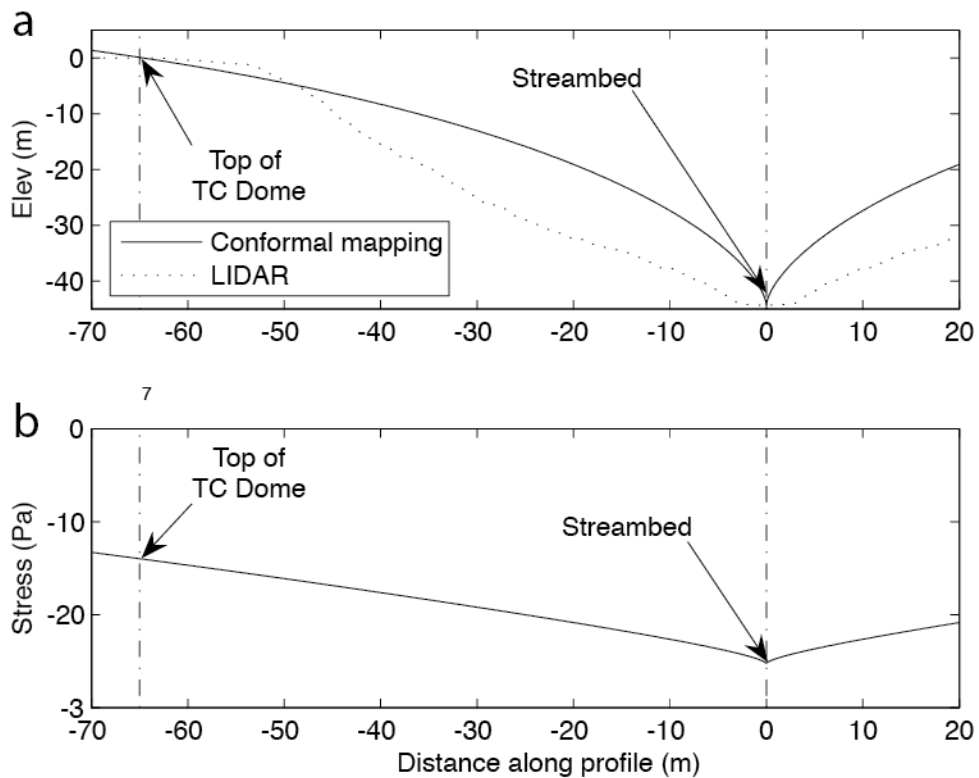


Figure 26. Topography and modeled stress along the surface. (a) Shows a convex surface grossly representing a topographic profile trending N60°E at TC Dome. (b) The modeled surface-parallel stress along the surface (P) ranges from -14 MPa at the top of the dome to -25 MPa at the streambed.

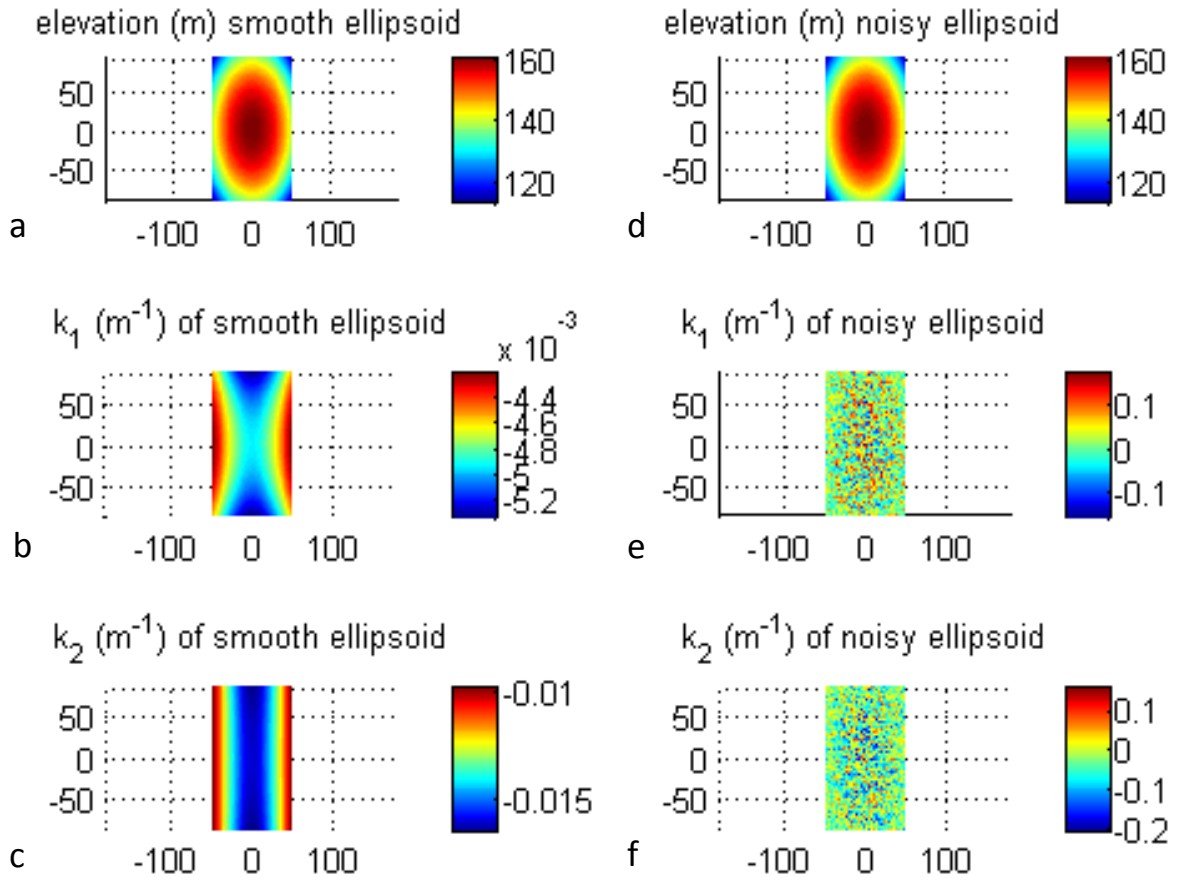


Figure 27. Curvature of an ellipsoidal surface grossly representing TC Dome. (a-c) Digital elevation model, k_1 , and k_2 of a smooth ellipsoidal surface, respectively. (d-f) Digital elevation model, k_1 , and k_2 of an ellipsoidal surface with 10 cm vertical uncertainty, respectively. The results in (e) and (f) indicate that aerial LIDAR data requires smoothing in order to obtain to obtain the overall surface-curvature in TC Dome study area.

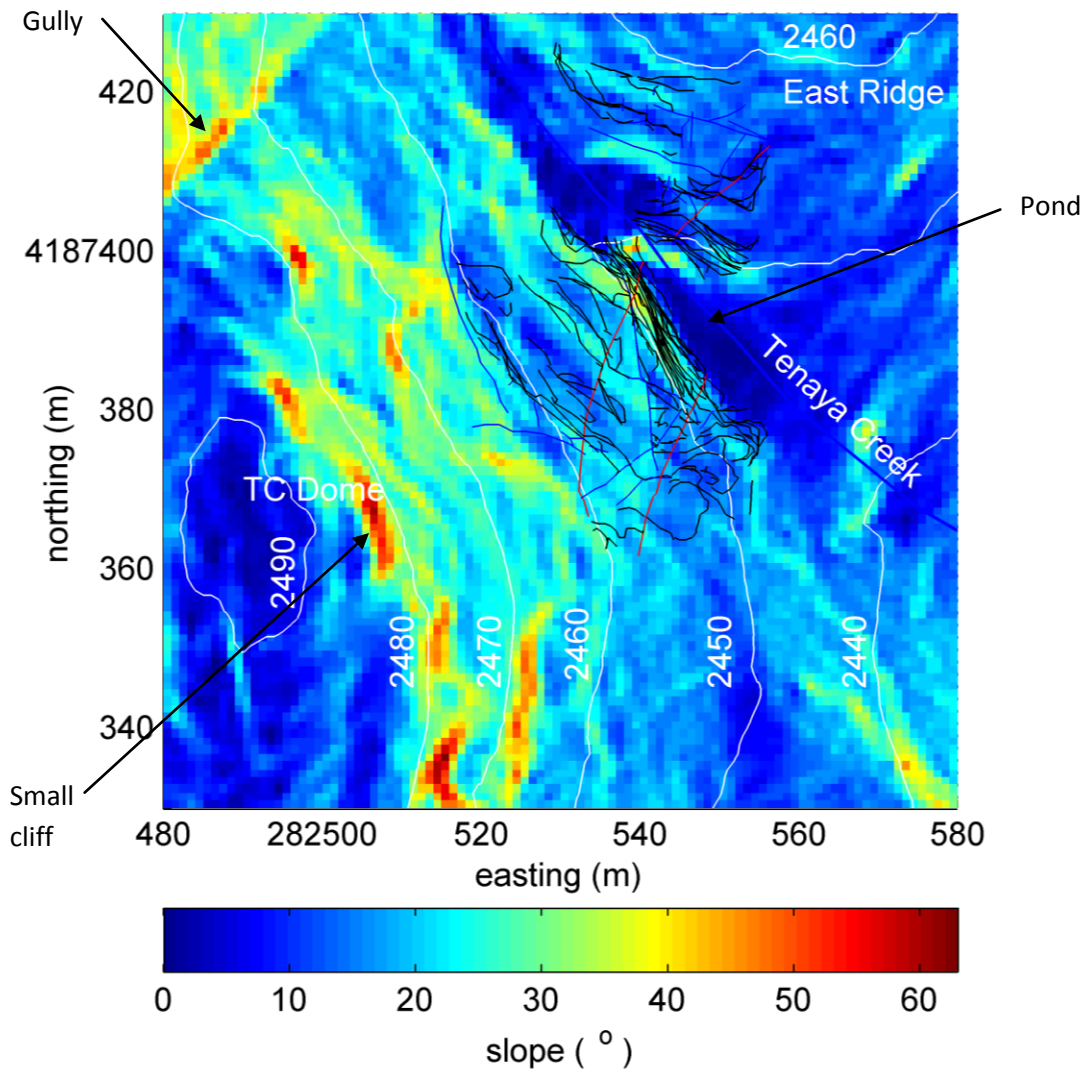


Figure 28. Slope map of TC Dome study area from unfiltered aerial LIDAR data. The slopes vary between 0° and 62° . Identifiable topographic features include the gully (Fig. 15) trending N45E in the northwestern corner, the pond in dark blue near the center of the figure, steep steps in topography such as small cliffs (red), and sheeting joint steps (yellow) seen in Figures 14-18. Contours represent elevation in meters.

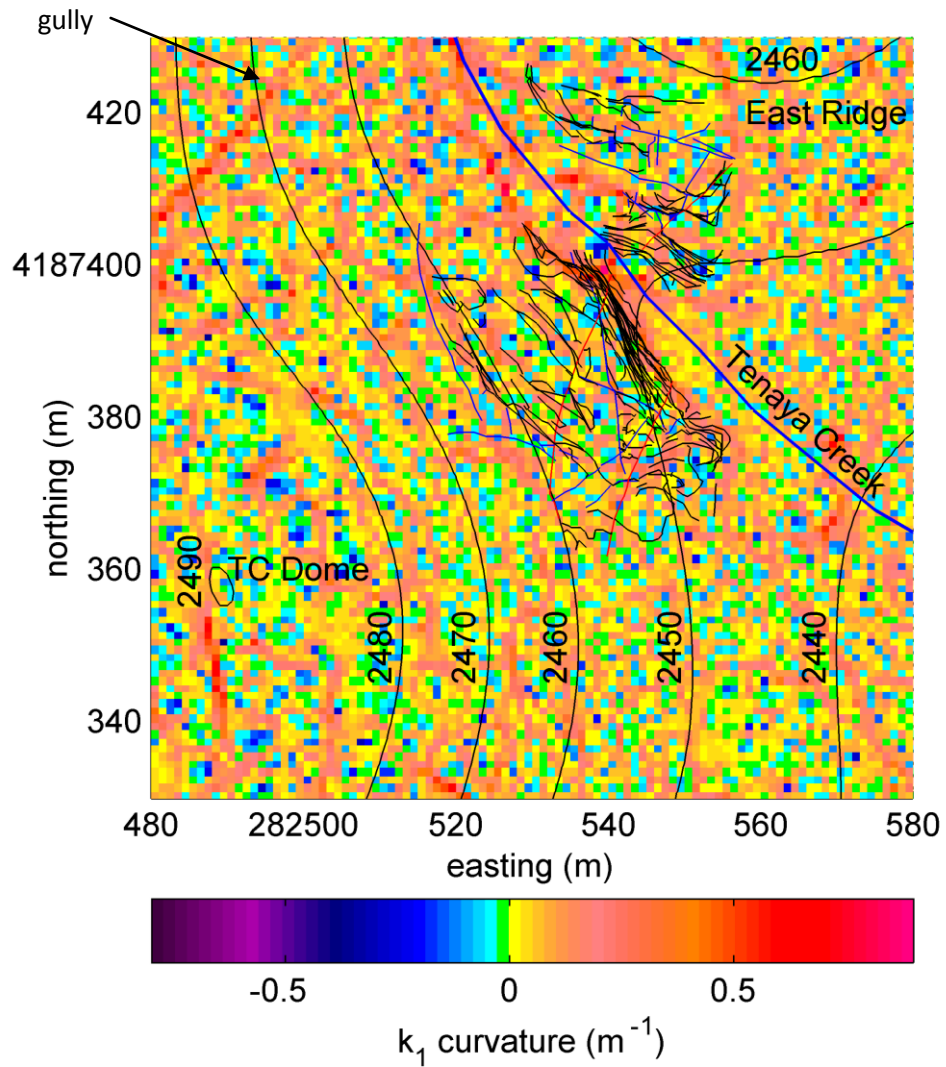


Figure 29. Maximum principal curvature (k_1) map of TC Dome study area from unfiltered aerial LIDAR data. Curvature values shown here vary between -0.43 and 0.90 m^{-1} . The results are noisy. Contours represent elevation in meters.

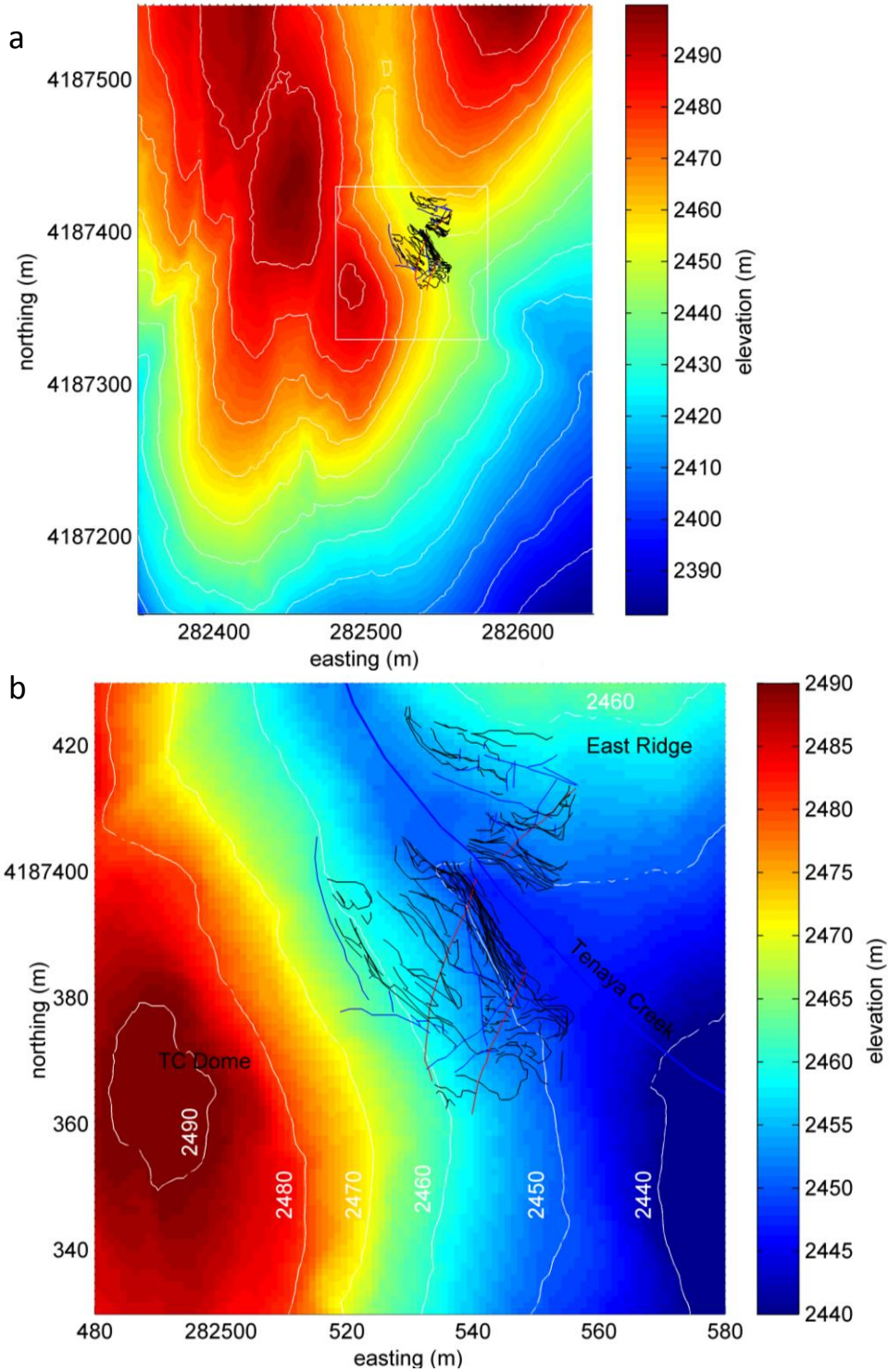


Figure 30. Unfiltered topography at TC Dome study area with elevation in meters. (a) Topography of the area to be analyzed (TC Dome and greater area) in order to reduce edge effects on TC Dome study area (white outlined box). (b) Enlarged view of TC Dome study area. Fractures from Fig. 20 are shown for reference. Contours represent elevation in meters.

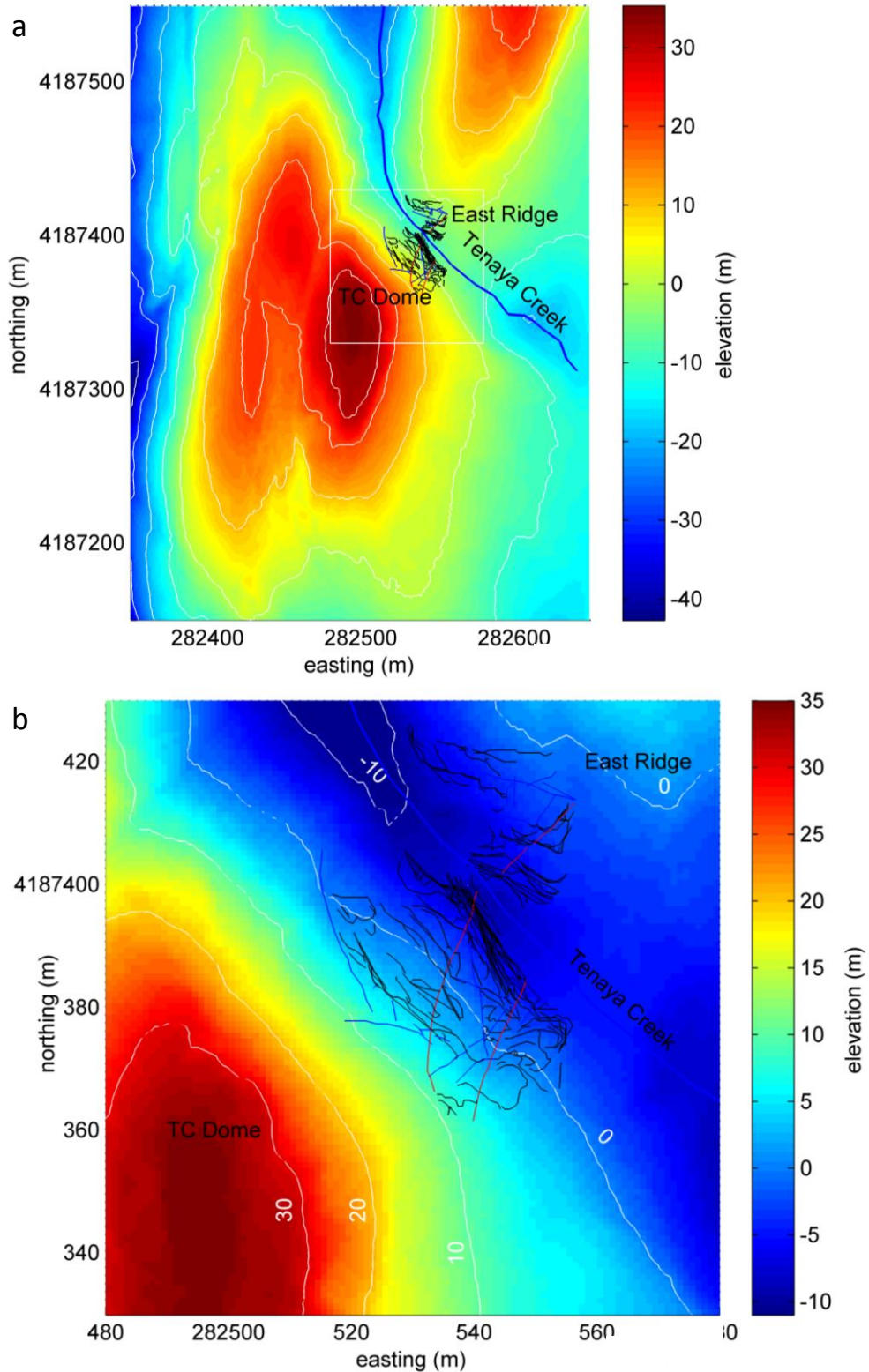


Figure 31. Unfiltered topography of TC Dome with the best fit plane removed: (a) TC Dome and the greater area (TC Dome study area outlined in white) and (b) enlarged view of TC Dome study area. Contours represent elevation in meters.

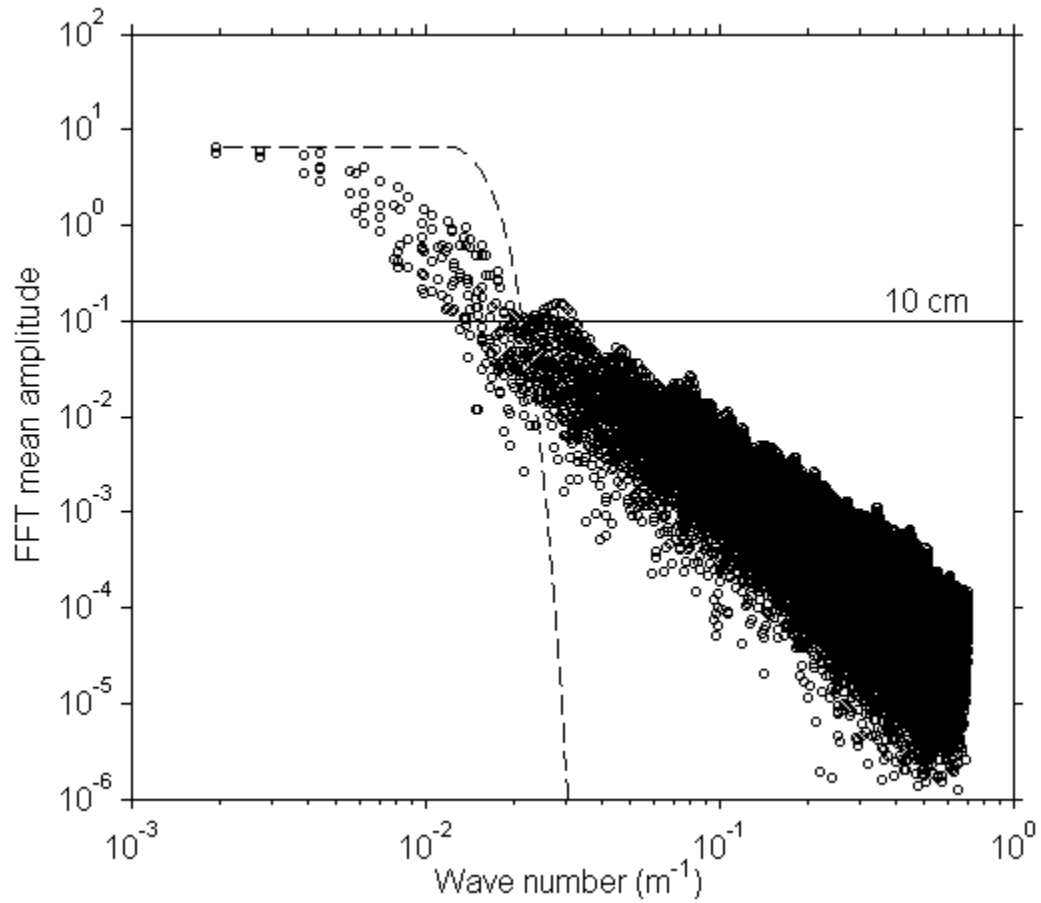


Figure 32. Log-log radial periodogram of unfiltered topographic data (after trend was removed), and the lowpass filter (dashed curve) that was used to remove high-frequency, short-wavelength signals. The circles represent mean amplitude from the fast Fourier transform, binned by radial wave number (or inverse wavelength). Data to the left and beneath the filter are kept; data to the right and above the filter are effectively removed during the filtering process.

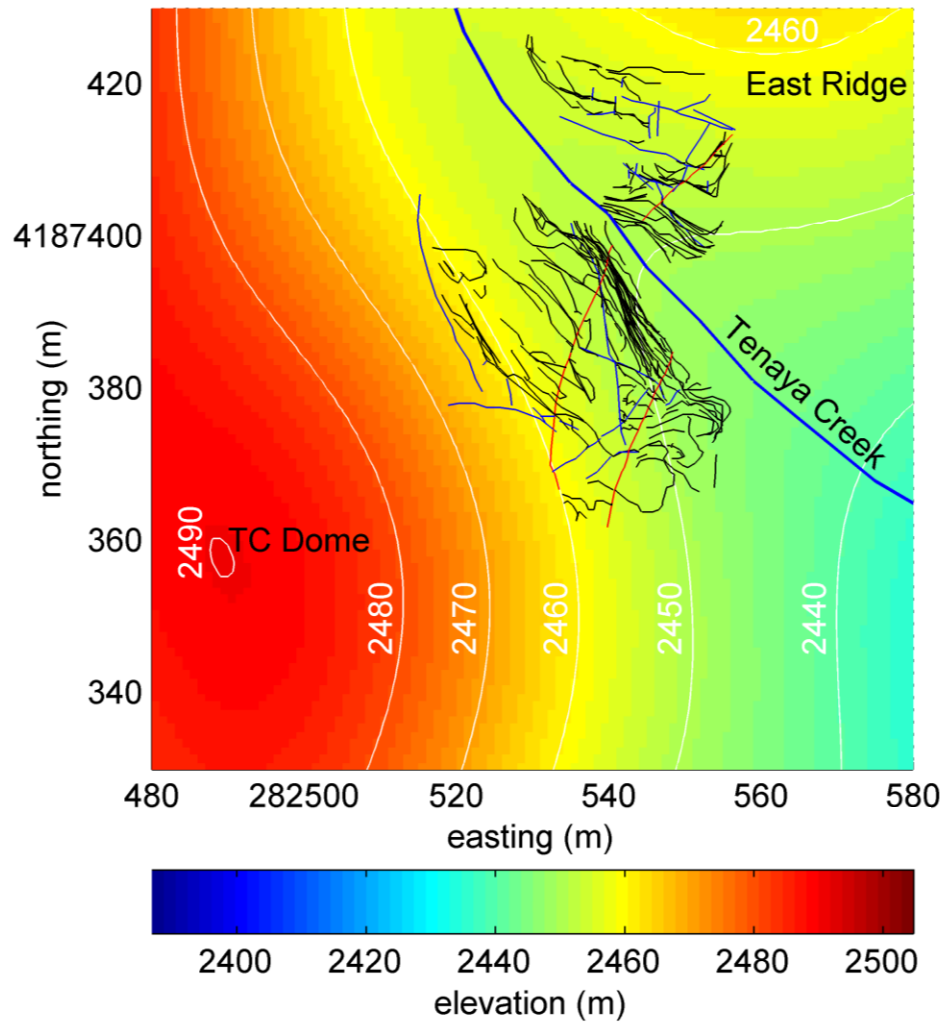


Figure 33. Filtered and re-trended digital elevation map of TC Dome study area. The overall topographic shape remains, but smaller features such as the gully (Fig. 15) are no longer visible. Contours represent elevation in meters.

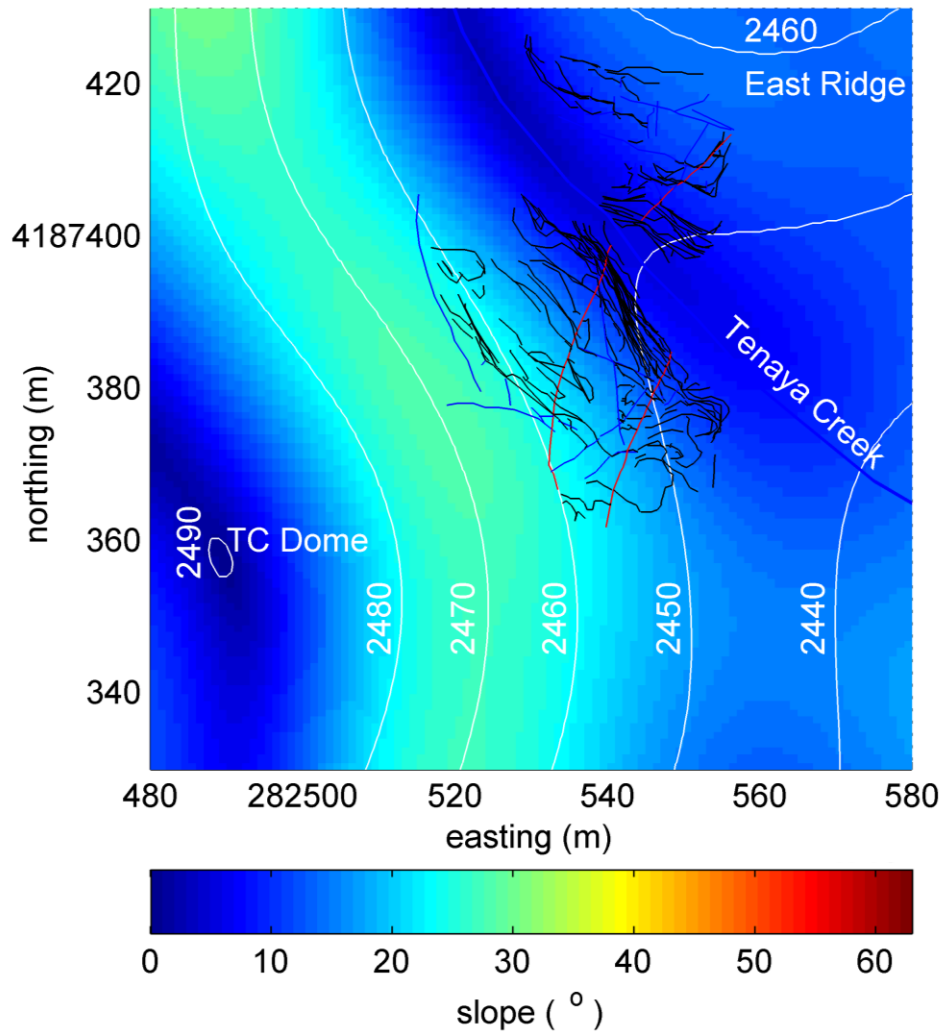


Figure 34. Filtered slope map of TC Dome study area. Slopes shown here vary between 0° and 28° . Individual features such as steps in topography caused by sheeting joints or other fracture scarps cannot be identified here. Contours represent elevation in meters.

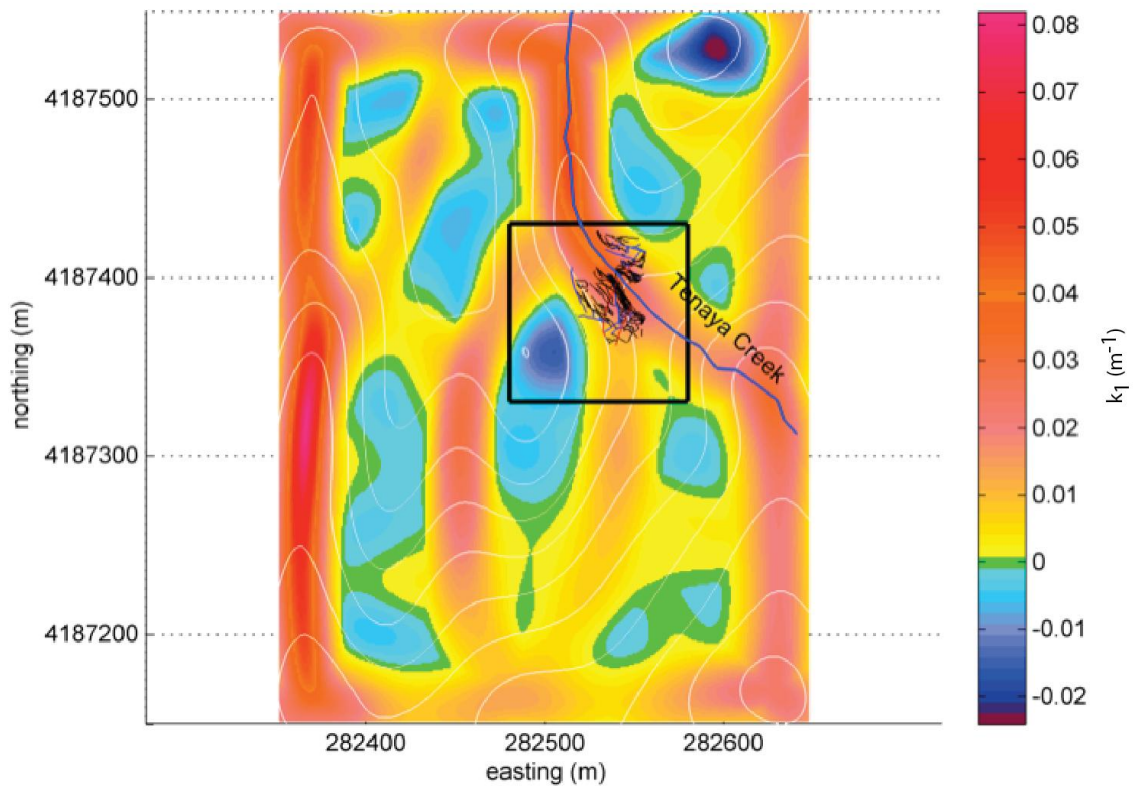


Figure 35. Maximum principal curvature (k_1) map of TC Dome and greater area from filtered aerial LIDAR data. Artifacts are seen in the results around the edges of the map; however, the area of interest (TC Dome study area) is essentially unaffected. Contours represent elevation in meters.

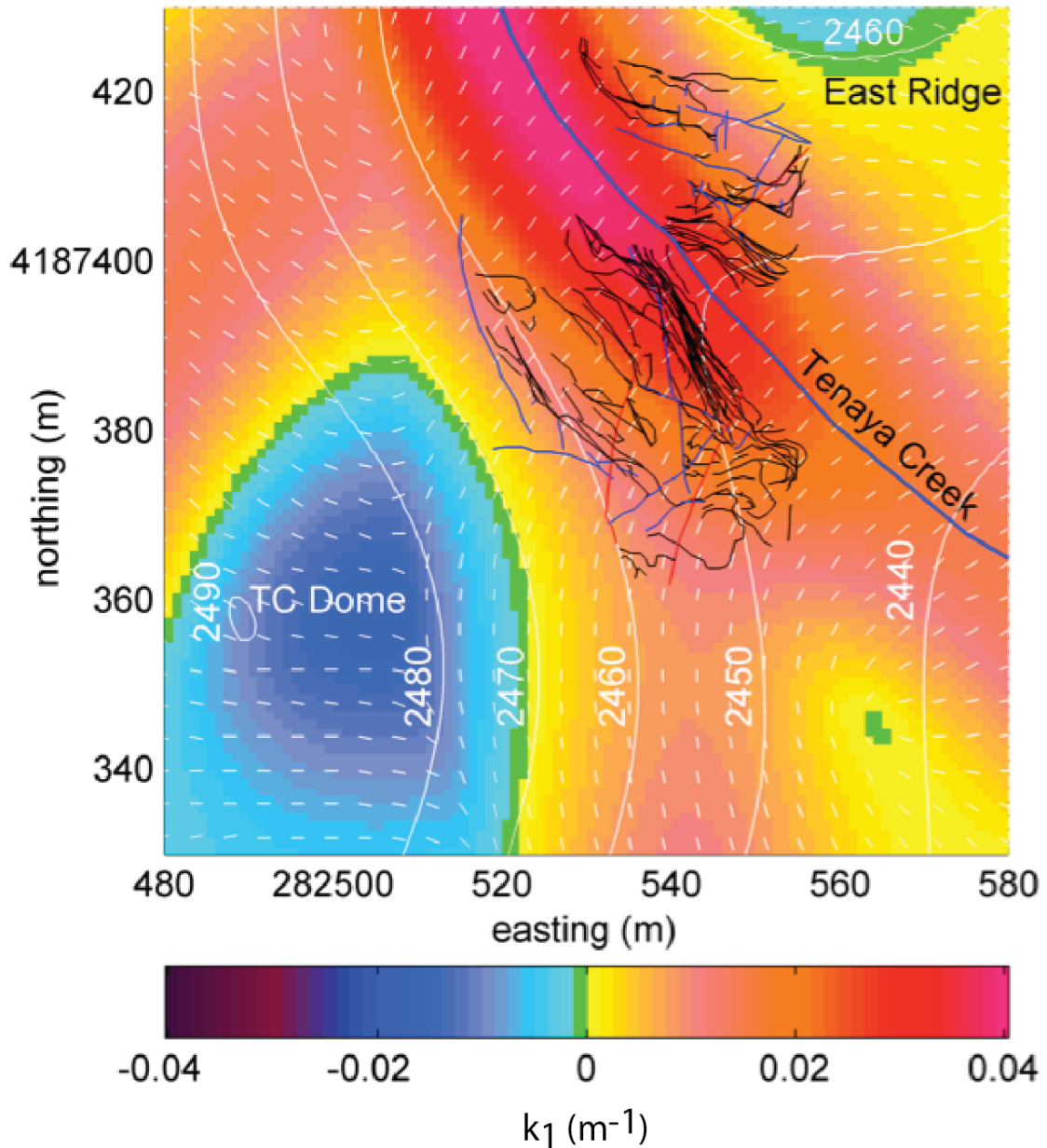


Figure 36. Maximum principal curvature (k_1) map of TC Dome study area from filtered aerial LIDAR data. Values of k_1 shown here vary between -1.6×10^{-2} and $4.0 \times 10^{-2} \text{ m}^{-1}$. White tick marks indicate the trend of k_1 . The fractures from Fig. 20 are overlain for reference. Two areas of negative (convex) k_1 values are shown here: the upper portion of TC Dome and a portion of East Ridge. The green patch in the southeastern corner ($\sim 282560 \text{ m}$ easting, $\sim 4187340 \text{ m}$ northing) is located in an area with no aerial LIDAR data and is likely an artifact from gridding. The valley of Tenaya Creek is marked by positive (concave) values of k_1 . Contours represent elevation in meters.

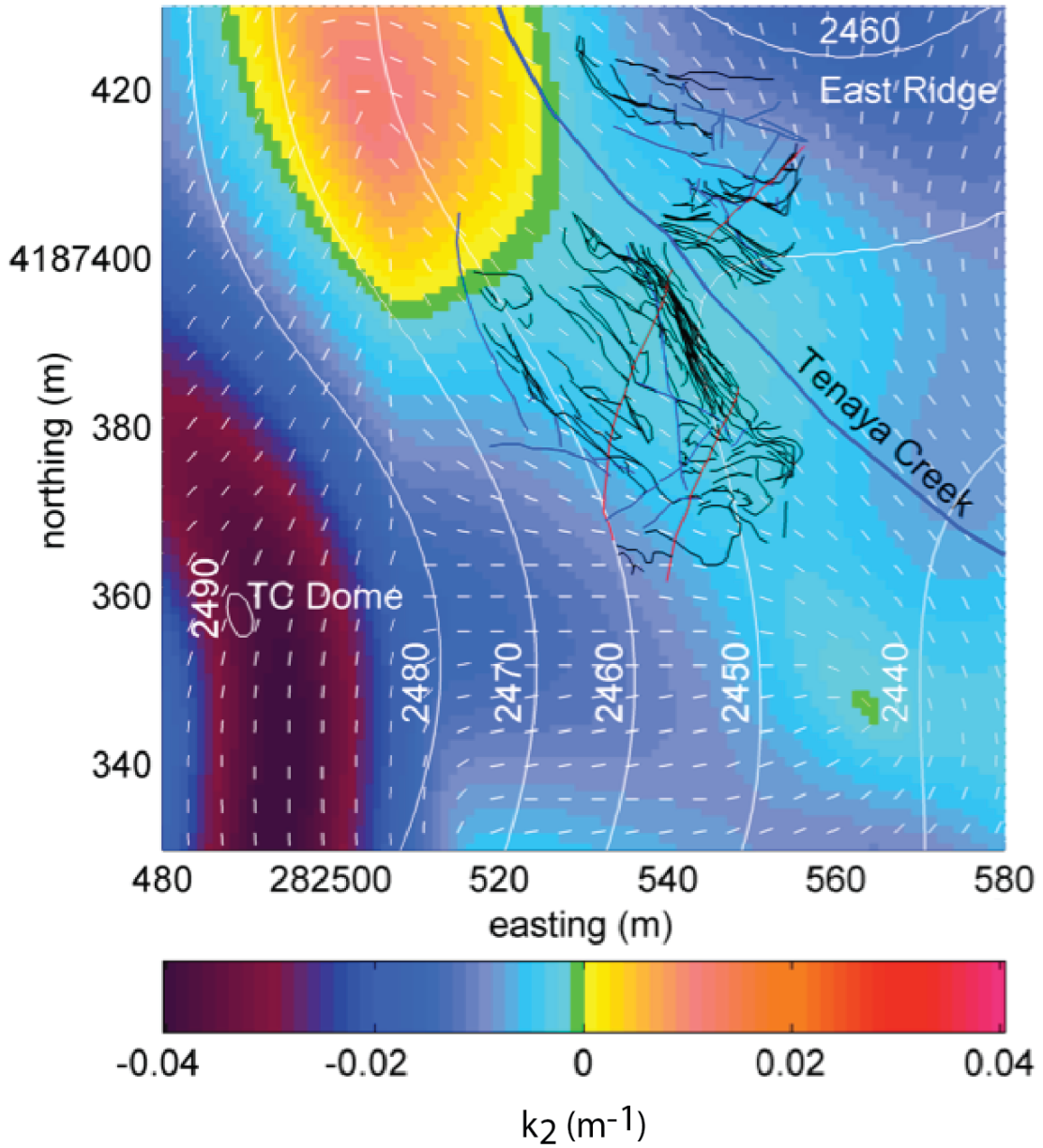


Figure 37. Minimum principal curvature (k_2) map of TC Dome study area from filtered aerial LIDAR data. Values of k_2 shown here vary between $-4.0 \times 10^{-2} \text{ m}^{-1}$ and $-1.1 \times 10^{-2} \text{ m}^{-1}$. For 90% of the area, k_2 is negative (i.e., 90% of the area is convex in at least one direction). White tick marks indicate the trend of k_2 . Fractures from Fig. 20 are overlain for reference. The green patch in the southeastern corner ($\sim 282560 \text{ m}$ easting, $\sim 4187340 \text{ m}$ northing) is located in an area that had no aerial LIDAR data and is likely an artifact from gridding. TC Dome, ridge, and much of Tenaya Creek streambed have negative (convex) curvature. Contours represent elevation in meters.

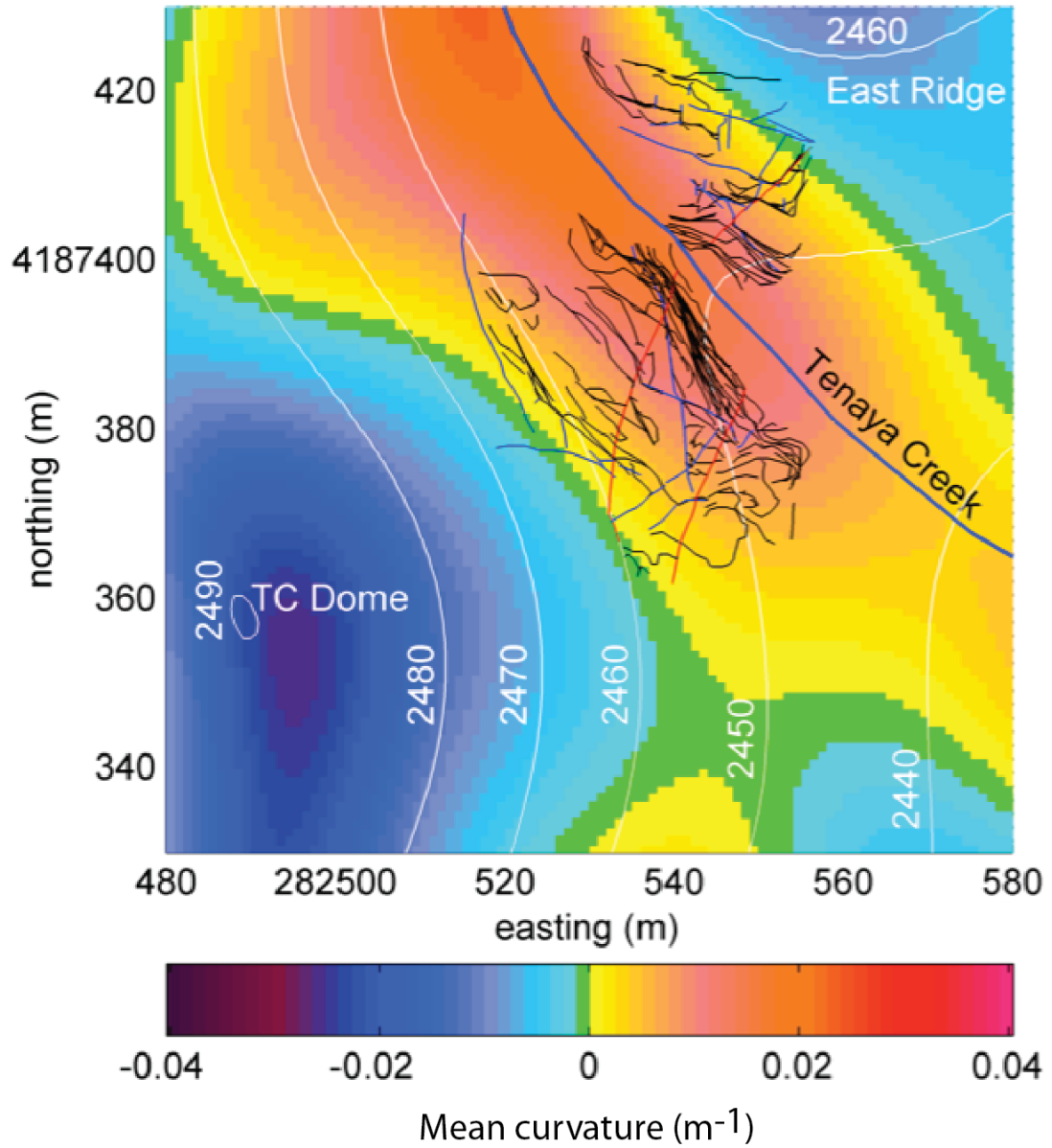


Figure 38. Mean curvature map of TC Dome study area from filtered aerial LIDAR data. Mean curvature values shown here vary between -2.6×10^{-2} and $2.1 \times 10^{-2} m^{-1}$. Fractures from Figure 20 are overlain for reference. Contours represent elevation in meters.

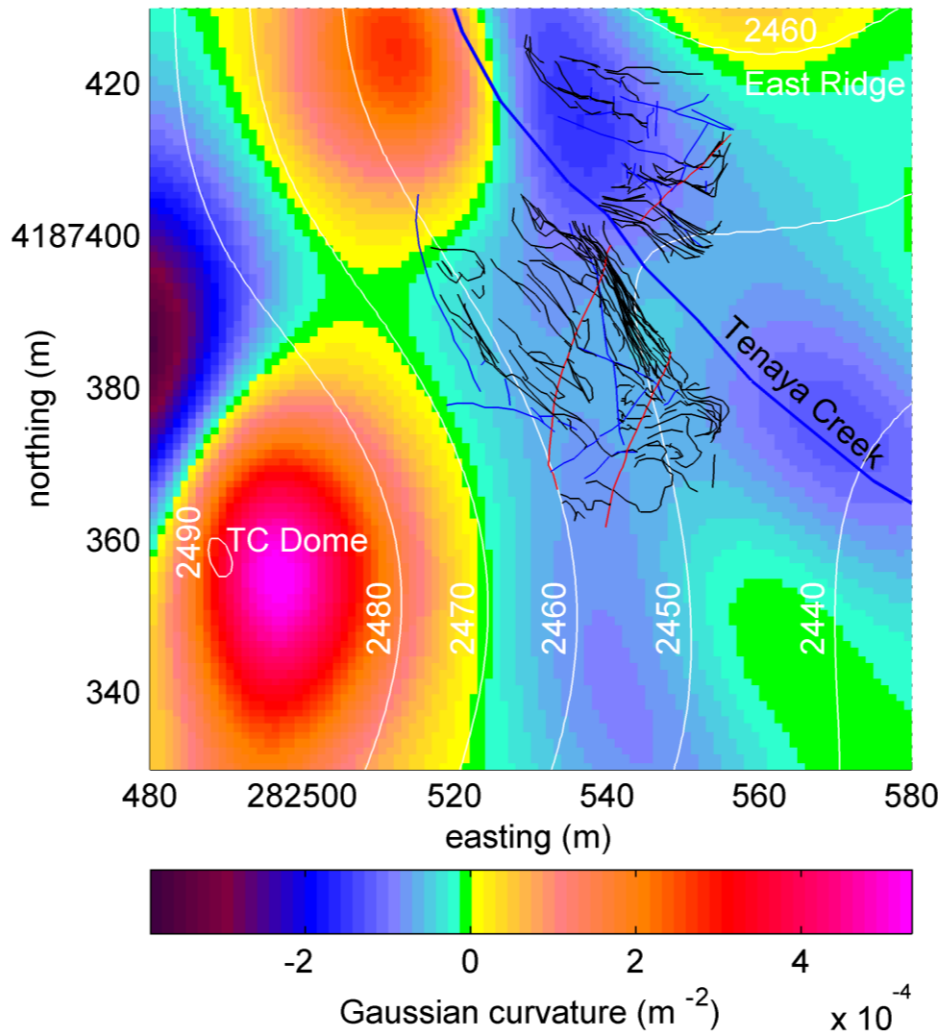


Figure 39. Gaussian curvature map of TC Dome study area from filtered aerial LIDAR data. Gaussian curvature values shown here vary between $-3.8 \times 10^{-4} \text{ m}^{-2}$ and $5.3 \times 10^{-4} \text{ m}^{-2}$. Positive Gaussian curvature values represent bowls and domes, and negative values represent saddles. Much of TC Dome and East Ridge would be classified as saddle-shaped, as would much of Tenaya Creek streambed. Contours represent elevation in meters.

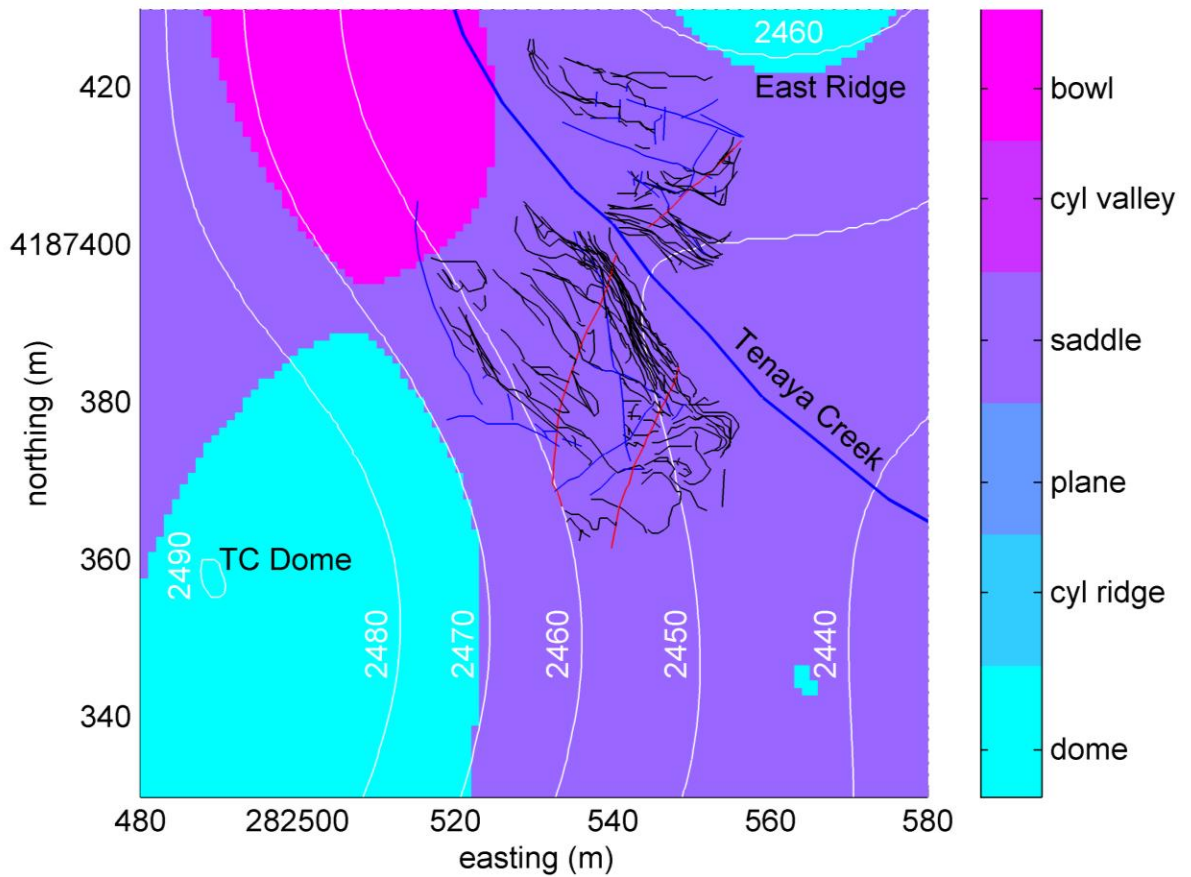


Figure 40. Topographic shapes based on combinations of principal curvatures k_1 and k_2 from filtered aerial LIDAR data. Cyan areas indicate domes, pink indicates bowls, and purple indicates saddles. Most of the topographic surface is saddle-shaped. The sheeting joints of Fig. 20 are in a saddle, not a dome. Contours represent elevation in meters.

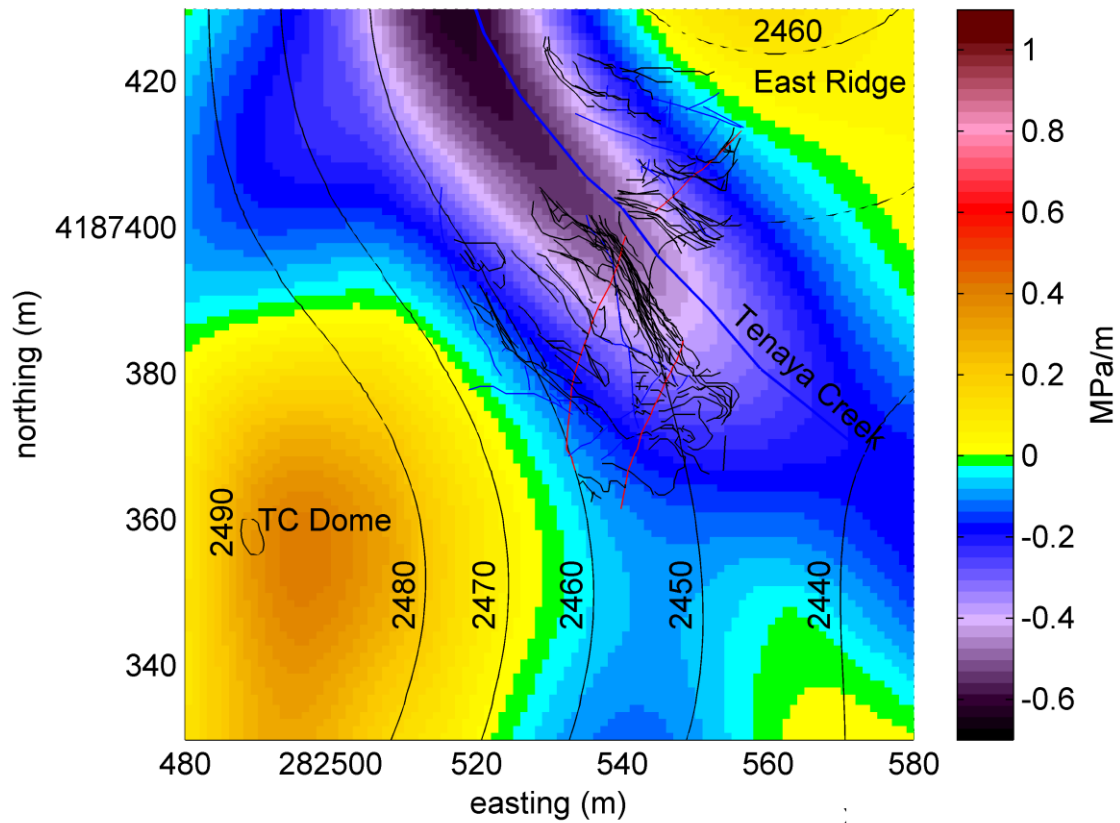


Figure 41. Lower bound for stress gradient ($\partial N / \partial z$) for TC Dome study area, based on stresses at Tuolumne Meadows and using curvatures from Figs. 36 and 37. $\partial N / \partial z$ varies between -0.6 and 0.4 MPa/m. Fractures from Fig. 20 are overlain for reference. Contours represent elevation in meters.

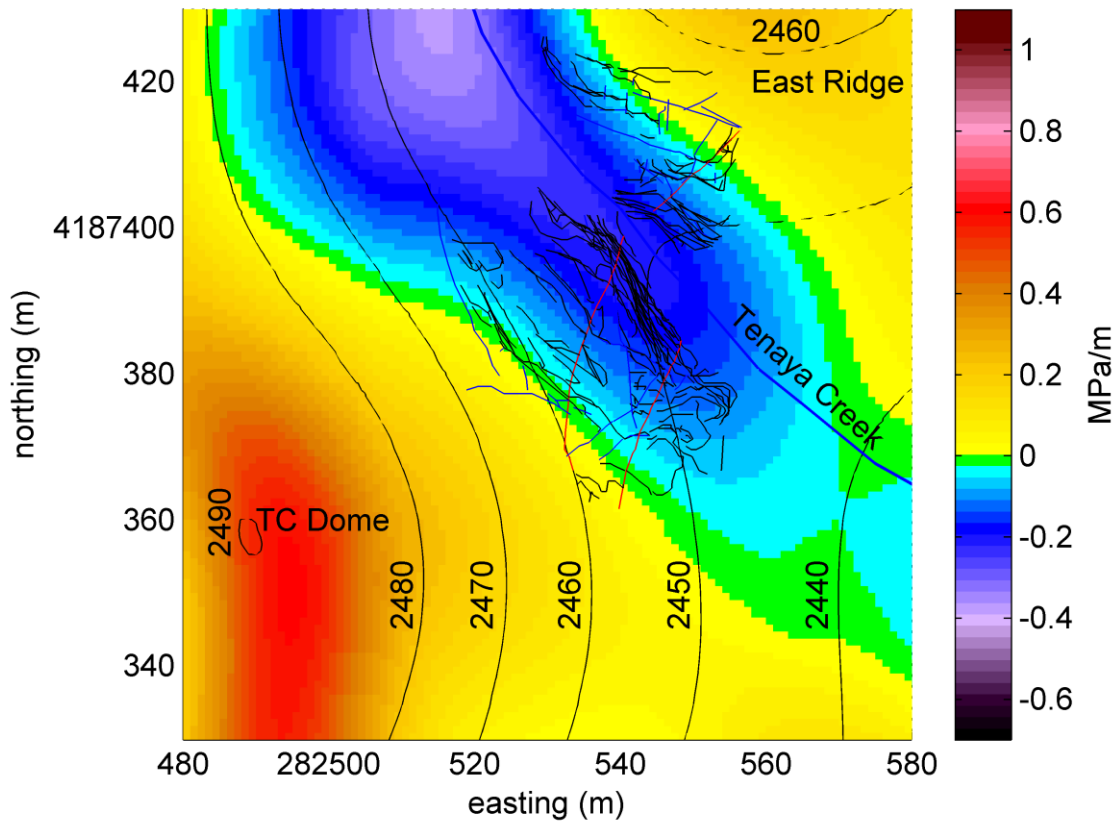


Figure 42. Upper bound for stress gradient ($\partial N/\partial z$) for TC Dome study area, based on stresses at Tuolumne Meadows and using curvatures from Figs. 36 and 37. $\partial N/\partial z$ varies between -0.4 and 0.6 MPa/m. Fractures from Fig. 20 are overlain for reference. Contours represent elevation in meters.

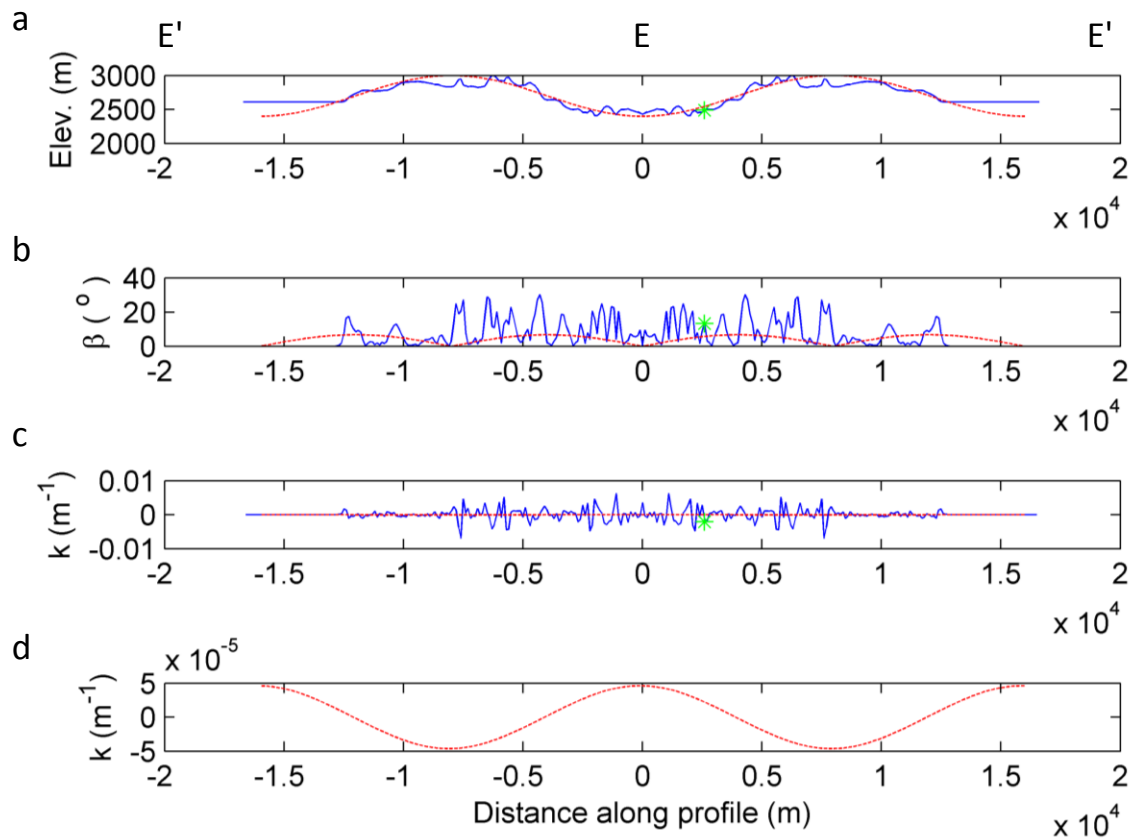


Figure 43. Geometry of regional profile E-E' of Fig. 5 (solid line) and a sinusoidal fit (dashed line). The point $x = 0$ corresponds to a point near the base of Cloud's Rest. The actual topography is mirrored about $x=0$. (a) Vertically exaggerated topographic profile. (b) Slope. (c) Curvature. (d) Curvature of sinusoidal fit.

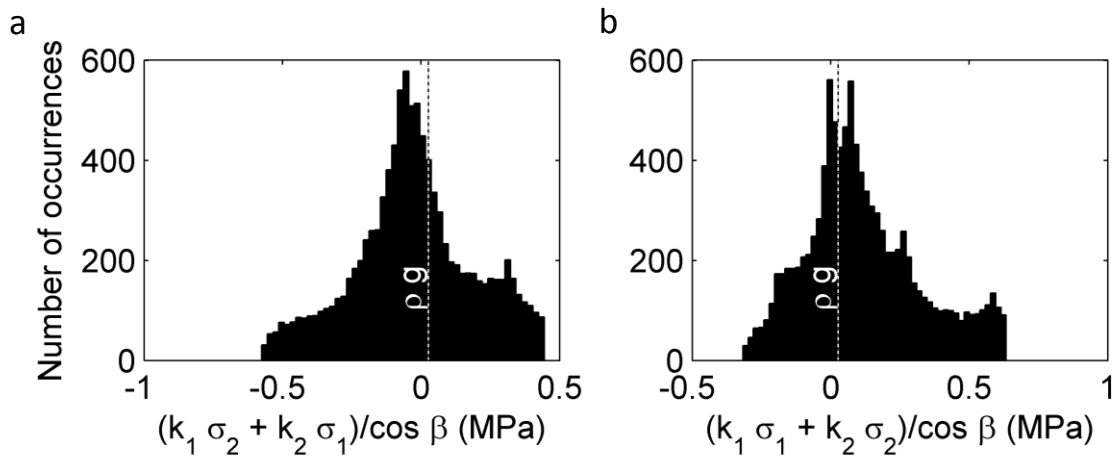


Figure 44. Histograms showing the distributions of calculated values of $\partial N/\partial z$ over a grid of 1x1 m cells for the TC Dome study area based on stresses equivalent to those at Tuolumne Meadows. The dashed line indicates a threshold. To its left, the stress gradient $\partial N/\partial z$ is negative and sheeting joints are predicted not to nucleate under current conditions. To the right, $\partial N/\partial z$ is positive and sheeting joints are predicted to be able to nucleate. (a) Histogram for the lower bound of $\partial N/\partial z$; approximately 36% of the surface of TC Dome study area has conditions sufficient to nucleate sheeting joints. (b) Histogram for the upper bound of $\partial N/\partial z$; approximately 64% of the surface has conditions sufficient for sheeting joint nucleation. The distributions together suggest that the study area as a whole is on the verge of being able to nucleate sheeting joints now.

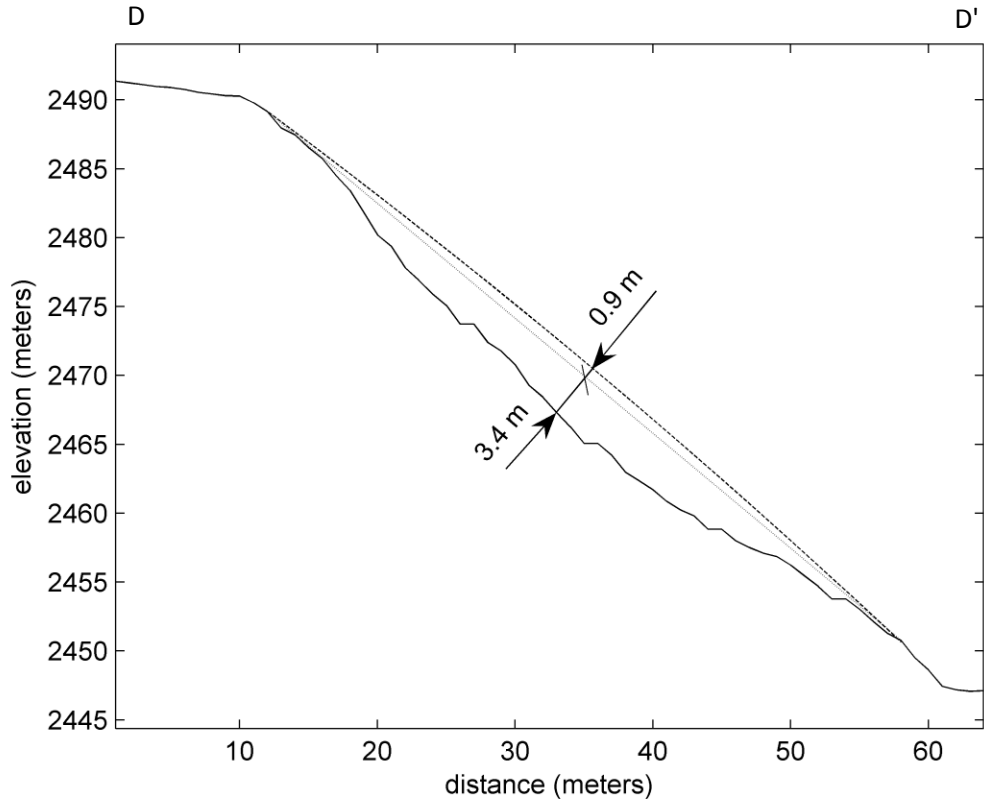


Figure 45. Cross-section profile D-D' (Fig. 24) trending N60°E, orthogonal to the trend of Tenaya Creek. The solid line represents the topographic profile from aerial LIDAR data. The dotted line represents a planar surface ($k = 0$). The dashed line represents the least convex surface required to account for sheeting joints in a profile ($k = -1.9 \times 10^{-3} \text{ m}^{-1}$). The maximum distance between the plane and the current topographic profile is 3.4 meters. An additional 0.9 meters is the maximum distance between the plane surface and the postulated convex paleo-surface. As little as 4.3 meters of glacial erosion could account for sheeting joints in this profile.

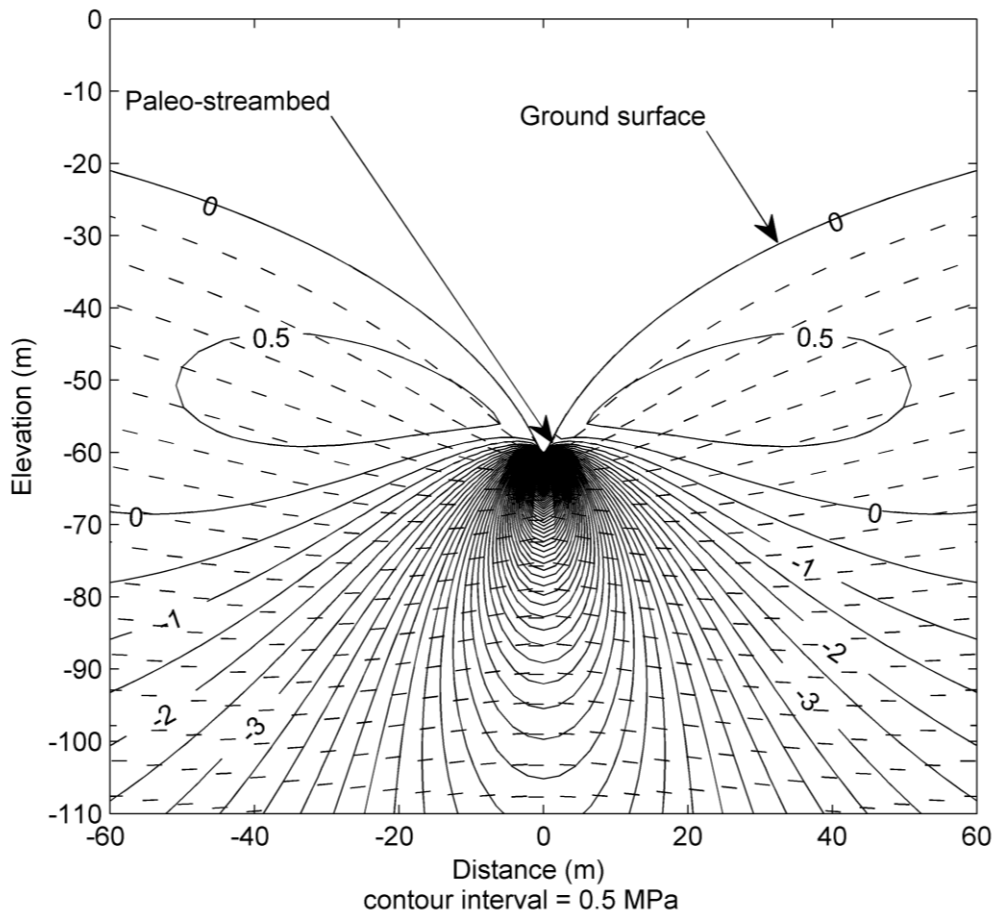


Figure 46. Conformal mapping solution showing most tensile stress values and trajectories of the most compressive stress below a cusp-shaped paleo-valley. Trajectories shown are a proxy for preferred sheeting joint orientation in cross-section. Sheeting joint trajectories shown here change from sub-parallel to topography near the sides of the diagram to nearly horizontal at the center beneath the cusp.

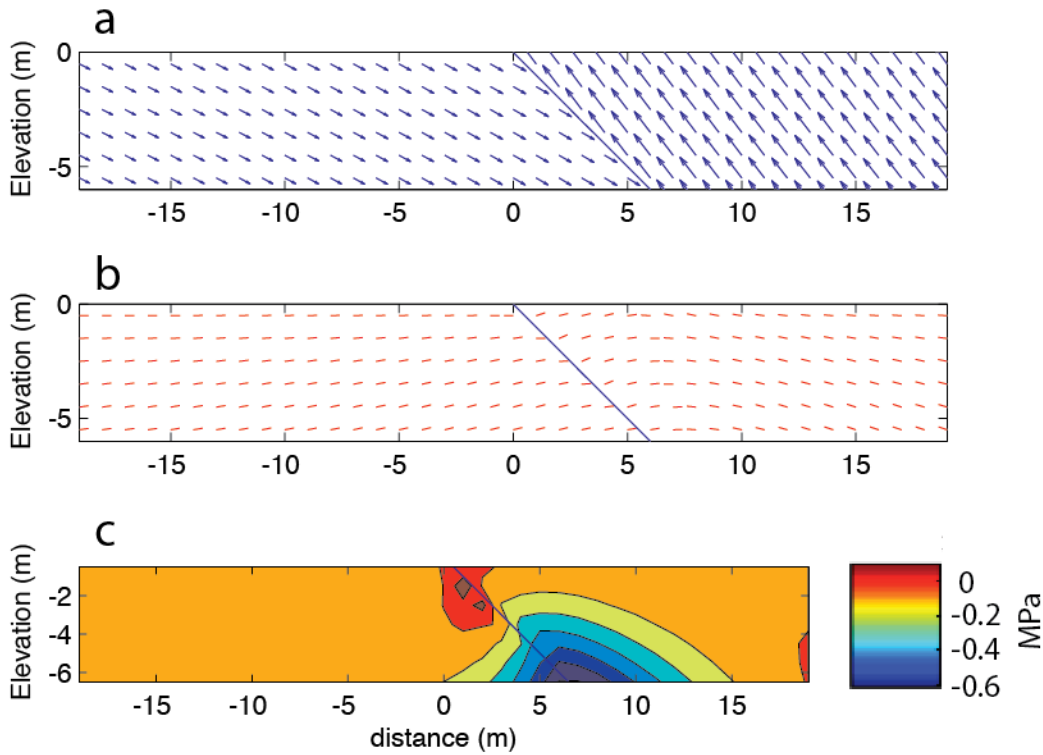


Figure 47. Linearly elastic boundary element model of deformation around a thrust fault that breaks the surface. The fault is 100 m long with a maximum slip of 0.25 m. Walls of the fault stay in contact. (a) Displacement field. (b) Trajectories of the most compressive stress, a proxy for preferred sheeting joint orientation. (c) The most tensile stress. Stress trajectories shown in (b) resemble the sheeting joint geometry observed in domains 1 and 2 of Fig. 18, with sheeting joints on the right curving steeply toward the fault and those on the left being nearly horizontal. The close spacing of sheeting joints in domain 1 could be accounted for by elevated tensile stress near the fault in (c). Fracture F2 may have slipped as a thrust fault before sheeting joints formed at TC Dome.

Appendix A: Orientation of Structural Features at TC Dome

Appendix A includes maps showing strike and dip of sheeting joint and fracture surfaces, and the locations for which detailed notes are available. Two maps are included in this appendix: A-1 shows the orientation data (strike and dip); A-2 shows locations for which detailed notes are available in the database.

All data used to make these maps as well as the fracture map from Fig. 20 are available in ASCII format (from myself or Dr. Martel) and include point names, location (northing, easting, and elevation in meters), and any additional information (e.g., strike and dip or other notes). Names are based upon the type of feature, the order in which it was surveyed, and the point along the feature. For example: SJ28B corresponds to the 28th sheeting joint surveyed, and the 2nd point (B) surveyed along that particular sheeting joint. Dikes and planar fractures are named DIKE and FRAC respectively; CPT indicates control points; and P indicates profile. For both the orientation data and the notes, the names and locations listed are the nearest surveyed point, usually within 0.5 meters of the actual strike and dip or location for which notes were taken.

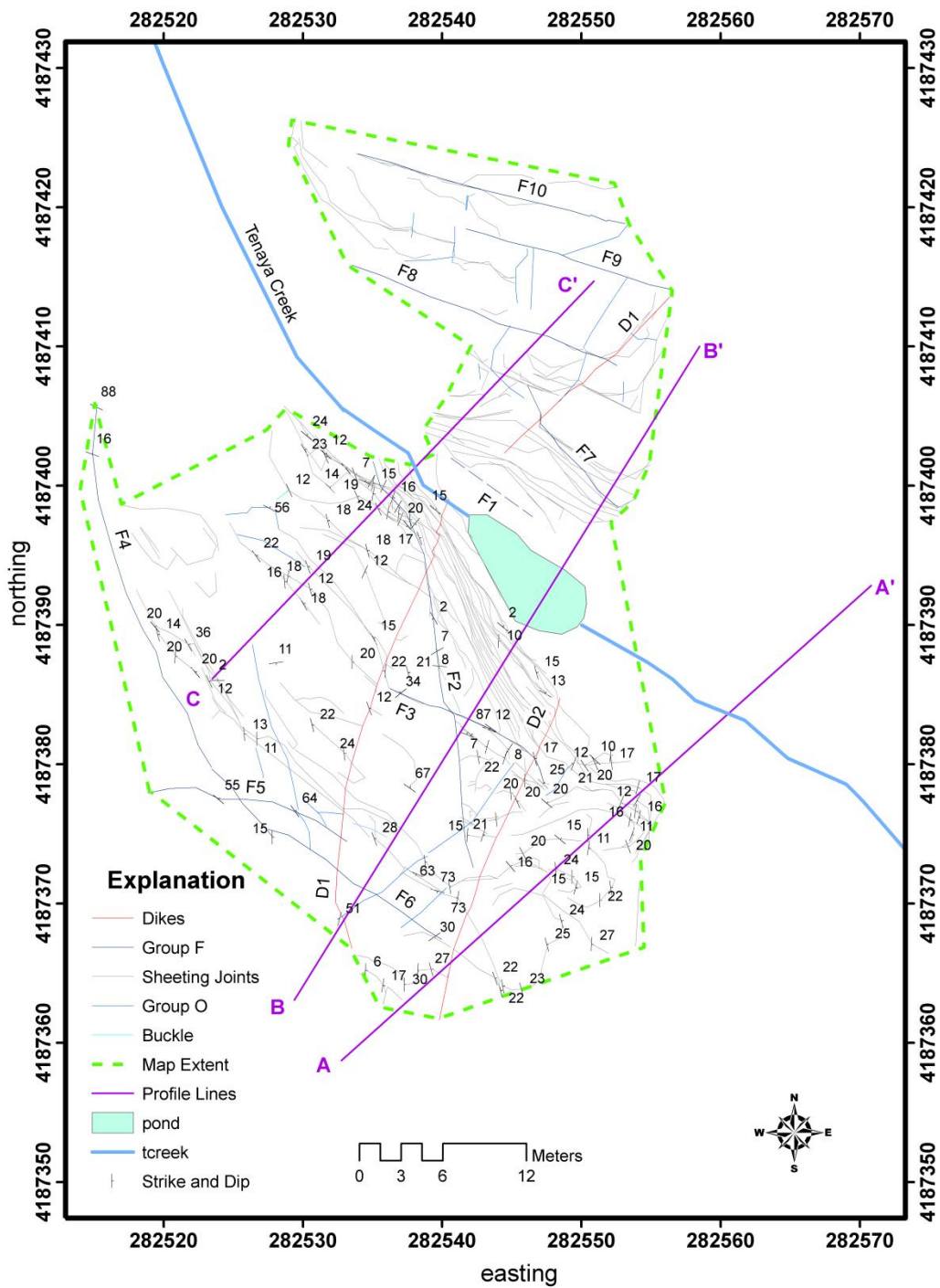


Figure A-1. Fracture map of TC Dome with orientation data for sheeting joints and fractures.

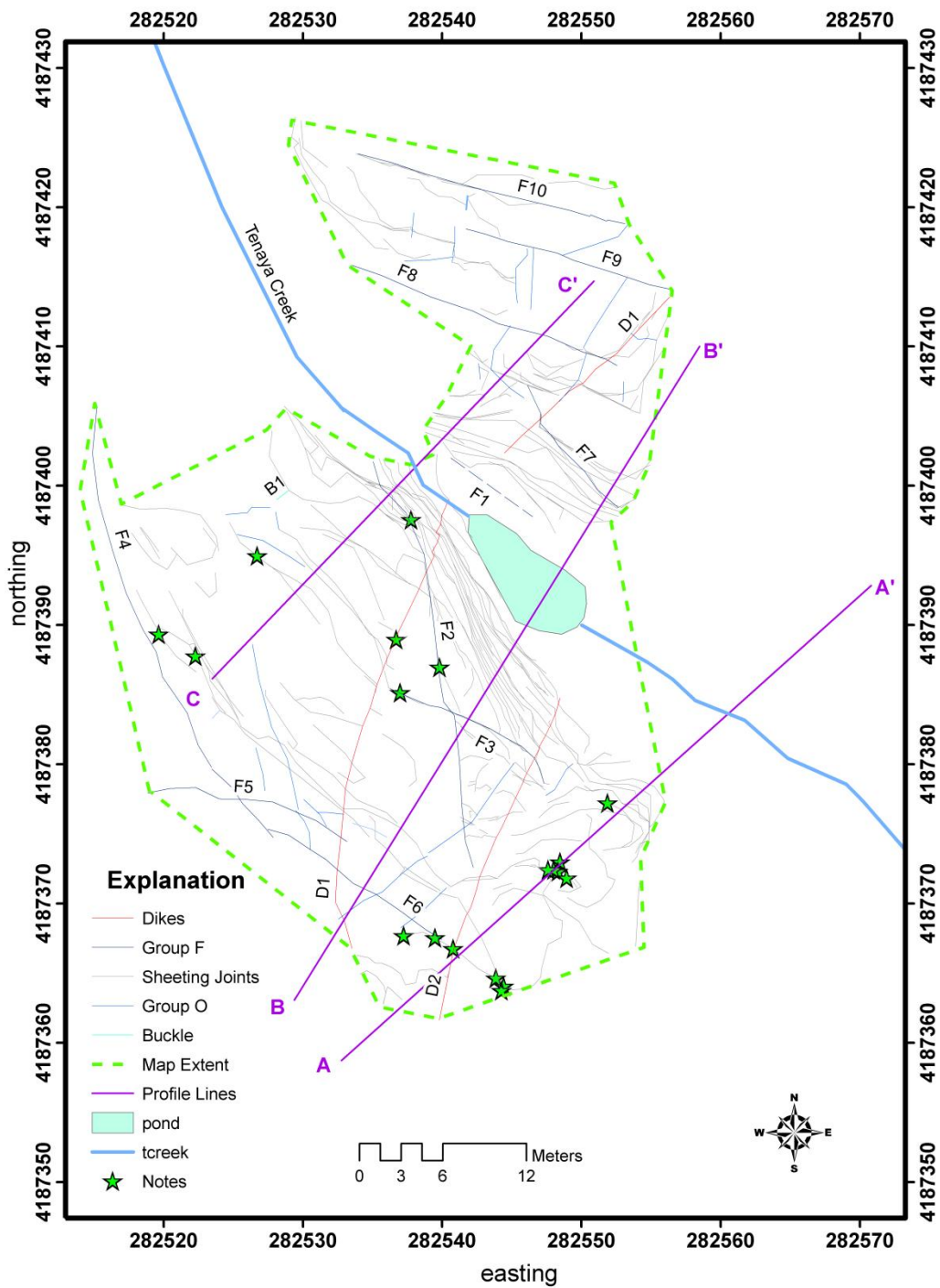


Figure A-2. Fracture map of TC Dome study area with stars depicting locations for which the following notes apply.

Notes

name	northing	easting	elevation	notes
SJ28C	282539.823	4187386.969	2452.403	note: sj28 dies at f2
SJ58A	282551.879	4187377.218	2450.301	photo: start of a sheeting joint
SJ81A	282537.769	4187397.562	2451.367	between 81a&b
SJ90A	282536.993	4187385.15	2455.119	note:sj90 dies into f2
SJ90F	282536.704	4187388.973	2455.049	photo: end of sj
SJ95J	282526.722	4187394.973	2458.406	note:f16 dies into sj95
SJ111A	282522.288	4187387.764	2462.732	photo: start of sj
SJ112C	282519.650	4187389.335	2463.656	photo: bifurcation
SJ121F	282548.471	4187372.979	2452.184	start of sj? My book says at pt 121g
SJ122A	282548.323	4187372.303	2452.289	photo: bifurcation
SJ122B	282548.017	4187372.414	2452.468	photo: bifurcation
SJ122C	282547.615	4187372.431	2452.644	photo: bifurcation/sj split
SJ123C	282548.941	4187371.820	2452.264	photo: start of sj123 @ dike
SJ132A	282544.418	4187364.058	2455.237	note: near f22d. F22 cuts sj132 surface. Sj132 is glacially polished
SJ135A	282544.269	4187363.744	2455.625	note: glacially polished surface. Striations: 000,11. frac23 cuts sj135.
SJ135B	282543.864	4187364.639	2455.659	note: glacially polished surface. Striations: 345, 4. frac23 cuts sj135.
SJ135E	282540.798	4187366.748	2457.202	photo: end of sj135,start of sj136, dike1
SJ136B	282539.489	4187367.542	2457.71	note: frac 7 dies into sj136
SJ136D	282537.233	4187367.685	2458.945	photo: fracture 7 dies at sj136

Appendix B: Sheet Curvature

Appendix B includes terrestrial (tripod-mounted) LIDAR data for TC Dome, and results of the curvature analyses of two individual sheeting joint surfaces. LIDAR data were collected by Ole Kaven (Stanford) and Nicholas VanDerElst (UC Santa Cruz) during the summer of 2007 with equipment loaned by Emily Brodsky (UC Santa Cruz). The spot spacing is approximately 5 cm. Figure B-1 shows a hillshade digital elevation model of TC Dome in map view, with the sheets of interest highlighted. Figure B-2 shows the maximum and minimum principal curvatures of individual sheeting joint surfaces.

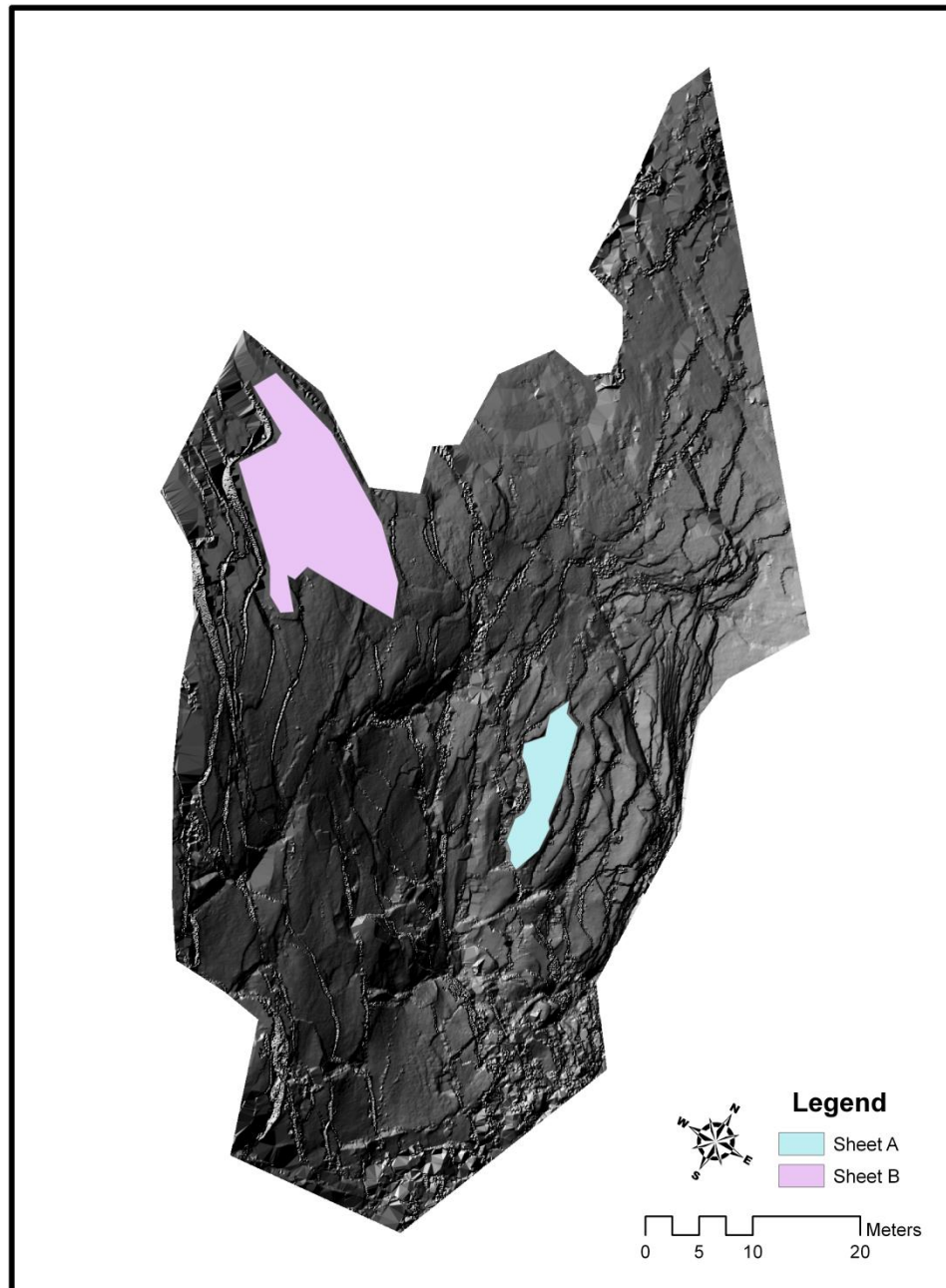


Figure B-1. Hillshade digital elevation model of TC dome from tripod-mounted LIDAR with 5 cm spot spacing. Curvature is calculated along two individual sheeting joint surfaces, A (light blue) and B (light purple); see Fig. B-2.

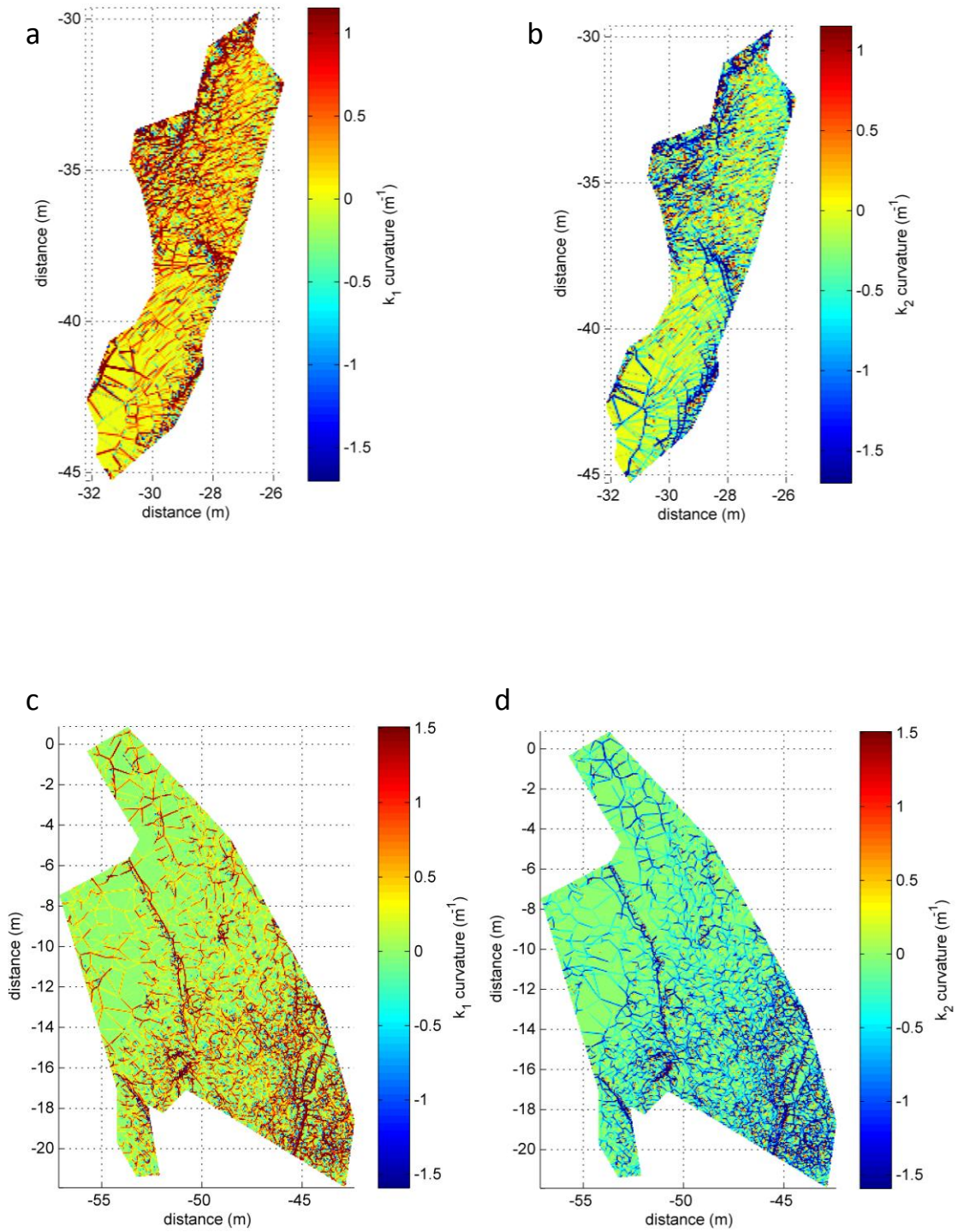


Figure A-2. Curvature of individual sheeting joint surfaces. (a-b) Curvature k_1 and k_2 of sheeting joint A. (c-d) Curvature k_1 and k_2 of sheeting joint B.

References Cited

- Bahat, D., Grossenbacher, K., and Karaski, K., 1999, Mechanism of exfoliation joint formation in granitic rocks, Yosemite National Park: *Journal of Structural Geology*, v. 21, p. 85-96.
- Bateman, P.C., and Wahrhaftig, C., 1966, Geology of the Sierra Nevada. In: Bailey, E.H. (Ed.), *Geology of Northern California (special issue): California Division of Mines and Geology Bulletin*, 190, p. 107-172.
- Bergbauer, S., 2002, The use of curvature for the analysis of folding and fracturing with application to the Emigrant Gap Anticline, Wyoming [PhD thesis]: Stanford University, 200 p.
- Bergbauer, S., and Pollard, D.D., 2003, How to calculate normal curvatures of sampled geological surfaces: *Journal of Structural Geology*, v. 25, p. 277–289.
- Bradley, W.C., 1963, Large-scale exfoliation in massive sandstones of the Colorado Plateau: *Geological Society of America Bulletin*, v. 74, p. 519–528.
- Cadman, J., 1969, The origin of exfoliation joints in granitic rocks [Ph.D. thesis]: Berkeley, University of California, 277 p.
- Carmichael, R.S., 1989, *Practical handbook of physical properties of rocks and minerals*: Boca Raton, Florida, CRC, 741 p.
- Cassel, E.J., Graham, S.A., and Chamberlain, C.P., 2009, Cenozoic tectonic and topographic evolution of the northern Sierra Nevada, California, through stable isotopic paleoaltimetry in volcanic glass: *Geology*, v. 37, p. 547-550.
- Chorley, R.J., Schumm, S.A., and Sugden, D.E., 1984, *Geomorphology*: London, Methuen, 605 p.
- Clark, D.H., 1995, Extent, timing, and climatic significance of latest Pleistocene and Holocene glaciation in the Sierra Nevada, California [Ph.D. thesis]: Seattle, Washington University, 191 p.

- Coleman, D.S., Gray, W., Glazner, A.F., 2004, Rethinking the emplacement and evolution of zoned plutons: Geochronologic evidence for incremental assembly for the Tuolumne Intrusive Suite, California: *Geology*, v. 32, p. 433-436.
- Crouch, S.L., and Starfield, A.M., 1983, *Boundary element methods in solid mechanics*: London, Allen and Unwin, 334 p.
- Dale, T.N., 1923, The commercial granites of New England: *U.S. Geological Survey Bulletin*, 738, 488 p.
- Ericson, K., and Olvmo, M., 2004, A-tents in the central Sierra Nevada, California: a geomorphological indicator of tectonic stress: *Physical Geography*, v. 25, p. 291-312.
- Gilbert, G.K., 1904, Dome and dome structures of the High Sierra: *Geological Society of America Bulletin*, v. 15, p. 29-36.
- Gillespie, A.R., 1982, Quaternary glaciation and tectonism in the southeastern Sierra Nevada, Inyo County, California [Ph. D. thesis]: Pasadena, California Institute of Technology, 695 p.
- Glazner, A.F., Bartley, J.M., Coleman, D.S., Gray, W., and Taylor, R.Z., 2004, Are plutons assembled over millions of years by amalgamation from small magma chambers?: *GSA Today*, v. 14, p. 4-11.
- Goudie, A.S. (Ed.), 2004, *Encyclopedia of geomorphology*: London, Rutledge, 1156 p.
- Henry, C.D., 2009, Uplift of the Sierra Nevada, California: *Geology*, v. 37, p. 575-576.
- Holman, W.R., 1976, The origin of sheeting joints: A hypothesis [Ph.D. thesis]: Los Angeles, University of California, 75 p.
- Holzhausen, G.R., 1977, Sheet structure in rock and some related problems in rock mechanics [Ph. D. thesis]: Stanford, California, Stanford University, 515 p.

Holzhausen, G.R., 1989, Origin of sheet structure, 1, Morphology and boundary conditions: *Engineering Geology*, v. 27, p. 225-278.

Huber, N.K., 1987, The geologic story of Yosemite National Park: U.S. Geological Survey Bulletin, 1595, 64 p.

Jahns, R.H., 1943, Sheet structure in granites, its origin and use as a measure of glacial erosion in New England: *Journal of Geology*, v. 51, p. 71-98.

Leithold, L., 1967, *The calculus with analytical geometry*: New York, Harper and Row, 976 p.

Martel, S.J., 2000, Modeling elastic stresses in long ridges with the displacement discontinuity method: *Pure and Applied Geophysics*, v. 157, p. 1039-1057.

Martel, S.J., and Muller, J.R., 2000, A two-dimensional boundary element method for calculating elastic gravitational stresses in slopes: *Pure and Applied Geophysics*, v. 157, p. 989-1007.

Martel, S.J., 2005, Effect of surface curvature on the normal stress normal to the topographic surface, with application to sheeting joints: American Geophysical Union 2005 fall meeting, San Francisco, CA, United States, Dec. 5-9, 2005

Martel, S.J., 2006, Effect of topographic curvature on near-surface stresses and application to sheeting joints: *Geophysical Research Letters*, 33, L01308.

Matthes, F.E., 1930, Geologic history of the Yosemite Valley: U.S. Geological Survey Professional Paper, 160, 137 p.

Miller, D.J., and Dunne, T., 1996, Topographic perturbations of regional stresses and consequent bedrock fracturing: *Journal of Geophysical Research*, v. 101, p. 523-525, 536.

Mynatt, I., Bergbauer S., and Pollard D.D., 2007, Using differential geometry to describe 3-D folds: *Journal of Structural Geology*, v. 29, p. 1256-1266.

Pearce, M.A., Jones R.R., Smith S.A.F., McCaffrey K.J.W., and Clegg P., 2006, Numerical analysis of fold curvature using data acquired by high-precision GPS: *Journal of Structural Geology*, v. 28, p. 1640-1646.

Perron, J.T., J.W. Kirchner, and W.E. Dietrich, 2008, Spectral signatures of characteristic spatial scales and nonfractal structure in landscapes: *Journal of Geophysical Research*, v. 113, F04003, doi:10.1029/2007JF000866.

Phillips, F.M., Zreda, M.G., Benson, L.V., Plummer, M.A., Elmore, D., and Sharma, P., 1996, Chronology for fluctuations in late Pleistocene Sierra Nevada glaciers and lakes: *Science*, v. 274, p. 749-761.

Pollard, D.D., and Segall, P., 1987, Theoretical displacements and stresses near fractures in rock; with application to faults, joints, veins, dikes, and solution surfaces. In: Atkinson, B.K. (ed.), *Fracture mechanics of rock*: London, Academic Press, p. 277-349.

Pollard, D.D., and Aydin, A.A., 1988, Progress in understanding jointing over the past century: *Geological Society of America Bulletin*, v. 100, p. 1181-1204.

Pollard, D.D., and Fletcher, R.C., 2005, *Fundamental of structural geology*: Cambridge, U.K., Cambridge University Press, 500 p.

Roberts, A., 2001, Curvature attributes and their application to 3D interpreted horizons: *2001 First Break*, v. 19, p. 85-100.

Savage, W.Z., Powers, P.S., and Swolfs, H.S., 1984, In situ geomechanics of crystalline and sedimentary rocks; Part V, RVT, a Fortran program for an exact elastic solution for tectonics and gravity stresses in isolated symmetric ridges and valleys: U. S. Geological Survey open-file report OF 84-0827, 12 p.

Savage, W.Z., and Swolfs, H.S., 1986, Tectonic and gravitational stress in long symmetric ridges and valleys: *Journal of Geophysical Research*, v. 91, p. 3677-3685.

Segall, P., and Pollard, D.D., 1983, Joint formation in granitic rock of the Sierra Nevada: Geological Society of America Bulletin, v. 94, p. 563– 575.

Small, E.E., and Anderson, R.S., 1995, Geomorphically driven late Cenozoic rock uplift in the Sierra Nevada, California: Science, v. 270, p. 277-280.

Smith, J.O., 2007, Mathematics of the discrete Fourier transform (DFT) with audio applications, second edition: <http://ccrma.stanford.edu/~jos/mdft/>, online book, accessed 10/19/2008.

Smith, S.W., 1997, The scientist and engineer's guide to digital signal processing: <http://www.dspguide.com/>, online book, accessed 4/20/2010.

Strang, G., 1988, Introduction to linear algebra: Wellesley, MA, Wellesley-Cambridge Press, 503 p.

Struik, D.J., 1961, Lectures on classical differential geometry: New York, Dover, 232 p.

Trexler, K.A., 1961, The Tioga Road; a History 1883-1961, Yosemite Natural History Association: http://www.yosemite.ca.us/library/tioga_road/, online book, accessed 4/28/2010.

Turcotte, D.L., and Schubert, G., 2002, Geodynamics: New York, Cambridge University Press, 456 p.

Twidale, C.R., 1971, Structural landforms; landforms associated with granitic rocks, faults, and folded strata: An introduction to systematic geomorphology, v. 5: Cambridge, MA, MIT Press, 247 p.

Twidale, C.R., 1982, Granite landforms: New York, Elsevier, 372 p.

Unruh, J.R., 1991, The uplift of the Sierra Nevada and implications for late Cenozoic epeirogeny in the western Cordillera: Geological Society of America Bulletin, v. 103, p. 1395-1404.

USGS, n.d., U.S. Geological Survey Photographic Library, ID. Huber, N.K. 50ct, accessed July 6, 2010, <http://libraryphoto.cr.usgs.gov/cgi-bin/show_picture.cgi?ID=ID.%20Huber,%20N.K.%20%2050ct>.

USGS, n.d., U.S. Geological Survey Photographic Library, ID. Gilbert, G.K. 3162, accessed July 6, 2010, <[http://libraryphoto.cr.usgs.gov/cgi-bin/show_picture.cgi?ID=ID.Gilbert, G.K. 3162](http://libraryphoto.cr.usgs.gov/cgi-bin/show_picture.cgi?ID=ID.Gilbert,%20G.K.%203162)>.

Wakabayashi, J., and Sawyer, T.L., 2001, Stream incision, tectonics, uplift, and evolution of topography of the Sierra Nevada, California: *Journal of Geology*, v. 109, p. 539-562.

Wernicke, B., Clayton, R., Ducea, M., Jones, C.H., Park, S., Ruppert, S., Saleeby, J., Snow, J.K., Squires, L., Fliedner, M., Jiracek, G., Keller, R., Klemperer, S., Luetgert, J., Malin, P., Miller, K., Monney, W., Oliver, H., and Phinney, R., 1996, Origin of high mountains in the continents: The southern Sierra Nevada: *Science*, v. 271, p. 190-193.

Wikipedia, January 15, 2007, Yosemite West map, accessed July 6, 2010, <<http://en.wikipedia.org/wiki/index.html?curid=8790592>>.